Molecular Effects in Tritium Beta-Decay Neutrino-Mass Measurements

Laura I. Bodine

A dissertation
submitted in partial fulfillment of the
requirements for the degree of

Doctor of Philosophy

University of Washington

2015

Reading Committee:

R. G. Hamish Robertson, Chair

Jason Detwiler

R. Jeffrey Wilkes

Program Authorized to Offer Degree:
Physics

University of Washington

Abstract

Molecular Effects in Tritium Beta-Decay
Neutrino-Mass Measurements

Laura I. Bodine

Chair of the Supervisory Committee:
Professor R. G. Hamish Robertson
Department of Physics

An understanding of the molecular final state distribution is crucial to extracting a neutrino mass from molecular tritium-based experiments including the upcoming Karlsruhe Tritium Neutrino Mass Experiment. This dissertation studies molecular systematics for the upcoming neutrino mass measurements and discusses the measurement of molecular dissociation as a test of final state distribution calculations.

TABLE OF CONTENTS

LIST OF FIGURES

LIST OF TABLES

GLOSSARY

ADC: Analog to digital converter, electronics that convert analog signals into digital values by converting the peak height

CENPA: Center for Experimental Nuclear Physics and Astrophysics at the University of Washington, a Department of Energy Center of Excellence

CMB: Cosmic microwave background

DAQ: Data acquistion

FSD: Final state distribution

GUT: Grand Unified Theory predicting the unification of the electroweak and strong forces at high energy scales

KATRIN: Karlsruhe Tritium Neutrino Experiment, the next-generation tritium-based neutrino mass experiment currently under construction at KIT

KIT: Karlsruhe Institute of Technology

LANL: Los Alamos National Laboratory

LLNL: Lawrence Livermore National Laboratory

MAC-E: Magnetic adiabatic collimation with and electrostatic filter

MC: Monte Carlo, simulation method using random numbers to sample the space

ORCA: Object-oriented Realtime Control and Acquisition; software which controls the DAQ

PIPS: Passivated implanted planar silicon detectors, silicon detectors manufactured by Canberra Semiconductor

PMNS: Pontecorvo-Maki-Nakagawa-Sakata, contributors to neutrino mixing matrix

RGA: Residual gas analyzer

ROOT: An object-oriented analysis framework

SNO: Sudbury Neutrino Observatory, a solar neutrino experiment

TORI: Table of Radioactive Isotopes database maintained by Lawrence Berkeley Laboratory

UHV: Ultra-high vacuum

WGTS: Windowless, gaseous tritium source

WMAP: Wilkinson Microwave Anisotropy Probe

ΛCDM: Cosmological model containing dark energy and cold dark matter

ACKNOWLEDGMENTS

I express sincere appreciation to my family and friends for their constant support. First and foremost is my mother, Wilma Dulin, who has always been a strong role model–intelligent, hard-working and compassionate. My father, Scott Bodine, augmented my many trips to Germany, adding joy and levity. And as always thanks to my siblings for their constant reminders of the world beyond academic pursuits.

A huge thank you to my friends who have always been understanding of my crazy travel schedule and stressful life. Thanks to Dr. William Terrano for his never-ending support during graduate school and for always believing in me–you will always be family. To Eric and Zoe Wallace for many late nights spent recharging. To Brett Wolfe for his unwavering support and colorful stories. And last but not least Dr. Michelle Zimmerman, an amazing woman who is always up for new adventures.

Thanks to the CENPA students, postdocs, faculty and, most importantly, staff for their support. CENPA has the best technical staff in the world and I wouldn't have been able to do this project without their pateience and support. In particular John Amsbaugh, Tom Burritt, Jim Elms, Greg Harper, David Hyde, Gary Holman, David Peterson, Hank Simons, Eric Smith, Tim Van Wechel, and Doug Will. Thanks to the front office staff who make the lab run smoothly: Bob Shupe and Victoria Clarkson. A special thanks to Jason Detwiler & Joy Sebe, Diana & Brian Parno, Noah Oblath, Christian Boutan, Charlie Hagedorn, Rachel Ryan, Julieta Gruszko and Catherine Provost for bringing humanity to the difficult process of dissertating and dealing with real life.

A very special thanks to the Space Needle for being my writing haven. There's

nothing like looking out on an unbeatable view to stoke creativity.

My work has been supported by the Department of Energy Office of Science Nuclear Physics Program under grant #DE-FG02-97ER41020.

DEDICATION

to my parents

Chapter 1

NEUTRINO MASS

In this chapter we introduce the basic concepts of neutrino mass and issues related to adding neutrinos to the Standard Model. We discuss three approaches to determining the neutrino mass: searching for neutrinoless double-beta decay, indirect cosmological limits and direct measurement via tritium beta decay.

1.1 Introduction to Massive Neutrinos

The neutrino (ν) has been the subject of intense study since Wolfgang Pauli first postulated its existence in 1930 [12]. First understood as a massless, spin-1/2 fundamental particle required to conserve energy and momentum in beta decay, the neutrino has proven a useful tool for studying fundamental physics as well as an interesting research subject in its own right. From supernovae to the unification of the fundamental forces, neutrinos play a critical role in our description of the universe. In particular, neutrino mass is the first confirmed disagreement with the standard model of particle physics. A direct measurement of the mass will improve our understanding of particle physics and, hopefully, provide insight into the origin of mass.

The standard model contains three neutrinos, one associated with each of the three charged leptons: electron (e), muon (μ) and tau (τ). Often called flavors, these designate *interaction* eigenstates that couples to the W boson and associated charged lepton. In general the *mass* eigenstates need not be equivalent to the interaction eigenstates and particle oscillations result if the two bases are not equivalent. The observation of neutrino flavor disappearance in Super-Kamiokande experiment was the first evidence for massive neutrinos [13].

Subsequent solar neutrino (SNO[14]), reactor neutrino (KamLAND[15], DayaBay[16], Double Chooz[17], RENO[18]) and accelerator neutrino (K2K[19], MINOS[20], T2K[21], OPERA[22]) experiments have generated a nearly complete picture of three-state oscillations. The current picture comprises three mass states (ν_1, ν_2, ν_3) and three flavor states (ν_e, ν_μ, ν_τ), connected by the unitary Pontecorvo-Maki-Nakagawa-Sakata (PMNS) mixing matrix elements U_{fi} [23]. The observation of oscillations with two different frequencies implies two distinct mass splittings, that is at least two nonzero neutrino masses. While the absolute mass scale is constrained by a variety of experimental probes with different model dependence and sensitivity, the scale remains unknown. In the current paradigm the neutrino mass is bounded above by tritium beta decay at the 2-eV level and below by the oscillation parameters at the 0.05-eV level [23].

The connection between the mass and flavor states facilitates a description of the *effective* mass of each flavor state in terms of the three masses. The smallness of the mass splittings, the connection between the mass and flavor eigenstates, allows processes like beta decay to probe the absolute neutrino mass scale. The mass splittings are significantly smaller than the current limit on the neutrino mass scale and the mass states can be treated as degenerate. In this quasi-degenerate limit the expression for the electron flavor neutrino takes on a simple form:

$$m_{\nu_e}^2 = \sum_i |U_{ei}|^2 m_i^2 \tag{1.1}$$

The current generation of experiments will probe the quasi-degenerate mass regime. Future experiments are necessary to probe the regime in which the masses are hierarchical and to probe for the ordering for the mass states.

1.2 Neutrino mass in the standard model

Consistent with a minimalist philosophy and to avoid a hierarchy problem, the standard model was constructed with massless neutrinos. In order to incorporate neutrino

mass in the model we must identify the correct terms to add to the Lagrangian. Determining the neutrino-mass Lagrangian requires extensive study, not only of the neutrino mass scale but also of the very nature of the neutrino. While charged massive particles have only Dirac mass terms, the neutrino is neutral under all but the weak interaction and thus can be its own antiparticle with a Majorana mass term.

A Majorana mass term opens the possibility that the tiny neutrino mass is related to higher energy phenomena, naturally explaining the apparent fine tuning of small neutrino masses [24]. The see-saw mechanism ties the right-handed unobservable neutrinos and the smallness of the neutrino mass to the scale at which all the fundamental forces become one in the Grand Unified Theory (GUT) [25, 26]. The ratio of a typical particle mass to the GUT scale gives rise to the tiny observed neutrino mass. The attractiveness of the see-saw solution has inspired myriad formal models incorporating this basic concept but with different particle content (e.g. Higgs multiplets) and interactions. The existence of a Majorana mass term would open a window into beyond-the-standard-model physics, providing a glimpse at the processes that underlie our current description of the world.

1.3 Neutrinoless double-beta decay

Observing neutrinoless double-beta decay ($0\nu\beta\beta$) is the most direct method of determining that neutrinos are Majorana in nature. The Feynman diagrams for double-beta decay and neutrinoless double-beta decay are shown in Fig. 1.1. The neutrinoless version of the decay requires a lepton number violation (by two units). While the decay may be mediated by another light, neutral particle (such as the lightest supersymmetric particle) the existence of neutrinoless double-beta decay *necessarily* implies that the neutrino has a Majorana mass term [27]. Assuming the process is mediated by neutrinos the half-life $T^{0\nu}_{1/2}$ of the $0\nu\beta\beta$ decay is related to the nuclear matrix element $M^{0\nu}$, phase space factor $G^{0\nu}$, and the coherent sum of the neutrino masses $m_{\nu i}$ weighted by the matrix elements U_{ei}:

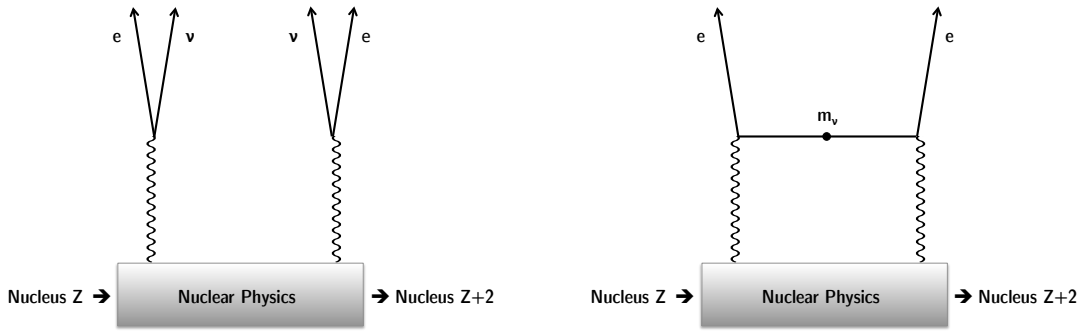

Figure 1.1: Two neutrino and neutrinoless double-beta decay Feynman diagrams.

$$T^{0\nu}_{1/2} = G^{0\nu}|M^{0\nu}|^2 \langle m^2_{\beta\beta}\rangle\,, \tag{1.2}$$

$$\langle m^2_{\beta\beta}\rangle = |\sum_i U^2_{ei} m_{\nu i}|^2. \tag{1.3}$$

The matrix elements contain CP-violating "Majorana phases" that are not observable in oscillation experiments. The combination of the Majorana phases and the possibility of having both Dirac and Majorana terms changes the interpretation of a half-life in terms of an absolute mass scale as it opens up the possibility of the see-saw mechanism [25].

If neutrinoless double-beta decay occurs it is extremely rare and experiments with ultra low backgrounds are necessary to search for it. Many experiments, including Majorana, EXO, KamLAND-Zen, GERDA, and SuperNEMO, are making progress toward ton-scale neutrinoles double-beta decay experiments in a variety of isotopes. The most sensitive limits on half-life come from the EXO, KamLAND-Zen and GERDA collaborations. For the decay of xenon-136, the EXO collaboration set a half-life limit of 1.1×10^{25} yr [28]; KamLAND-Zen set a limit of 1.9×10^{25} yr [29] for a combined limit of 3.4×10^{25} yr [29]. For the decay of germanium-76 the GERDA

collaboration set a half-life limit of 2.1×10^{25} yr [30]. Uncertainties in the calculations of matrix elements and the possibility of other mediators complicate the interpretation of lifetimes in terms of fundamental neutrino parameters [31]. Results for several different isotopes will be necessary for a definitive measurement and to cross-check systematics. The search for neutrinoless double-beta decay is an active field of neutrino research that may provide interesting insight into the nature of the neutrino.

1.4 Astrophysics, cosmology and neutrino mass

Neutrino mass plays a wide variety of roles in astrophysics and cosmology. Neutrinos are able to stream from some of the densest regions in the universe.

Neutrinos play important roles in astrophysics by allowing us to probe extreme environments in remote parts of the universe. The extreme environments in core collapse supernovae provide a possible probe of the ordering of the mass states. The neutrino mass itself affects the energy density during early times. In such models the flavor profile of neutrinos is expected to vary with time and this"flavor swapping" has been proposed as a method of probing the neutrino mass hierarchy [32].

Unfortunately nearby supernovae are extremely rare and to date the only observed supernova neutrinos came from the explosion of supernova 1987A (SN1987A) in the nearby Large Magellanic Cloud. Prior to the arrival of the light from SN1987A bursts of neutrinos were seen in three large-scale neutrino detectors: two water Cherenkov detectors and one scintillator detector. The water Cherenkov Kamiokande-II detector observed 12 neutrinos [33] while the IMB detector observed eight neutrinos [34]. The scintillator detector Baksan observed five neutrinos [35]. A slightly earlier burst of neutrinos in the LSD scintillator experiment was initially attributed to SN1987A but has subsequently been discounted [36, 37] due to a timing discrepancy. In conjunction with SN1987A a total 25 MeV-range neutrinos were detected during a 13-second window. The timing and energy of these signals is consistent with models of supernova explosions. The observation of these neutrinos preceeded the photon observation by

several hours and a comparison of the difference in photon and neutrion timing led Bahcall and Glashow to set an 11-eV limit on the mass of the electron neutrino [38]. The observation of SN1987A played an important role in motivating future neutrino astrophysical studies.

Additionally, the field of cosmology is deeply impacted by neutrinos and would benefit from measurements of the neutrino mass parameters[39]. The number of neutrino species and the neutrino mass play an important role in cosmology as they closely mimic the behavior of both dark matter and the dark energy equation of state parameter. Cosmological data have been used to set stringent limits on the neutrino mass but many of them have been shown to be unreliable due to the use of strict priors imposed by tensions between the data sets [40]. The standard techniques use precise studies of the cosmic microwave background (CMB) as the basis for determining cosmological parameters, adding galaxy surveys and other observations to tighten limits on neutrino mass.

Large scale structures such as galaxy clusters contain information about the neutrino mass from primordial density fluctuations. The imprint of neutrino mass can be measured by looking at variations in the CMB. Being electrically neutral neutrinos do not couple to the photon and interact much more weakly than electrons and photons. The interaction cross sections for electrons and photons were large enough that the particles in high-density regions became trapped, unable to escape. But the neutrino cross section is very weak and neutrinos were able to leave these very dense regions at a high rate. The neutrino streaming rate depends on the mass of the neutrinos, thus the rate at which energy fluctuations are dissipated by neutrinos depends on the mass spectrum. The size of structure in the universe provides a snapshot of the density fluctuations, providing indirect limits on the neutrino mass.

Several studies have published limits on neutrino mass from combined measurements. Constraining the neutrino mass with astrophysical data requires the choise of a specific cosmological model of the universe, generally taken to be ΛCDM. Issues

arise from combining experiments with different systematics as well as from degeneracies in the fits. A direct laboratory measurement of the neutrino mass would allow cosmologists to constrain more precisely other important parameters, in particular the dark energy equation of state parameter.

The Planck satellite provides the most precise measurements of the CMB and sets the most stringent limits on the neutrino mass. The Planck CMB anistropy limit is $\sum m_\nu < 0.72$ eV at the 95% confidence level[41]. The collaboration reports tighter constraints when external data are considered in addition to the CMB. The limit of $\sum m_\nu < 0.23$ eV (95% confidence level) includes lensing, baryon acoustic oscillations, supernovae surveys and direct measurements of the Hubble constant in addition to the polarization information from Planck. More stringent limits can be reported by adding other data but at the cost of introducing tension in the fit.

While Planck provides unprecedented precision on the CMB, their highlighted neutrino-mass results rely on combining their data with external data and the degeneracies between neutrino mass and other ΛCDM parameters, particularly σ_8. Furthermore the extracted neutrino mass depends on the particular lensing model employed and the Planck data are already close to the bounds of predicted lensing [41]. Operating at the edge of a bound provides a steep prior that artificially constrains the neutrino mass.

While astrophysics and cosmology provide information about neutrino mass they would benefit from a laboratory measurement. Being able to fix the value of the neutrino mass would allow them to remove degeneracies and further constrain the desired physical effects such as the dark energy density. With limited cosmological data it is important to make the best use of it. An outside measurement of the neutrino mass would help extend the reach of cosmological experiments by reducing correlation.

1.5 Direct neutrino mass experiments

The most direct approach to measuring the neutrino mass is measurement of the distortion near the beta endpoint in tritium decay. The long and rich history of early tritium-based experiments to measure the absolute mass of the neutrino was reviewed by Robertson and Knapp [10]. Otten and Weinheimer [42] discuss more recent experimental progress.

The earliest tritium-based neutrino mass experiments were 1940s gas proportional counter experiments [43, 44]. The efforts of Hanna and Pontecorvo were plagued by poor resolution that prevented them from setting an upper limit. Although Curran, Angus and Cockcroft [44] set an upper limit of 1 keV, their result contained ambiguity about the endpoint. A series of experiments using similar approaches followed with upper limits based on the simple interpretation of the kinematics of the electron from a bare nuclear decay. In 1972 Bergkvist [45] set a 55-eV limit and noted that future progress was dependent on consideration of the spectral distortions arising from atomic and molecular excitations near the endpoint [46].

In 1980 a Los Alamos National Laboratory (LANL) experiment began construction of an experiment with a windowless, gaseous T_2 source [47, 48]. This experiment, motivated by Bergkvist's comments on atomic and molecular excitations, used a source for which ab initio calculations are viable. The gaseous nature of the source also limited the effects of scattering within the source. A concurrent tritiated-valine experiment reported a 30 eV neutrino mass [49] that sparked worldwide interest because the value implied closure density for primordial electron-flavor neutrinos. The LANL experiment, however, refuted the claimed measurement, setting an upper limit of 9.3 eV at the 95% confidence level [48]. The LANL results, however, had a 2-standard-deviation excess of events in the endpoint region. Following the LANL limit, a Lawrence Livermore National Laboratory (LLNL) used a windowless, gaseous T_2 source to set a limit of 8.3 eV with a significant excess of events near the endpoint [50].

At the same time the LANL and LLNL experiments were using T_2 sources, many other experiments around the world were using complex tritium sources to search for neutrino mass. The results of the Beijing [51], Tokyo [52] and Zürich [53] experiments were all consistent with zero neutrino mass but provided central values in the unphysical regime with $m_\nu^2 < 0$. The negative-mass-squared problem further motivated experiments using T_2 sources and further theoretical work on the molecular final-state distribution followed (Sec. 2.2).

The present Particle Data Group evaluated limit of $m_\nu < 2$ eV at an unstated confidence level is a combination of results from Mainz [54] and Troitsk [55, 56]. Both experiments employed a magnetic-adiabatic-collimation-with-electrostatic (MAC-E) filter [57] spectrometer in which the momenta of the beta electrons are rotated as the particles are guided from high to low magnetic field regions. The momentum collimation of the beam results in both a wide spatial spread and a means of electrostatic filtering with a longitudinal potential.

The Mainz experiment employed a solid source consisting of T_2 films quench-condensed onto substrates of highly oriented pyrolytic graphite. Dewetting of the lattice, lattice relaxation following decay and other solid-state source effects were carefully considered in the Mainz analysis. The final Mainz limit was $m_\nu < 2.3$ eV at 95% confidence [54].

The Troitsk experiment, like its predecessors at LANL and LLNL, employed a windowless, gaseous tritium source. In early runs a mass analyzer at the source and count-rate measurements at a low retarding-potential setting allowed indirect monitoring of the source gas density. In later runs an electron gun mounted upstream of the source provided scattering measurements to determine the column density. The initial Troitsk analysis involved a step function added to the standard spectral shape [55] (the so-called "Troitsk Anomaly"). The final result was based on the subset of runs for which the electron gun scattering measurements were available. The final Troitsk limit was $m_\nu < 2.05$ eV at 95% confidence [56] using the Feldman-Cousins

method [58].

1.6 Future prospects for direct neutrino-mass experiments

As the sensitivity of T_2-based experiments improves, an accurate understanding of the role of molecular final states after beta decay becomes more important. The key role of the final states as a source of systematic uncertainty has been a major motivator in the search for other experimental approaches to direct neutrino mass measurement. Microcalorimters and atomic traps have been considered as alternatives to the traditional beta spectrometer approach.

The use of a microcalorimeter to record the energy released in the decay has the advantage that (with some experimental caveats) all the energy released is captured and totaled for each event, except for the energy carried away by the neutrino. The final-state distribution is therefore not needed unless it significantly modifies the available lepton phase space. In principle this approach can be applied to the decay of tritium, but in practice the population of the part of the phase space sensitive to neutrino mass is too small for this method to be used. Microcalorimeters must faithfully analyze every decay because there is no preselection possible. In the presently interesting range for neutrino mass, more than 10^{13} events would need to be recorded in a tritium-based calorimeter experiment. With such high statistics pileup becomes a troublesome source of systematic error and very small calorimeters are needed. Two nuclei with lower Q-values have therefore received more attention because the fraction of decays leading to the region of interest improves inversely as the cube of the Q-value.

The isotope ^{187}Re decays by a forbidden transition $^{187}\mathrm{Re} \rightarrow {}^{187}\mathrm{Os} + \beta + \bar{\nu}_e$, with an endpoint energy of 2.47 keV, 7.5 times lower than that of tritium beta decay [59]. The Microcalorimeter Arrays for a Rhenium Experiment (MARE) collaboration has worked to improve the sensitivity of cryogenic bolometers with ^{187}Re in the absorbers [60]. Given the ^{187}Re half-life of 4.5×10^{10} years, large amounts of the

isotope are required to achieve reasonable statistics near the endpoint, and numerous independent detectors are needed in order to avoid pileup in any individual bolometer. Any neutrino-mass measurement with a solid ^{187}Re source must also account for spectral distortion due to the beta environmental fine structure, resulting from interference between the outgoing beta wave and its reflection from nearby atoms in the lattice [61].

For these reasons, attention has turned to a very different prospect, the electron-capture decay of ^{163}Ho, which has a half-life of about 4750 years. The ^{163}Ho electron-capture Q-value is not well known but measurements fall within a few hundred eV of 2.5 keV [62]. The experiment consists of a calorimetric measurement of the visible energy released in the decay $^{163}\mathrm{Ho}^{+} + e^{-} \rightarrow {}^{163}\mathrm{Dy}_{i}^{*} + \nu_{e}$. To first order, the neutrino spectrum is a series of narrow lines corresponding to electron capture from various atomic subshells. However, because vacancies in those subshells have non-zero widths reflecting their short lifetimes, there is a continuum of visible energy extending to the Q-value. A non-zero neutrino mass modifies the spectral shape at the endpoint just as it does in beta decay [63]. The scaling difficulties of a rhenium experiment are somewhat mitigated by the shorter half-life, but significant uncertainties in the deexcitation spectrum [64] and ^{163}Ho production remain to be resolved. A holmium-based approach is under investigation by the HOLMES [63], the Electron Capture ^{163}Ho (ECHo) [65], and the LANL [66] collaborations.

The beta decay of tritium remains the major focus of experimental work on direct measurement of neutrino mass. The largest and most sensitive such experiment yet is the KATRIN (KArlsruhe TRItium Neutrino mass) project. Scheduled to begin taking data in 2016, KATRIN will be sensitive to a neutrino mass of 0.2 eV at the 90% confidence level [11]. Fig. 1.2 shows a layout of the KATRIN experiment. the beta electrons from the windowless, gaseous molecular tritium source are adiabatically guided to a set of spectrometers that act as high-pass filters. The electrons passing the filters are magnetically guided to a silicon detector for counting. The experiment

maps the integrate beta spectrum as a function of spectrometer settings.

In KATRIN, stringent control of many kinds of systematic uncertainty is needed if the projected sensitivity is to be achieved. The molecular final-state distribution populated by T_2 decay represents one of the larger potential sources of systematic error in KATRIN. A 1% uncertainty in the calculated width of the ground-state molecular rotation and vibration distribution would contribute 6×10^{-3} eV^2 to the standard deviation of the square of the neutrino mass, $\sigma(m_\nu^2)$, the largest single contribution to the identified systematic uncertainty of approximately 10×10^{-3} eV^2 for the entire KATRIN experiment [11].

Other major sources of systematic uncertainty for KATRIN are more amenable to experimental control [11]. An electron gun behind the 10^{11}-Bq windowless, gaseous T_2 source will allow calibration of the experimental transmission function and of the energy loss experienced by betas traveling through the source. The retarding potential of the KATRIN MAC-E filter will be independently monitored by the refurbished spectrometer from the Mainz experiment [68] and by a high-voltage divider with a demonstrated stability of 6.0×10^{-7} per month [69]. Fluctuations in the column density of the source, which affect the scattering probability for betas exiting the source, will be limited to the 0.1% level through control of the tritium injection rate, the pumping speed, and the vessel temperature; a temperature stability of $\Delta T/T = 5 \times 10^{-5}$ per hour has been demonstrated with a prototype system [70]. The isotopic composition of the source gas will be monitored via Raman scattering in the tritium recirculation loop that feeds the source [71].

The KATRIN main spectrometer represents the practical limit of MAC-E filter technology given the size of the spectrometer and source; subsequent tritium-based neutrino-mass experiments require the development of new techniques. Additionally KATRIN operates at the maximum source density tolerable given the electron scattering cross section. Increased statistical precision would require scaling up the already prohibitively large cross-sectional area of the source and spectrometer. In an

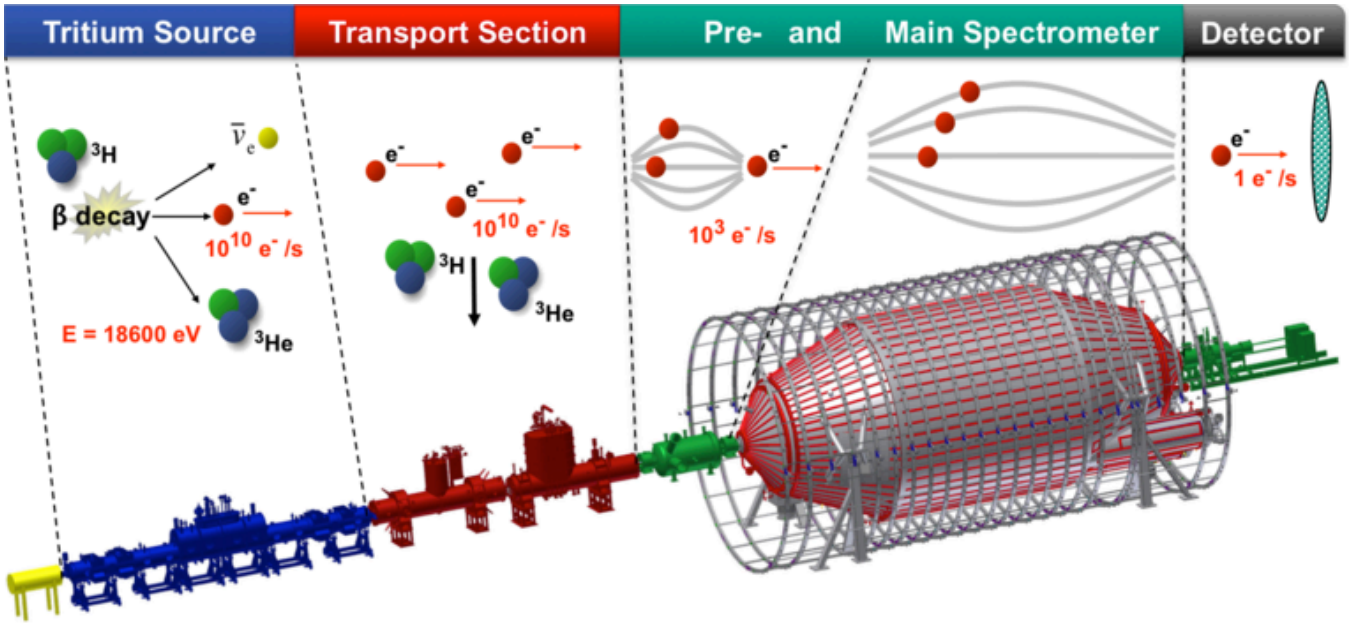

Figure 1.2: Layout of the Karlsruhe Tritium Neutrino Experiment, the next-generation, tritium-beta-decay neutrino-mass experiment. Figure from the Karlsruhe Institute of Technology KATRIN website [67].

effort to circumvent these limitations, the Project 8 collaboration is currently constructing a prototype for studying the feasibility of trapping betas and determining their energies by measuring their cyclotron radiation frequencies with microwave antennae [72]. Monreal and Formaggio report that the experiment could tolerate a T_2 source activity of up to $\sim 10^9$ Bq with acceptable accidental rates and energy losses, however, substantial research and development are required [73, 74]. In its use of a T_2 source, Project 8 also requires an accurate quantitative description of the molecular final states of the source. The collaboration is also studying the possibility of building an atomic T source by magnetically trapping single atoms as well as emitted betas.

The novel approach of trapping *atomic* tritium in order to detect the beta and recoil $^3He^+$ ion in coincidence was proposed by Jerkins *et. al.* [75]. Such an approach relies on the ability to simultaneously measure the momentum of both charged decay products as well as the beta energy. Given sufficient precision on the momenta and energy the neutrino mass can be reconstructed, however, this approach relies on a number of technical advancements that seem unlikely to come to fruition. Otten [76] criticized the original concept paper for ignoring field variations and not identifying a sufficiently precise beta spectrometer. The validity of these concerns was conceded by Jerkins *et. al.* [77] and there have been no further publications on the subject.

Studying tritium beta decay remains the most promising method of improving the neutrino-mass sensitivity within the laboratory. The upcoming KATRIN experiment represents the culmination of the current approach. If KATRIN provides an upper limit at the projected sensitivity, new techniques will be needed to probe the remaining order of magnitude. Several groups are investigating new techniques to improve the sensitivity.

Chapter 2

MOLECULAR TRITIUM DECAY AND NEUTRINO MASS MEASUREMENTS

Molecular tritium beta decay is the favored method of direct meaurement of the neutrino mass. This chapter lays out the aspects of beta decay that are relevant for neutrino mass, particularly the role of molecular excitations and is based on our recent publication [4] on molecular final state effects in neutrino mass measurements. The figures that are reproduced include citations indicating their origin in the published work.

2.1 Beta Decay and Neutrino Mass

Tritium (T), an unstable neutron-rich isotope of hydrogen, undergoes nuclear beta decay, converting to $^3He^+$ by releasing an electron (β) and electron antineutrino. The energy released in the decay is 18.6 keV, a relatively low Q-value for beta decay. The 12.3 year half-life is reasonably short, allowing the construction of sources with high specific activity.

The well-known form of the tritium beta spectrum is illustrated schematically in Fig. 2.1 for massless neutrinos and for 1-eV neutrinos. It is the task of the experimentalist to measure the spectral shape and thereby determine the neutrino mass. Only a fraction of order 10^{-13} of the decays populate the last 1 eV of the beta spectrum. Uncertainty on the Q-value and practical experimental challenges preclude fixing the endpoint energy during data analysis and it therefore must be treated as a 'nuisance parameter.' Furthermore, the spectral distortion due to the neutrino mass is small and distortions of similar size can arise from a number of theoretical corrections and

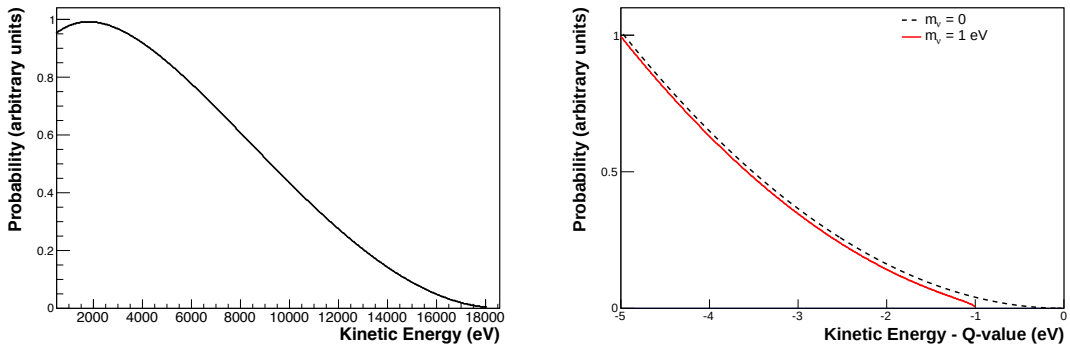

Figure 2.1: Tritium beta spectrum with 3 active neutrinos with masses $m_{\nu i} \simeq 1$ eV for the case of no daughter excitation. The left panel shows the full spectrum. The right panel shows the last 5 eV before the endpoint, with the dotted curve indicating the spectral shape for $m_{\nu i} = 0$.

from instrumental effects. For a molecular tritium source, the largest modifications to the spectrum are caused by excitations of the daughter molecule formed in the decay, which at present must be calculated from theory. One could consider using a non-molecular source, such as T^+ or T, but these are far less practical due to space-charge limitations and the high reactivity of atomic hydrogen.

The ongoing construction of the Karlsruhe Tritium Neutrino experiment (KATRIN) [11], the next-generation tritium-based neutrino-mass experiment, has renewed interest in the molecular final-state distribution (FSD) populated by T_2 beta decay [42]. With a design neutrino-mass sensitivity of 0.2 eV, KATRIN depends critically on a theoretical understanding of molecular effects. Accordingly, extremely precise, *ab initio* calculations of the molecular final-state spectrum have been performed [1, 9] in the region of interest for KATRIN, near the endpoint of the beta electron energy spectrum. A direct experimental verification of these calculations through a study of the molecular final-state spectrum itself is not practical as explained in Sec. 2.4. Indirect tests can be performed, but have yielded mixed results.

Although most of the spectrum of the HeH^+ isotopolog is inaccessible to experiment, many predicted spectral features have been observed in emission; HeH^+ photodissociation measurements are also compatible with theory, although a high-precision test has yet to be performed. On the other hand, measurements of the branching ratio of T_2 to the bound molecular ion $^3HeT^+$ following beta decay – another observable indirectly related to the final-state distribution – show stark disagreement with predictions.

2.1.1 Theory of beta decay

Tritium decay is well described by the Fermi theory of beta decay. Tritium and helium-3 are mirror nuclei thus the nuclear matrix element M_{nuc} is maximal. The transition is allowed, and the spectrum is not significantly modified by a shape factor dependent on the kinetic energy of the electron. Hence the shape of the beta decay spectrum is determined by the neutrino mass m_ν; electron mass m_e; total electron energy E_e; maximum energy of the electron, $E_{\text{max}} = Q - E_{\text{rec}}^{\text{kin}} + m_e$; and the energies V_k and probabilities P_k associated with excitations of the daughter ion. The recoil energy $E_{\text{rec}}^{\text{kin}}$ consists of translational kinetic energy of the daughter ion. Since the discovery of neutrino oscillations shows there are three different neutrino eigenmasses ($m_{\nu i}$), the full spectrum becomes an incoherent sum over individual spectra for mass index $i = 1, 2, 3$, with intensities given by the squares of the neutrino mixing matrix elements (U_{ei}) [78]. The resulting distribution of the electron energy E_e is shown in Eq. 2.1, in which G_F is the Fermi weak-coupling constant, θ_C is the Cabibbo angle, $F(Z, E_e)$ is the Fermi function correcting for the interaction between the electron and the nucleus, and $\Theta(E_{\text{max}} - E_e - V_k - m_{\nu i})$ is a Heaviside step function ensuring energy

conservation [10]. Units are chosen where $c = 1$.

$$\begin{aligned}\frac{dN}{dE_e} =& \frac{G_F^2 m_e^5 \cos^2\theta_C}{2\pi^3\hbar^7}|M_{\rm nuc}|^2 F(Z,E_e)p_e E_e \\ &\times \sum_{i,k}|U_{ei}|^2 P_k(E_{\rm max}-E_e-V_k)\sqrt{(E_{\rm max}-E_e-V_k)^2-m_{\nu i}^2} \\ &\times \Theta(E_{\rm max}-E_e-V_k-m_{\nu i})\end{aligned} \tag{2.1}$$

A number of small corrections to this basic spectral form have been identified over the years and have been summarized by Wilkinson [79]. At the time of his work, the effects he enumerated were for the most part negligible, but as experimental precision has advanced, their significance has as well. Radiative corrections are the most important and have subsequently been re-examined [80]. A comprehensive and fully relativistic treatment of weak magnetism and induced terms may be found in Ref. [81].

Formally, Eq. 2.1 also contains inaccuracies in its treatment of rotational and vibrational molecular excitations. The mass of the nucleus is considered to be infinite in deriving the electron-neutrino phase space, and nuclear recoil is then treated separately in determining the molecular translation, rotation, and vibration in the final state. Electronic excitations represent energy unavailable to the outgoing leptons, and the modification to the phase space is appropriately captured by the appearance of V_k in expressions for the electron energy. However, a correct treatment of rotational and vibrational excitations becomes ambiguous inasmuch as the appropriate recoil mass is not defined. In addition, the center-of-mass frame invoked for the decay described by Eq. 2.1 is not related in any simple way to the center of mass of an object more complex than an isolated atom. In a molecule, the atoms are always in motion, a source of Doppler broadening for the observed electron. These issues can be avoided by consideration in a relativistic formalism of the full three-body phase space populated in the decay.

Because of the momentum imparted by the leptons to the recoil nucleus, the phase

space is three-body rather than two-body everywhere except at the endpoint. While it is standard to neglect this effect, doing so introduces a small spectral distortion. More importantly, the three-body form permits a self-consistent treatment of recoil effects. The spectrum endpoint is given without ambiguity for any molecular system by conservation of the four-momentum for the full system. An exact three-body, fully relativistic calculation for the phase-space density has been given by Wu and Repko [82] (see also Masood *et al.* [83] and Simkovic *et al.* [81]):

$$\begin{aligned}\frac{dN}{dE_e} &= CF(Z,E_e)\frac{p_e E_e}{\epsilon^2}\left(1-\frac{E_e}{M}\right) \\ &\quad\times\sum_i (\Delta_i - E_e)|U_{ei}|^2\left[(\Delta_i-E_e)^2 - m_{\nu i}^2\epsilon^2\right]^{1/2}\Theta(E_{ei,\max}-E_e) \qquad (2.2)\end{aligned}$$

with the following definitions:

$$C = \frac{G_F^2 m_e^5 \cos^2\theta_C}{2\pi^3\hbar^7}|M_{\rm nuc}|^2 \qquad (2.3)$$

$$\Delta_i = \frac{1}{2M}(M^2 - M_{(f)}^2 + m_e^2 + m_{\nu i}^2) \qquad (2.4)$$

$$E_{ei,\max} = \frac{1}{2M}(M^2 - M_{(f)}^2 + m_e^2 - m_{\nu i}^2 - 2m_{\nu i}M_{(f)}) \qquad (2.5)$$

$$\epsilon = 1 - \frac{2m_e}{M} + \frac{m_e^2}{M^2}. \qquad (2.6)$$

We have here generalized Wu and Repko's result by introducing multiple neutrino mass eigenstates $m_{\nu i}$. The mass M ($M_{(f)}$) is the mass of the initial (final) atom or molecule, including associated atomic electrons and any excitation energy that may be present. The quantity Δ_i, an experimentally useful fit parameter, is the 'extrapolated endpoint energy' that is obtained when the neutrino mass in the term in square brackets in Eq. 2.2 is set to zero. The quantity $E_{ei,\max}$ is the maximum energy of the electron for each neutrino eigenmass [84]. The electron-neutrino correlation modifies the spectrum at recoil order ($\sim m_e/M$) [81] and is not included here.

Both initial- and final-state excitations can now be introduced explicitly by indexing M and $M_{(f)}$ to become M_j and $M_{(f)k}$, respectively. For each pair of initial and

final states jk there is a corresponding Q-value,

$$Q_{kj} \quad = \quad M_j - M_{(f)k} - m_e \tag{2.7}$$

which is the kinetic energy released in the transition in the absence of neutrino mass. A special case is the atomic mass difference between the neutral atoms T (mass $M_0 = A$) and ^{3}He (mass $M_{(f)0} + m_e = A'$) in their ground states, which we denote Q_A:

$$Q_A \quad = \quad A - A'. \tag{2.8}$$

This corresponds to the Q-value for bound-state beta decay from ground state to ground state, the kinetic energy being delivered entirely to the neutrino and recoil. (The term "Q-value" without qualification is used inconsistently in the literature, sometimes meaning Q_{00} and sometimes Q_A. For the atomic case, those quantities differ by the single-ionization energy of He, 24.59 eV.)

In the general case the masses M_j and $M_{(f)k}$ can be related to atomic masses by accounting for electron binding energies and for the possible presence of other atoms in the molecule:

$$M_j \quad = \quad A_s + A - b_j \tag{2.9}$$

$$M_{(f)k} \quad = \quad A_s + A' - b_{(f)k} - m_e \tag{2.10}$$

$$Q_{kj} \quad = \quad Q_A - b_j + b_{(f)k}. \tag{2.11}$$

Here, the binding energies b_j and $b_{(f)k}$ are the energies released in transforming an atomic mass to the species of the parent or daughter, and the atomic mass of the other, 'spectator,' nucleus in the molecule (if present) is denoted A_s. For example, the binding of two neutral tritium atoms to form a neutral T_2 molecule in its ground state occurs with the release of $b_0 = +4.59$ eV. Figure 2.2 is a graphical summary of the relevant binding energies.

The extrapolated endpoint energy Δ_{ikj} can be expressed in terms of the corresponding Q-value:

$$\Delta_{ikj} \;=\; Q_{kj} + m_e - \frac{Q_{kj}}{2M_j}(Q_{kj} + 2m_e) - \frac{m_{\nu i}^2}{2M_j}. \tag{2.12}$$

The extrapolated endpoint still has a dependence on neutrino mass, but it is completely negligible so the mass-eigenstate subscript i on Δ will be omitted henceforth. The recoil-order term is small, a few parts in 10^4 of Q_{kj}. Thus the extrapolated endpoint energy Δ_{kj} for excited final states ($\lesssim$ 100 eV) can be taken to be the ground-state quantity Δ_{0j} minus the excitation energy.

Weighting each transition by a matrix element W_{kj} for the transition connecting the specific initial state j to the final state k, the spectral density becomes

$$\begin{aligned}\left(\frac{dN}{dE_e}\right)_{kj} \;=\; & CF(Z,E_e)\,|W_{kj}|^2\,\frac{p_e E_e}{\epsilon_j^2}(\Delta_{kj}-E_e)^2\left(1-\frac{E_e}{M_j}\right)\times \\ & \times\sum_i |U_{ei}|^2\left[1-\frac{m_{\nu i}^2\epsilon_j^2}{(\Delta_{kj}-E_e)^2}\right]^{1/2}\Theta(E_{ei,\max(kj)}-E_e).\end{aligned} \tag{2.13}$$

An expression for the matrix element W_{kj} is given in Eq. 2.16 in Sec. 2.2.

The maximum kinetic energy $E^{\rm kin}_{{\rm rec},\max(kj)}$ imparted to the recoil atom or molecule is the difference between the extrapolated endpoint energy and the available mass energy in the decay:

$$E^{\rm kin}_{{\rm rec},\max(kj)} \;=\; \frac{Q_{kj}}{2M_j}(Q_{kj}+2m_e) \tag{2.14}$$

A correct evaluation of the recoil energy is important because, as will be shown, the variance of the final-state distribution in the ground electronic state is directly proportional to it.

Table 2.1 summarizes the values of these parameters for several parent species[1], evaluated using the atomic mass difference Q_A = 18591.3(10) eV given by Audi,

[1]The sources considered here are those that have been suggested for neutrino-mass measurements. While relevant to the discussion of a real source, the decays of ionized molecules is beyond the scope of this work.

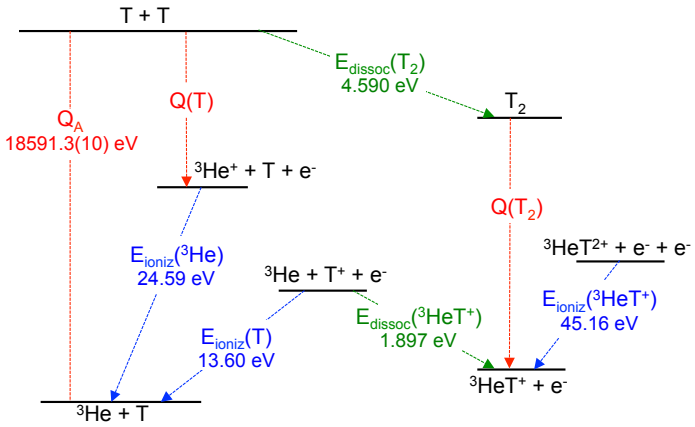

Figure 2.2: Energy levels relevant to atomic and molecular tritium decay, patterned after Fig. 5 in Otten and Weinheimer [42]. The mass difference Q_A is taken from Audi, Wapstra, and Thibault [85]. Dissociation energies are derived from calculations by Doss [3]; the ionization energy of $^3HeT^+$ is from calculations by Kołos *et al.* [86]. The ionization energies for T [87] and for ^{3}He [88] are taken from recent compilations. (Figure made by D. S. Parno for reference [4].)

Wapstra, and Thibault [85]. In ref. [89] a more recent measurement and a discussion of the experimental status of Q_A are presented.

In particular, it may be seen from the table that the endpoint energy for HT falls about 0.8 eV below that for T_2, and the endpoint energy for DT is intermediate between the two. However, the same underlying kinematics produce a compensating energy shift in the final-state distribution, as described in Sec. 2.3.

2.1.2 Molecular Tritium Beta Decay

The beta decay of a bound tritium atom differs from that of a free tritium atom in the existence of rotational and vibrational states that can be excited in the decay. For parent molecules in the ground state, the spectrum of states excited in the decay appears Gaussian (on the 0.1-eV scale) with a central value of 1.7 eV and a standard

Table 2.1: Values in eV of the binding energies, Q-values, extrapolated endpoint energies, and maximum recoil translational energies for five tritium-containing parents. All of the quantities in the last three lines have the fractional uncertainty of Q_A.

Quantity	Parent				
	T^+	T	HT	DT	T_2
b_0	-13.61	0	4.53	4.57	4.59
$b_{(f)0}$	-79.01	-24.59	-11.77	-11.73	-11.71
Q_{00}	18525.85	18566.66	18574.96	18574.95	18574.95
$\Delta_{00} - m_e$	18522.44	18563.25	18572.40	18572.91	18573.24
$E^{\text{kin}}_{\text{rec,max}(00)}$	3.402	3.409	2.557	2.045	1.705

deviation of 0.3 eV. Additionally the recoil energy of $^3HeT^+$ from molecular decay is decreased by a factor of 2 over the recoil energy of $^3He^+$ from atomic tritium decay. The differences in kinematics are visible in the slope and endpoint of the beta spectrum as indicated by eqn. 2.1.

The molecular states can be fully specified by electronic (n), vibrational (v), rotational (J) and azimuthal (M) quantum numbers. In addition the total nuclear spin can take on two values: spin-1 (ortho) and spin-0 (para). The ortho state is a triplet corresponding to the molecular state that is symmetric under exchange of the tritium nuclei. The para state is a singlet corresponding to the molecular state that is antisymmetric under exchange of the tritium nuclei.

In accordance with Fermi statistics the molecular wavefunction must be antisymmetric under exchange of the two tritium nuclei. The electronic, azimuthal and vibrational wavefunctions of the molecule are inherently symmetric. Thus the symmetric ortho state requires an antisymmetric spatial wavefunction, corresponding to odd J. The antisymmetric para state requires a symmetric spatial wavefunction, cor-

responding to even J. Hence the para state is the ground state of the molecule and even the lowest lying ortho state is excited by a few meV.

For a given initial state i T_2 and a given final state f of $^3HeT^+$ the probability of a transition is given by the square of the overlap integral:

$$P_{if} = |\langle \Psi_f^{^3HeT^+} |\, e^{i\boldsymbol{k}\cdot\boldsymbol{R}} \,| \Psi_i^{T_2} \rangle|^2. \tag{2.15}$$

The recoil motion of the ion is accounted for as an exponential of the dot product of recoil momentum and the nuclear separation. The initial state strongly impacts the final-state distribution populated by the decay and the characteristics of the tritium source must be well known in order to interpret the slope of the beta spectrum in terms of the neutrino mass.

High-precision, *ab initio* calculations of the molecular excitations arising from T_2 beta decay have been performed [1, 9]. The calculations use the Born-Oppenheimer approximation to factorize the molecular wavefunctions into electronic wavefunctions, vibrational wavefunctions and spherical harmonics dependent on the rotational and azimuthal quantum numbers. Hyperfine structure is neglected except where spin symmetry must be respected in homonuclear systems. Corrections to the Born-Oppenheimer and other approximations have also been investigated and found to be small [90].

2.2 Molecular Final State Distribution

2.2.1 Geminal-basis method

Theoretical investigations of beta decay in T_2 date back to the pioneering work of Cantwell in 1956 [91]. Modern calculations are built on the theoretical framework of Kołos and Wolniewicz, who developed an adiabatic description of the hydrogen molecule in a basis of explicitly correlated two-electron wavefunctions in 1964 [92]. This basis is sometimes described as geminal because it treats the electrons as a pair rather than as independent particles. Development of the geminal basis for the

hydrogen molecule led to early calculations of the molecular effects in the decay of HT [93]. In a further refinement of the basis, Kołos *et al.* [86] investigated optimal parameter values. The most recent calculations rely on those results with minor additional refinements [1].

As Jonsell, Saenz, and Froelich [90] show, the transition matrix element related to the final-state $^3HeT^+$ excitation $k \equiv (v_{(f)}, J_{(f)}, M_{(f)}, n_{(f)})$ from an initial T_2 state $j \equiv (v, J, M, n)$ may be written,

$$|W_{kj}(K)|^2 = \left| \int \left[\chi^{n_{(f)}}_{v_{(f)} J_{(f)} M_{(f)}}(\mathbf{R}) \right]^* S_n(R) e^{i\mathbf{K}\cdot\mathbf{R}} \xi^n_{vJM}(\mathbf{R}) d^3R \right|^2 . \quad (2.16)$$

In this expression, χ and ξ are the rotational-vibrational wave functions of the $^3HeT^+$ and T_2 molecules, respectively, and $S_n(R)$ is an electronic overlap integral. The exponential of the dot product of the recoil momentum $\mathbf{K}$ and the nuclear separation $\mathbf{R}$ is a consequence of the recoil motion of the daughter He nucleus.

The reduced mass of the daughter molecule enters into the radial Schrödinger equation, which must be solved in order to compute the rotational and vibrational energy levels. There is some ambiguity in the definition of this quantity, which depends on whether and how the masses of the two bound electrons are included. Coxon and Hajigeorgiu [94], comparing predicted energy levels to spectroscopic measurements (Sec. 2.4.1), achieved the best agreement with an effective reduced mass that assumes one electron belongs strictly to the He nucleus, with the second electron distributed evenly between the H and He nuclei. Doss *et al.* [9], confirming this result, introduced the effective reduced mass to the calculation of the final-state distribution, but noted that the change was insignificant at the 0.1-eV level of foreseeable T_2-based neutrino-mass measurements.

Fig. 2.3 shows the spectrum of final-state molecular excitations from the beta decay of T_2 ($J = 0$ initial state) as published by Saenz *et al.* in 2000 [1], compared with the 1985 calculation by Fackler *et al.* [2]. The electronic ground state appears as

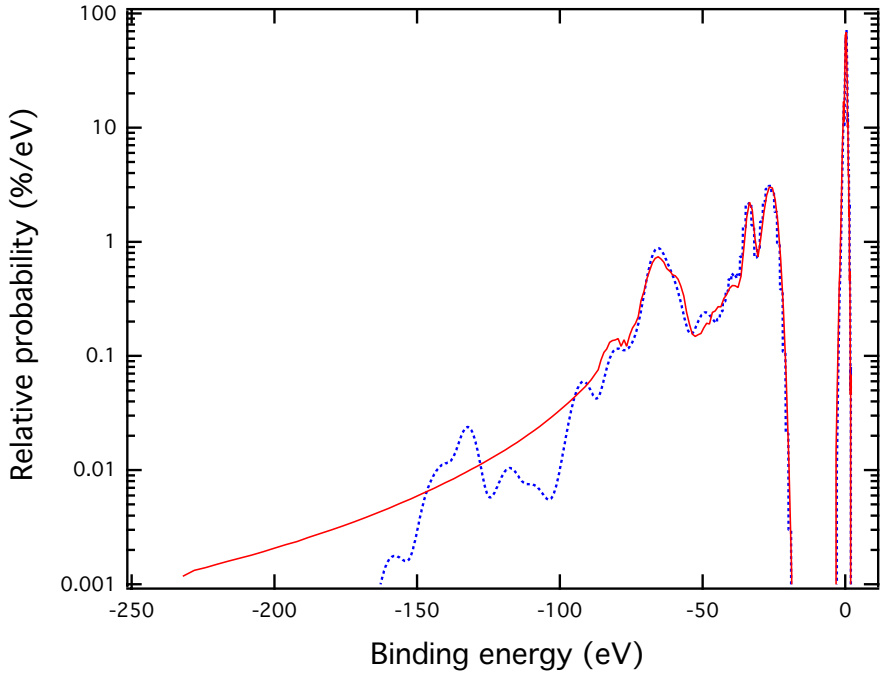

Figure 2.3: Molecular spectrum excited in the beta decay of T_2 ($J = 0$) as calculated by Saenz *et al.* [1] (solid curve, red online) and by Fackler *et al.* [2] (dotted curve, blue online). For the purposes of display and comparison, discrete states in the latter spectrum have been given a Gaussian profile with a standard deviation of 3 eV. (Figure made by R. G. H. Robertson for reference [4].)

a large peak centered at 0.2 eV binding energy (1.7 eV excitation energy), broadened by the rotational and vibrational excitations. The higher electronic states also suffer broadening as shown. For a detailed description of the differences between the Saenz and Fackler calculations see reference [1]. The more recent results of Doss *et al.* [9] were not published in tabular form but a subset of the tables was provided to the KATRIN collaboration courtesy of Doss. Reference [3] compares the Doss *et al.* [9] results and the Saenz *et al.* [1] results. The differences are negligible for the ground state but noticeable in the electronic continuum, particularly above 45 eV of excitation

energy (see Sec. 2.2.3).

Unfortunately, in the geminal basis the convergence of the calculations depends on the explicit choice of basis functions and in-depth study has revealed that adding even one basis function can dramatically change the contributions of other functions [95]. Significant optimization work was done to select the correct basis functions for T_2 and $^3HeT^+$ and provide reliable results [86]. In lieu of explicitly computing uncertainties, which is impractical due to the volatility of the basis, published calculations typically report the deviation from 1 of the cumulative probability function at the highest excitation energy. However, this single number, while informative, is an insufficient gauge of accuracy. Despite the linear dependences and instability of the geminal basis, it has been used to produce essentially all final-state distribution calculations of the ground-state manifold since its publication [9, 1].

2.2.2 Configuration-interaction method

The configuration-interaction (CI) method presents an alternative approach to modeling two-electron, diatomic molecules such as T_2 and $^3HeT^+$ within the Born-Oppenheimer approximation. In the CI technique, two-electron configurations are constructed as the products of pairs of solutions to the single-electron Schrödinger equation (denoted orbitals). Superpositions of these configurations are then used to build wavefunctions and make calculations. As the simplest two-electron heteronuclear molecule, HeH^+ was an early test bed for the method (see, *e.g.*, [96, 97, 98]). In the 1980s, parallel to the refinement of the geminal-basis method, the CI method was applied to the FSD following beta decay in T_2. Fackler *et al.* [99] performed a preliminary study of decays to the first five electronic states of $^3HeT^+$; Martin and Cohen [100] used a more flexible basis set of Cartesian Gaussian orbitals to study the first 50 eV of the electronic continuum. (See Sec. 2.2.3.) Without the benefit of modern computation, however, such early treatments were neither complete nor precise enough to address the final-state spectrum in the region of interest for modern tritium-based

neutrino-mass experiments such as KATRIN.

More recently, Vanne and Saenz [101] have developed a CI approach, based on an underlying B-spline basis set and carried out in an elliptical box, that shows promise for neutrino-mass experiments. This method avoids the linear dependences that tend to arise in numerical calculations with the geminal-basis method, allowing application to larger internuclear distances R as well as the use of larger basis sets. Adding individual basis functions does not introduce artificial resonances. The discretization provided by the elliptical box allows the electronic continuum to be discretized as well, permitting the consideration of both bound and continuum states within the same basis set. Since all configurations are expressed in terms of one-electron wavefunctions, however, two-electron correlations are treated less accurately than in the geminal-basis method, especially if the configuration set is small.

Vanne and Saenz have compared their B-spline-based CI treatment of HeH^+ photoionization [101] against one using the standard geminal basis [102]. The first resonance in the $X^1\Sigma \rightarrow {}^1\Sigma$ photoionization cross section, at about 16 eV, is shifted about 0.5 eV higher in the CI results, likely due to the difference in treating two-electron correlations. The two approaches predict the same amplitude for this resonance and give good agreement for other features of the spectrum.

The application of this method to tritium beta decay is a work in progress [103]. Once sufficiently complete configuration sets are calculated for T_2 and for ${}^3HeT^+$, the electronic overlap integrals $S_n(R)$ can be computed. Transition probabilities may then be determined using Eq. 2.16.

2.2.3 Electronic continuum

The energy window for the KATRIN neutrino-mass measurement is narrow enough that related FSD calculations can focus on the ${}^3HeT^+$ electronic ground state. However, it has been suggested that a measurement of the tritium beta spectrum over a wider energy range could be used to search for sterile neutrinos with mass on the eV

scale [104] or even on the keV scale [105]. If the acquisition window extends more than about 40 eV below the beta endpoint, the analysis must account for the electronic continuum portion of the FSD. Table 2.2 gives a brief overview of the variety of methods that have been applied to the problem. In addition to their differences in general approach, the available calculations differ in baseline assumptions. Early calculations often used the clamped-nuclei approximation rather than explicitly accounting for nuclear motion that broadens resonances. Assumptions about the localization of resonances can introduce errors at higher excitation energies [106]. Variation of the internuclear distance shifts the overall probability distribution but can also change the relative intensities of the electronic resonances [107]. A significant simplification is possible at excitation energies above $\sim$ 200 eV, a region in which the fast-moving ejected electron sees the $^3He^{++}$ ion as equivalent to a bare He nucleus. The high-excitation-energy tail of the FSD can then be described with a spectrum adapted from the decay of atomic tritium [107].

The percentage of tritium decays that populate the electronic continuum is relatively consistent across calculations despite dramatic differences in the integration range, reflecting the fact that this region of the spectrum is dominated by a few autoionizing states near the ionization threshold. However, comparisons between different calculations, performed *e.g.* in Ref. [106] and [108], show significant discrepancies in the detailed structure of this part of the spectrum. For a sterile-neutrino search, knowledge of the integrated probability P_{cont} is not sufficient. If not properly accounted for, small structures in the FSD at high excitation energies could lead to errors in interpretation, especially when small mixing angles are considered. Sensitivity calculations for such a search must be guided by theoretical studies of this region of the FSD spectrum.

Table 2.2: Selected calculations of the probability P_{cont} of populating the electronic continuum of $^3HeT^+$ in T_2 beta decay. The integration range differs between the calculations, and the bounds are specified as excitation energies above the $^3HeT^+$ ground state.

Method	**Reference**	$\mathbf{P_{cont}}$	**Integration Range**
Complex scaling	Froelich *et al.* (1993) [108]	12.77%	$45 - 90$ eV
Stieltjes imaging	Martin and Cohen (1985) [100]	13.42%	$45 - 94$ eV
Stabilization	Fackler *et al.* (1985) [2]	14.2%	$45 - 200$ eV
R-matrix	Doss and Tennyson (2008) [106]	13.66%	ca. $40 - 240$ eV*

*Lower integration bound is not explicitly given.

2.2.4 Differences in excitations across tritium isotopologs

The tritium-containing hydrogen isotopologs (HT, DT and T_2) have different reduced masses and thus different excitation spectra. While the overall structure of the final-state spectrum remains qualitatively the same across isotopologs, the vibrational energy levels are shifted and the probability of a transition to any specific rotational-vibrational state changes. For example, the electronic excitations in $^3HeH^+$ are shifted ∼1 eV lower than the corresponding excitations in $^3HeT^+$ [90]. As shown in Table 2.1, however, the difference in recoil mass also changes the extrapolated endpoint, canceling the change in the beta energy to first order [11].

In addition to differences in reduced mass, nuclear spin and symmetry considerations play an important role in determining the allowed angular-momentum states of the homonuclear T_2 molecule but do not apply to the heteronuclear DT and HT molecules. In accordance with Fermi statistics, the ground state of the molecule is the para state with $J = 0$.

In thermal equilibrium the partition function of rotational states (J) in T_2 may be written,

$$Z_{\text{equil}} = \sum_{J=0}^{\infty} [2 - (-1)^J](2J+1)e^{-J(J+1)\hbar^2/2\mathscr{I}k_BT}, \tag{2.17}$$

to first order. Here the first factor is the spin statistical weight for ortho (odd J) or para (even J) in the case of a homonuclear molecule, when total antisymmetry must be enforced, and k_BT is the thermal energy. The moment of inertia, $\mathscr{I}$, is related to the energy of the first excited state, $E_{J=1}$,

$$\mathscr{I} = \frac{\hbar^2}{2E_{J=1}}. \tag{2.18}$$

Since $E_{J=1} = 0.00497$ eV [3] is small compared to k_BT at room temperature, the ortho-para ratio of a thermally equilibrated source at room temperature is essentially the ratio of the spin statistical weights, 3:1 [90]. Rather than the ortho-para ratio,

the state of a molecular hydrogen source is typically characterized in terms of the parameter λ quantifying the fraction of the source that is in the ortho state.

The ortho-para transition requires a simultaneous change in the spin and rotational quantum numbers, making the ortho state metastable. Thus transitions to lower rotational states are dominated by intrinsically slow quadrupole transitions. For this reason, unless specific steps are taken to ensure it, thermal equilibrium of the rotational states of T_2 cannot be guaranteed. Thermalization of the spin degrees of freedom in a homonuclear hydrogen source is a slow, exothermic process, and uncertainty arises from the use of sources that are not in thermal equilibrium and that contain a mixture of states. This complicates interpretations of tritium-based experiments, many of which use non-thermal sources. The KATRIN source will be flashcooled from room temperature and the travel time of molecules through the windowless, gaseous tritium source (WGTS) is short enough to assume the rotational states are out of equilibrium, i.e. in the room temperature 3:1 ratio.

Previous studies of molecular hydrogen have focused on the ortho-para ratio alone as the determining factor in the rotational-state distribution, a reasonable assumption for light isotopologs. However, for T_2 above cryogenic temperatures, states higher than $J = 1$ have significant populations and the evolution of the full rotational-state distribution must be considered. Spontaneous quadrupole transitions are extremely slow, on the order of 10^{-7} s^{-1} in free space [109], and transitions will be dominated by collisions with other tritium molecules and the walls. The rate of these processes depends on the detailed design of the gas system and must be carefully modeled to determine the rotational-state distribution of the source.

2.3 Conceptual model of the rotational-vibrational spectrum

As we have seen in Sec. 2.2, a precise treatment of the molecular final-state spectrum requires an extensive theoretical framework. However, as experimental sensitivity has advanced, dependence on the highly excited states has diminished. The width

of the ground-state manifold now sets the fundamental limit on the sensitivity of experiments using T_2. With the intention of gaining some insight into the physical origin of the width of this manifold we have developed a simplified treatment, based on kinematic considerations and the approximation of the molecule as a simple harmonic oscillator. It reproduces several features of the precisely calculated spectrum while clarifying the underlying physics.

Qualitatively, the beta spectrum is influenced in two distinct ways by the molecular structure. The rotational, vibrational and translational motions of the parent T_2 molecule lead to modulation of the energy of the detected beta electron. Some motions are essentially thermal in origin and contribute a Doppler shift in the laboratory electron energy. Classically, each degree of freedom contains on average $\frac{1}{2}k_BT$ of energy, and the atomic velocity adds vectorially to the electron velocity. Nevertheless, as we shall see, it is a uniquely quantum-mechanical effect, zero-point motion, that in fact dominates the spectrum at low temperatures.

In the following, our interest is in the rotational and vibrational degrees of freedom in the electronic ground state. We begin by examining the purely kinematic constraints on the recoil momentum $\mathbf{p} = \hbar\mathbf{K}$. We then, in a semiclassical approach, combine the initial momentum of the decaying T nucleus in the parent molecule with the momentum delivered by lepton recoil in order to find the momentum spectrum of the daughter ^{3}He. Applying kinematic constraints, the momentum spectrum is expressed in terms of the corresponding translational and excitation energies of the recoil molecular ion $^3HeT^+$ or $^3HeH^+$, for the parents T_2 and HT, respectively.

2.3.1 Recoil momentum

The three-momentum imparted to the molecular system by the beta decay has a magnitude

$$\begin{aligned} p &= |\mathbf{p_e} + \mathbf{p}_\nu| \\ p^2 &= E_e^2 - m_e^2 + (E_{ei,\max} - E_e - E_{\rm rec}^{\rm kin})^2 - m_\nu^2 \\ &\quad +2E_e(E_{ei,\max} - E_e - E_{\rm rec}^{\rm kin})\beta\beta_\nu \cos\theta_{e\nu} \end{aligned} \tag{2.19}$$

where $\theta_{e\nu}$ is the angle between the electron and the neutrino momenta, and β and β_ν are, respectively, the electron speed and neutrino speed relative to the speed of light. It is sufficient for the present purpose to neglect neutrino mass and also the kinetic energy of the recoil $E_{\rm rec}^{\rm kin}$, which contributes corrections of order $m_e/M \simeq 10^{-4}$ to the square of the recoil momentum.

The electron-neutrino correlation term may be written [110]

$$\left[1 + a_{e\nu}\frac{\mathbf{p_e}\cdot\mathbf{p}_\nu}{E_e E_\nu}\right] = 1 + a_{e\nu}\beta\cos\theta_{e\nu}. \tag{2.20}$$

Using for $a_{e\nu}$ the value measured for the free neutron, $a_{e\nu} = 0.105(6)$ [111], and noting that the electron velocity $\beta \leq 0.26$, one sees that the electron-neutrino correlation is very weak in tritium decay. The recoil-energy envelope for the decay of an isolated tritium nucleus is shown in Fig. 2.4.

Although the recoil momentum is given immediately from the lepton momentum via momentum conservation, determining the recoil *energy* requires knowledge of the (effective) recoil mass. In the case of an isolated T atom, shown in Fig. 2.4, the calculation is unambiguous, but for a T_2 molecule it is not. For a very tightly bound system with no accessible internal degrees of freedom the mass would be the total mass (6 u), and for a very weakly bound one it would be 3 u. Without further information, the recoil energy can be bounded above and below by kinematics and at these limits is entirely translational kinetic energy. At the endpoint of the beta

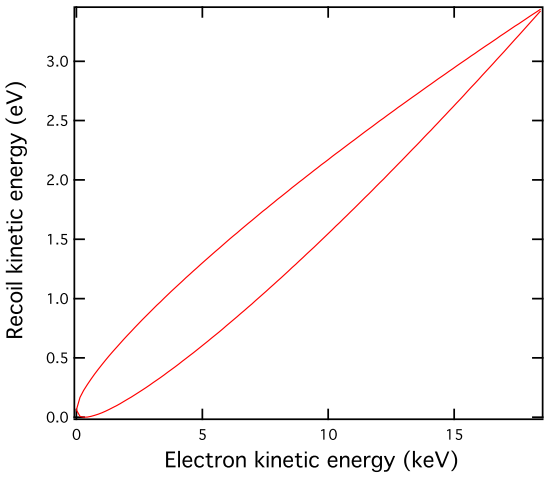

Figure 2.4: Recoil kinetic energy imparted to a ^{3}He daughter by the beta decay of an isolated tritium nucleus at rest. The upper boundary of the envelope corresponds to $\theta_{e\nu} = 0$ and the lower one to $\theta_{e\nu} = \pi$. (Figure made by R. G. H. Robertson for reference [4].)

spectrum,

$$1.705 \quad \leq \quad E_{\rm rec}^{\rm kin} \leq 3.410 \text{ eV}. \tag{2.21}$$

The ^{3}HeT$^+$ ion has a spectrum of rotational and vibrational excitations that are one or two orders of magnitude smaller than the recoil energy, less like the strongly bound picture and more like the weakly bound one. Some insight into the behavior of this system can be gained by considering first a purely classical T_2 molecule at 0 K, such that both atoms are bound together but at rest. If the molecule remains bound after beta decay, conservation of linear momentum requires that 1.705 eV must be in the form of translational kinetic energy, leaving only 1.705 eV available for internal excitations. The binding energy of the final-state molecular ion ^{3}HeT$^+$ is 1.897 eV [3], and, since this is greater than the available excitation energy, the ^{3}HeT$^+$ must remain bound in this classical picture with no thermal motion. Then the final state consists

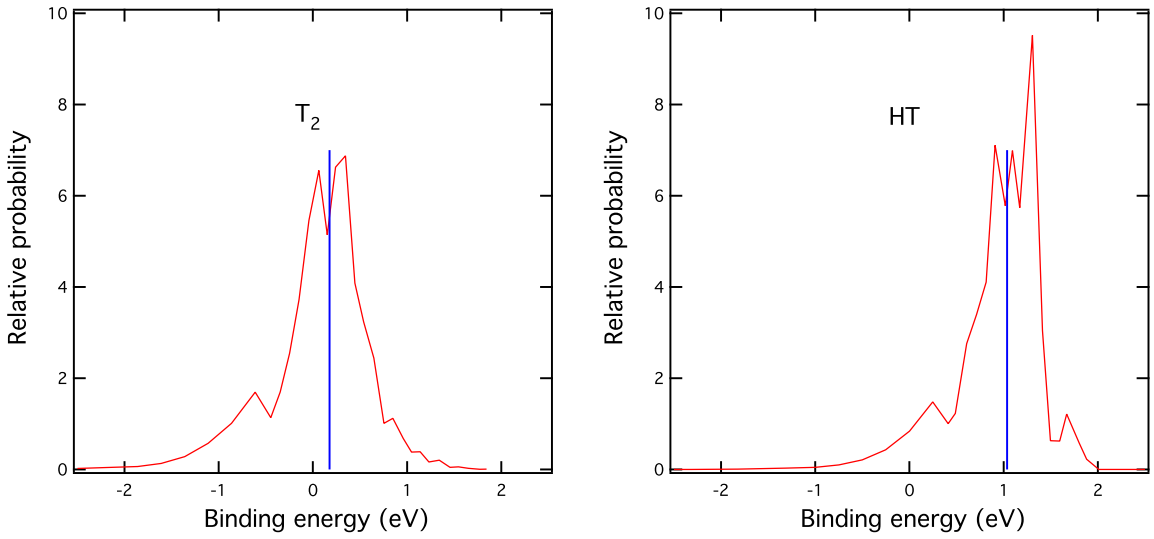

Figure 2.5: Distributions of excitation energy in the ground-state rotational and vibrational manifold of $^3HeT^+$ (left) and $^3HeH^+$ (right) as calculated by Saenz *et al.* [1]. The expected value for the excitation energy in each case, based on kinematic considerations, is indicated by a vertical line. An excitation energy of 0 corresponds to a binding energy of 1.897 eV [3]. (Figure made by R. G. H. Robertson for reference [4].)

of a mass-6 ion with a translational kinetic energy of 1.705 eV and rotational and vibrational excitations totaling 1.705 eV. How the excitation energy is apportioned between rotational and vibrational excitations depends (classically) on the relative orientation of the axis connecting the atoms to the lepton momentum direction, but the total excitation energy is always 1.705 eV.

The equivalent relationship for the HT parent molecule is

$$2.557 \quad \leq \quad E_{\rm rec}^{\rm kin} \leq 3.410 \text{ eV}, \tag{2.22}$$

the total internal excitation of the $^3HeH^+$ is 0.85 eV, and the translational kinetic energy is 2.557 eV. We compare these expectations with the calculations of Saenz, Jonsell, and Froelich [1] in Fig. 2.5.

The centroids of the theoretical distributions agree with our expectation but the distributions are not delta functions. Broadening is caused by the fact that atoms in the *parent* molecule are always in motion due to thermal and quantum effects, which smears the final-state momentum of the ^{3}He and the momentum of the outgoing leptons. The calculations of Saenz *et al.* were carried out in the center of mass for T_2 and HT gas at 30 K; we shall show that, at low temperatures, the chief mechanism for broadening is zero-point motion in the parent molecule.

2.3.2 Spectrum of the electronic ground state

A diatomic molecule at low excitation may be described as a one-dimensional harmonic oscillator:

$$E_v = (v+1/2)\hbar\omega_c + a(v\hbar\omega_c)^2;\ v = 0, 1, 2, ... \tag{2.23}$$

$$\omega_c = \sqrt{\frac{k}{\mu}} \tag{2.24}$$

where k is the force constant for displacements from the equilibrium internuclear separation, and μ is the reduced mass. A small anharmonic term with coefficient a is included. By fitting the four lowest vibrational states of the H_2 molecule [112] one finds $\hbar\omega_c = 0.5320(5)$ eV and $a = -0.0537(8)$ eV^{-1}. The corresponding value of $\hbar\omega_c$ for T_2 is then 0.3075 eV, much larger than k_BT at 30 K (0.003 eV), and also larger than typical rotational excitations (0.005 eV). In the vibrational ground state, the zero-point motion has an equivalent temperature of about 0.15 eV, or $\sim$ 1600 K, and dominates the line broadening. The zero-point energy is

$$E_{\rm zp} \equiv E_0 - E_{-1/2} = \frac{1}{2}\hbar\omega_c - a\left(\frac{1}{2}\hbar\omega_c\right)^2. \tag{2.25}$$

When beta decay occurs, the lepton recoil momentum $\mathbf{p}$ adds vectorially to the instantaneous momentum $\mathbf{p_T}$ of the decaying tritium nucleus of mass m within its molecule:

$$\mathbf{p_f} = \mathbf{p} + \mathbf{p_T}. \tag{2.26}$$

The mean kinetic energy of the decaying tritium nucleus is

$$\frac{\langle p_T^2 \rangle}{2\mu} = \frac{1}{2} E_{\rm zp}, \tag{2.27}$$

$$\mu = \frac{m_s m}{m_s + m}, \tag{2.28}$$

and the standard deviation of the excitation energy $E_{\rm exc}$ of the recoil ion is then

$$\sigma(E_{\rm exc}) = \frac{p}{m} \sqrt{\frac{1}{3} \langle p_T^2 \rangle} \tag{2.29}$$

$$= \sqrt{\frac{p^2}{2m} \left(\frac{2\mu}{3m} E_{\rm zp} \right)}. \tag{2.30}$$

where m is the mass of the decaying tritium nucleus, and m_s is the nuclear mass of the 'spectator' nucleus in the molecule. For the present purposes we ignore the difference between the nuclear masses of T and ^{3}He.

Inserting for $E_{\rm zp}$ the relevant zero-point energies for T_2 and HT, the predicted distributions of recoil excitation energy are compared with the calculated spectra of Saenz *et al.* [1] in Fig. 2.6. The good agreement (4%; see Table 2.3) underscores the fact that the gross features of the final-state distribution really arise from the *initial* state, *i.e.* it is mainly the zero-point motion of the tritium atom in its molecule that broadens what would otherwise be a line feature. The broadening occurs even for the ground-state molecule at absolute zero and is *irreducible*. Final-state effects assert their presence only through the density of available states in the $^3HeT^+$ and $^3HeH^+$ ions, which modulates the continuous distribution. That modulation may be calculated by evaluating the overlap integral between the final-state wave functions and the momentum projection operator acting on the initial state as given above.

Including the smearing effect of zero-point motion, the line feature is broadened to a sufficient extent that a large fraction of the distribution lies above the dissociation threshold, 1.897 eV in $^3HeT^+$. Jonsell *et al.* [90] find that while the intensity of the ground state transitions near the T_2 beta endpoint amounts to 57% of decays, 18% absolute lies above the dissociation threshold. For HT only 1.5% absolute is above

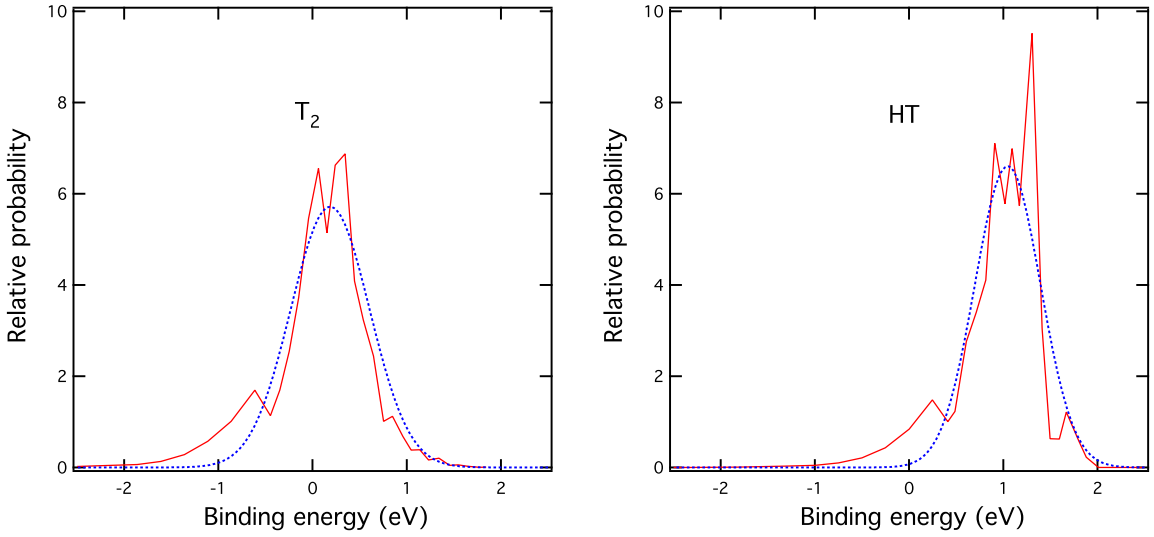

Figure 2.6: Calculated recoil excitation energy spectra from zero-point motion in the parent molecule (dotted curves, blue online), compared to the final-state distributions calculated by Saenz *et al.* [1] at 30 K (solid curves, red online). The curves from zero-point motion are parameter-free except for normalization, and have the standard deviations indicated in Table 2.3. An excitation energy of 0 corresponds to a binding energy of 1.897 eV. (Figure made by R. G. H. Robertson for reference [4].)

Table 2.3: Root-mean-square widths in eV of the ground-state manifold from the exact calculation of Saenz *et al.* [1] for initial state $J = 0$, and derived from the semiclassical treatment based on the zero-point motion of the parent molecule.

Method	T_2	HT
Saenz *et al.* [1]	0.436	0.379
Zero-point motion	0.420	0.354

the dissociation threshold (see Fig. 2.6). Not all such excited states will necessarily dissociate, however, because of the angular momentum barrier for states with high J.

Those states may be sufficiently long-lived to decay radiatively.

The T_2 vibrational energy interval of 0.308 eV is almost two orders of magnitude larger than the excitation energy $E_{J=1} = 0.00497$ eV of the lowest-lying ortho state (Sec. 2.2.4); the zero-point motion is thus the dominant contribution to the final-state width. If the parent molecule is in an initial state with angular momentum J, the root-mean-square width becomes

$$\sigma(E_{\rm exc}) = \sqrt{\frac{p^2}{2m}\left(\frac{2\mu}{3m}E_{\rm zp} + \frac{2\alpha^2 m_e^2 J(J+1)}{3R_0^2 m}\right)}, \tag{2.31}$$

where α is the fine structure constant and R_0 is the equilibrium internuclear separation in a.u. (1 a.u. $= \hbar/m_e\alpha$). The variances of the excited-state distributions for T_2, DT, and HT for states up to $J = 10$ are given in Table 2.4, and a graphical comparison with the calculations of Doss [3] up to $J = 3$ is displayed in Sec. 6.2.

The objective in a tritium beta-decay experiment is measurement of the neutrino mass via a detailed study of the shape of the electron spectrum near the endpoint. Energy conservation assures a connection between the molecular final state and the electron energy. The modification can be directly derived and has a particularly appealing and simple form.

If the tritium atom has a velocity β_T in the center of mass at the instant the decay takes place, the foregoing considerations of zero-point motion in the molecule give

$$\begin{aligned} \langle\beta_T^2\rangle &= \frac{E_{\rm zp}}{3m}\frac{m_s}{m_s+m} \\ \sigma(E_e) &= E_e\beta\sqrt{\langle\beta_T^2\rangle}. \end{aligned} \tag{2.32}$$

This result is identical to Eq. 2.30, the previously derived width for the excitation of the recoil.

2.3.3 Recoil energy spectra in dissociation

The theory of molecular beta decay can also be used to predict the energy of the ions produced in the decay. A measurement of the ion energy spectra would be helpful

Table 2.4: Root-mean-square widths in eV of the ground-state manifold of the daughter molecule from the semiclassical treatment based on the zero-point motion of the parent molecule with the inclusion of rotation.

(v, J)	T_2	DT	HT
(0,0)	0.4197	0.3972	0.3537
(0,1)	0.4331	0.4113	0.3694
(0,2)	0.4586	0.4381	0.3991
(0,3)	0.4944	0.4755	0.4398
(0,4)	0.5385	0.5212	0.4888
(0,5)	0.5890	0.5732	0.5439
(0,6)	0.6443	0.6299	0.6034
(0,7)	0.7035	0.6903	0.6662
(0,8)	0.7654	0.7533	0.7313
(0,9)	0.8297	0.8185	0.7983
(0,10)	0.8956	0.8853	0.8667

in assessing our understanding of the underlying decay. As Sec. 2.4.2 discusses in detail, theory predicts that approximately half of the decays of T_2 and HT lead to dissociative states [90], whereas experimental data indicate that more than 90% of the transitions lead to bound molecular ions [113, 114]. While there are several plausible experimental and theoretical explanations for this discrepancy, the disagreement motivates an examination of the dissociation-fragment spectrum that would be predicted by theory. The upcoming Tritium Recoil-Ion Mass Spectrometer experiment described in chapter 3 should able to make a measurement of this spectrum, providing a new test of the theory.

We examine the six dominant electronic configurations in the Born-Oppenheimer approximation as given by Jonsell *et al.* [90]. These configurations account for 84%

of the intensity, with the remaining 16% coming from the electronic continuum. In the ground-state manifold there is a potential minimum that leads to binding of the $^3HeT^+$ by almost 2 eV; all electronic excited states are monotonically repulsive with the exception of the first excited state, which has a shallow minimum far outside the Franck-Condon region. Rotational and vibrational states in the electronic-ground-state manifold are quasibound because of the potential minimum augmented by an angular momentum barrier as shown in Fig. 2.7. For this analysis we consider these quasibound states to be rotational and vibrational states of a bound (mass-6) ion which dissociates by tunneling through the barrier, analogous to fission. Conversely, owing to the absence of a binding potential, molecular motion in the electronic excited states corresponds more closely to the unbound scenario in which all the lepton momentum is delivered to a mass-3 recoil ion. In this case the two fragments gain additional kinetic energy at dissociation by converting the repulsive potential energy of the excited molecular state at the Franck-Condon spatial separation. The necessary data for the latter calculation can be found in Fig. 1 of Ref. [90].

The laboratory energies of the dissociation fragments from the quasibound ion can be calculated from kinematics. The laboratory kinetic energy $E_{i(\mathrm{lab})}$ for a fragment of mass m_i is uniformly distributed in the interval

$$E_{i(\mathrm{lab})} = \frac{1}{m_i + m_j}\left\{ \left(\sqrt{m_i E_{\mathrm{rec}}^{\mathrm{kin}}} - \sqrt{m_j(E_{\mathrm{exc}} - E_B)}\right)^2, \left(\sqrt{m_i E_{\mathrm{rec}}^{\mathrm{kin}}} + \sqrt{m_j(E_{\mathrm{exc}} - E_B)}\right)^2 \right\}, \tag{2.33}$$

for $E_{\mathrm{exc}} \geq E_B$ and $m_i E_{\mathrm{rec}}^{\mathrm{kin}} \geq m_j(E_{\mathrm{exc}} - E_B)$, where m_j is the mass of the other fragment and E_B is the binding energy of the molecular ion. It may be seen from this that the dissociation fragments from the quasibound states do not have translational energies significantly greater than that of the mass-6 ion, $E_{\mathrm{rec}}^{\mathrm{kin}}$.

Decays populating the electronic excited states produce recoil fragments, at least one of which is itself in an electronic excited state. Applying the Franck-Condon principle, the electronic excitation energy of the system before dissociation is evaluated

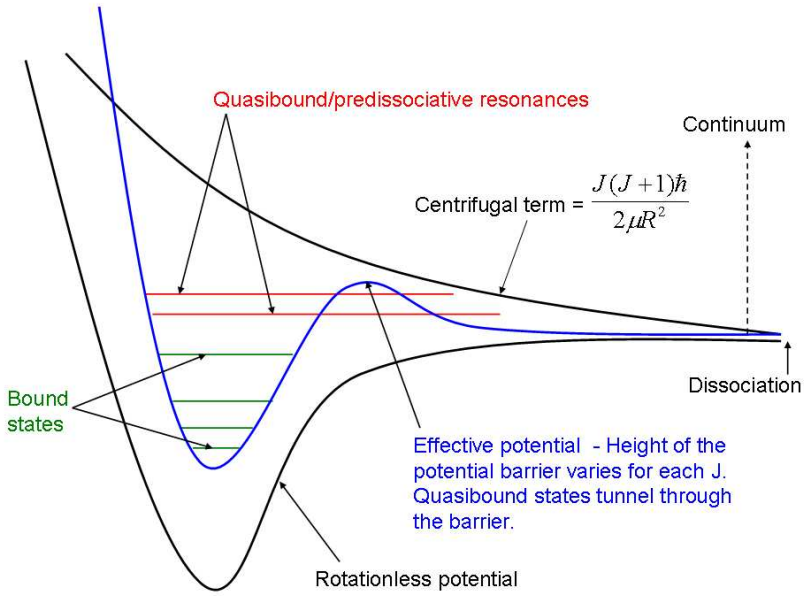

Figure 2.7: Sketch of potential curve for $^3HeT^+$ showing the bound, quasibound, predissociative resonance and dissociative states. Figure from the PhD thesis of N. Doss [3].

at the internuclear separation of the T_2, HT, or DT molecule in its ground state, 1.40 a.u. for all three species [9]. Tables 2.5 and 2.6 list the relevant properties for the six dominant electronic states and the kinetic energies of the recoil fragments.

The *total* kinetic energy available to the dissociation fragments by conversion of the interatomic potential in the five excited states is confined to a rather small range between 10 and 17 eV. An additional amount of kinetic energy $E'_{(\mathrm{trans})} = p^2/2m$ is contributed to the recoil of the beta-decay daughter by the lepton momentum. We therefore define and use in the Tables a parameter $0 \leq \eta \leq 1$ that is the fraction of the maximum lepton momentum squared. The other nucleus is a spectator and receives only the kinetic energy obtained from conversion of potential energy. The maximum energy imparted to a mass-3 daughter recoil is then about 12 eV for T_2 and 7 for HT. The He lines will be broadened by the zero-point motion as described in Sec. 2.3.2, and all lines will be broadened by the steep gradient of the interatomic potential in the Franck-Condon region. Moreover, except very near the endpoint, in an experiment the total lepton recoil momentum is not directly measurable; only the electron momentum is. This introduces a range of values of η at each energy, as may be seen in Fig. 2.4 and Eq. 2.19. A detailed calculation of the line widths is beyond the scope of this work.

The combination of the branching ratio to the bound molecular ion and the ion energy spectra provides a complete picture of the decay process. Measuring the branching ratio and kinematics has the potential to improve our understanding of the efficacy of our current model of molecular beta decay.

2.4 Tests of tritium final-state calculations

The sub-eV energy scales of the rotational and vibrational excitations and the unknown time scales for further evolution of the final-state products make direct measurement of the final-state distribution, and particularly those aspects that are reflected in the corresponding lepton momentum, all but infeasible. Of particular con-

Table 2.5: Structure of excited states and kinetic energies of dissociation fragments for the decay of T_2. The probabilities, which are valid in the sudden approximation, are taken from [9] for the case $J_i = 0$, and are very similar for $J_i = 1, 2, 3$. The total probability calculated for these six states is 84.2%.

State	Asymptotic structure	Excitation Energy (eV) $R = \infty$	Excitation Energy (eV) $R = 1.40$ a.u.	Total Kinetic Energy (eV)	E(^{3}He) eV	E(T) eV	Branch (%)
1	^{3}He($1s^2$) + T^+	< 0	< 1.897	–	–	–	39.0
	^{3}He($1s^2$) + T^+	> 0	> 1.897	Eq. 2.33			18.4
2	^{3}He$^+$(1s) + T(1s)	10.981	24.587	13.606	$6.8 + 3.4\eta$	6.8	17.4
3	^{3}He(1s2s) + T^+	20.5	31.390	10.890	$5.4 + 3.4\eta$	5.4	7.8
4	^{3}He$^+$(1s) + T(2s+2p)	21.186	36.152	14.966	$7.5 + 3.4\eta$	7.5	0.8
5	^{3}He$^+$(1s) + T(2s-2p)	21.186	36.833	15.647	$7.8 + 3.4\eta$	7.8	0.01
6	^{3}He(1s2p) + T^+	21.0	37.513	16.513	$8.3 + 3.4\eta$	8.3	0.9

Table 2.6: As Table 2.5, for the decay of HT. The total probability calculated for these six states is 83.8%.

State	Asymptotic structure	Excitation Energy (eV) $R = \infty$	Excitation Energy (eV) $R = 1.40$ a.u.	Total Kinetic Energy (eV)	E(^{3}He) eV	E(H) eV	Branch (%)
1	^{3}He($1s^2$) + H^+	< 0	< 1.897	–	–	–	55.4
	^{3}He($1s^2$) + H^+	> 0	> 1.897	Eq. 2.33			1.5
2	$^3He^+$(1s) + H(1s)	10.981	24.587	13.606	$3.4 + 3.4\eta$	10.2	17.4
3	^{3}He(1s2s) + H^+	20.5	31.390	10.890	$2.7 + 3.4\eta$	8.2	7.8
4	$^3He^+$(1s) + H(2s+2p)	21.186	36.152	14.966	$3.7 + 3.4\eta$	11.2	0.8
5	$^3He^+$(1s) + H(2s-2p)	21.186	36.833	15.647	$3.9 + 3.4\eta$	11.7	0.01
6	^{3}He(1s2p) + H^+	21.0	37.513	16.513	$4.1 + 3.4\eta$	12.4	0.9

cern are detector energy resolution and translational Doppler broadening of the distribution in a real experiment. The difficulty of a direct measurement has led to a variety of stratagems for indirect verification of the theory. In this section we discuss available data from spectroscopy, photodissociation, tritium-based neutrino mass measurements, and mass spectrometry.

2.4.1 Studies of the HeH^+ molecule

Rotational and vibrational level transitions

Determining the distribution of $^3HeT^+$ final states populated by beta decay requires calculating the energy levels of T_2 and of $^3HeT^+$. If the same theoretical framework is also applied to calculating the spectra of molecules with other isotopes of He and H, predicted transition energies can be compared against a large number of transition lines measured with high-precision spectroscopic techniques ranging from glow discharge to absorption spectroscopy to Raman spectroscopy. Such a comparison, of course, cannot test the probability of populating each $^3HeT^+$ state after beta decay, but as we saw in Sec. 2.2.1 it has provided valuable input to modern theoretical calculations.

Doss [3] calculated transition energies between rotational and vibrational levels in the electronic ground state for three tritium-containing parent molecules and for two daughter molecular ions and compared them to published spectroscopic data. For 21 measured transitions in T_2 [115], seven in DT [115], and 12 in HT [115, 116], ranging between 120 and 3775 cm^{-1}, the theoretical values always agreed within 1 cm^{-1} with a maximum fractional deviation of 0.1%. For 16 transitions in $^3HeH^+$ and 10 in $^3HeD^+$ [117, 118, 119], ranging from 71 to 3317 cm^{-1}, the agreement is still better, within 0.05%. However, there do exist experimentally measured transition energies for which no geminal-basis predictions are reported: two rotational-vibrational Q_1 transitions in T_2 [120] and two in DT [121], three purely rotational transitions in the

vibrational ground state of HT [121], and 12 transitions in hot vibrational bands of HT [116] that fall well outside the energy range of the other measured transitions.

In an earlier calculation in the standard geminal basis, Jonsell *et al.* [90] predicted transition energies ranging from 598 to 3157 cm^{-1} in helium hydride molecular ions containing the more common isotope ^{4}He, allowing validation against a much broader catalog of spectroscopically measured transitions. Five observed transition energies in $^4HeD^+$ [117] and sixty-two in $^4HeH^+$ [122, 123, 124, 125, 126] agree with these predictions to within 0.04%. The measured widths of seventeen predissociative resonances in $^4HeH^+$, $^3HeH^+$, $^4HeD^+$, and $^3HeD^+$ [117, 126] differ from the predicted values by up to an order of magnitude, but the specific machinery for calculating these widths is not used to determine the final-state distribution for neutrino-mass measurements [90]. No predictions are reported in the geminal basis for 46 additional observed transitions in low-lying vibrational bands of $^4HeD^+$ [118, 119, 127, 128], or for 36 similar transitions in $^4HeH^+$ [118, 119, 127, 129, 130].

Despite this great investment of experimental effort, only partial, fragmentary spectra have been measured for these seven molecules. Nonetheless, Coxon and Hajigeorgiu [94] were able to use these data to construct a fitted Born-Oppenheimer potential for the generic molecular helium hydride ion HeH^+, and compare it to an *ab initio* potential obtained from an older geminal basis with adiabatic corrections from Bishop and Cheung [131]. The two potentials differ by up to 2 cm^{-1} when the nuclei are close together but are in excellent agreement for internuclear distances $R \gtrsim 8$ a.u.; the dissociation energies differ by only 0.27 cm^{-1} [94]. No such comparison has yet been performed for the *ab initio* potential based on the most recent geminal basis.

While theoretical predictions for all measured transition energies would be useful, the excellent agreement obtained over 133 transition energies in seven diatomic molecules suggests that the rotational and vibrational energy levels of the electronic ground states are well reproduced in the geminal basis.

Photodissociation of $^4HeH^+$

The photodissociation spectrum of $^4HeH^+$ may be derived from a sufficiently complete theoretical description of the molecule. Since all electronic excited states of this molecule are dissociative in the Franck-Condon region, one can construct the photodissociation cross section as a function of energy by calculating dipole transitions between the electronic ground state and the electronic excited states. The result depends on the orientation of the internuclear axis relative to the photon polarization vector; the parallel and perpendicular cases must be treated separately. Several other theoretical models (*e.g.* [132, 133]) have been employed to study the photodissociation problem, but have not been applied to neutrino-mass measurements. Photodissociation calculations have been made with both the geminal and CI techniques.

The process has been probed experimentally with 38.7-eV (32-nm) photons at the Free-electron LASer in Hamburg (FLASH). The initial measurement [134] determined the cross section to the $^4He + H^+$ channel, and was not able to define the initial distribution of vibrational states in $^4HeH^+$. The second FLASH measurement [135] incorporated several experimental upgrades to provide additional tests. The $^4HeH^+$ beam could optionally be routed through a linear electrostatic ion trap and cooled to the $\nu = 0$ vibrational ground state before being extracted to the interaction region. An improved detection setup, combined with a positive potential across the ion-photon interaction region, allowed the measurement of the branching ratio to the $^4He + H^+$ and $^4He^+ + H$ channels. In both experiments, the distribution of the initial internuclear axis orientations was assumed to be isotropic.

Beginning with the same geminal basis set as that used for standard neutrino-mass-relevant calculations, Saenz computed the total photoabsorption cross section assuming that the molecule begins with $\nu = 0$ and is oriented parallel to the photon field [102]. Dumitriu and Saenz later performed a more detailed calculation in the CI method [136] and were able to reproduce those results; despite a 3% discrepancy in the

location of the first resonance, near 25 eV, the two methods are in close agreement at the 38.7-eV energy of the FLASH measurements. CI calculations were also performed for the individual dissociation channels, and for an isotropic molecular orientation, allowing direct comparison with the FLASH cross-section measurement [134]. The CI calculations give a ratio of ~ 1.7 between the two dissociation channels at energies above 35 eV [136], so that the total photoabsorption cross section of $\sim 0.8 \times 10^{-18}$ cm^2 at 38.7 eV, predicted in the geminal model [102], implies a partial cross section of $\sim 0.3 \times 10^{-18}$ cm^2 to the ^{4}He + H$^+$ channel. The cross-section results, shown in Table 2.7, demonstrate consistency between experiment and theory, although no theoretical uncertainties have been assigned and the experimental uncertainty is large.

Table 2.7: Photodissociation cross section for $^4HeH^+ + \gamma \rightarrow {}^4He + H^+$, from geminal and CI theories as well as from an experiment at FLASH. The geminal result, originally computed for both dissociation channels, is corrected for this channel by a factor of 1.7, given by CI calculations.

	Molecular Orientation	Cross-section (10^{-18}cm^2)
Geminal [102] (with CI [136])	Parallel	~ 0.3
CI (adiabatic limit) [136]	Parallel	~ 0.46
FLASH [134]	Parallel	0.4(2)
CI (adiabatic limit) [136]	Isotropic	1.4
FLASH [134]	Isotropic	1.45(7)

For each event in the FLASH data, the neutral-fragment momentum can be used to reconstruct the initial molecular orientation, under the assumption of fast fragmentation. In general, $\Sigma - \Sigma$ transitions peak for orientations parallel to the field, while $\Sigma - \Pi$ transitions peak when the molecule is oriented perpendicular to the field.

For vibrationally cold molecular ions dissociating through the $^4He + H^+$ channel, the measured value of $\sim 1:3$ for the $\Sigma:\Pi$ contribution ratio [135] agrees reasonably well with the CI prediction of $\sim 1:2$ [136]. There is a clear disagreement in the other channel, however: an experimental measurement of $\Sigma:\Pi \sim 1:1$, compared to a CI prediction of $\sim 1:6$.

Another discrepancy arises in the relative probability of photodissociation to the two channels. For vibrationally cold molecular ions, a ratio of $\sigma_{He^+ + H}/\sigma_{He + H^+} = 1.70(48)$ was observed in the later FLASH measurement [135], in agreement with the prediction of about 1.7 from the CI method [136]. However, this ratio was found to drop to 0.96(11) when the ion beam was not cooled, contradicting the expectation from the CI potential curves that the ratio would rise.

Without an error estimation from the theory, the significance of these discrepancies between the CI model and experiment cannot be evaluated. If the discrepancies hold, they may signal the importance of non-adiabatic effects, which were not included in the calculation of the CI potential curves [136]. Such effects are expected to be important to the application of the CI method to the molecular final-state distribution following beta decay in T_2.

2.4.2 Studies of $^3HeT^+$ and $^3HeH^+$ after beta decay

Instantaneous final-state distribution after beta decay

In principle, spectroscopy of T_2 gas can be used to measure the instantaneous population of accessible $^3HeT^+$ final states after T_2 beta decay, provided that primary radiative transitions from states excited in beta decay are distinguished from secondary transitions from states excited collisionally. One expects that electronic excitations of $^3HeT^+$ will dissociate on a time scale of about 10^{-15} s, so any observable radiative transitions must arise from excited dissociation products. Consideration of the dissociation channels for each electronic excited $^3HeT^+$ state led Jonsell *et al.* to con-

clude that only states representing about 16% of the total transition probability can result in electronic excited dissociation products that decay via photon emission [90]. A calculation of the full probability distribution of dissociation channels and excitation states is complicated by interference between molecular states and has not been attempted. Experimental data on these transitions are sparse: only one primary transition has been observed in T_2 spectroscopy, a 468.6-nm line corresponding to the $4s \rightarrow 3p$ transition in $^3He^+$ [137, 138].

As seen in Sec. 2.4.1, radiative transitions also occur between rotational and vibrational levels of $^3HeT^+$. An infrared emission line at 4.69(3) μm has been observed in T_2 gas and identified as the transition between the $v = 1$ and $v = 0$ vibrational levels of the $^3HeT^+$ electronic ground state [139]. The population of excited rotational and vibrational states after T_2 beta decay depends on the beta momentum and the calculations are done in the context of endpoint measurements. This experiment did not detect the beta electrons and was therefore insensitive to the variation with beta momentum. The measured excitation probability of the $v = 1$ level, 0.4(2) [139], thus cannot be compared directly to predictions made near the beta endpoint [90].

Branching ratios to electronic excited final states

The theory can also be probed by measurements of the branching ratios to various regions of the final-state spectrum following beta decay in T_2. A precise measurement of the electron energy spectrum about 25 eV below the endpoint would give the branching ratio to the electronic excited states of $^3HeT^+$, which cause a kink in the tritium beta decay spectrum. With good energy resolution and a large enough sample window, the change in slope can be measured. The energy resolution must be better than 10 eV to resolve the kink, and the spectrum must be extended to still lower energies to accurately measure the initial slope. Lower energies correspond to much higher rates, imposing a significant burden on the detector system. In addition corrections for scattering introduce systematic uncertainty.

Theory predicts that this branching ratio should be about 43% near the endpoint [90], but no measurement of the branching ratio to electronic excited states has been reported. The KATRIN experiment will be able to measure the spectrum in the relevant regime, providing the first direct test of the branching ratio to electronic excited states.

First and second moments of FSD from beta decay

It was pointed out by Staggs *et al.* [140] that one of the most direct measures of the accuracy of the FSD is the comparison of the extrapolated endpoint from beta decay with the value expected from mass-spectrometric determinations of the T-^{3}He atomic mass difference, Q_A. If the extrapolated endpoint is obtained from the beta spectrum well below the endpoint, it is the average of the individual quantities Δ_{kj} and differs from the ground-state value Δ_{00} by the first moment of the FSD. Neglecting neutrino mass and the Heaviside function, which affect the spectrum only at the endpoint, the beta spectrum of Eq. 2.13 summed over final states k becomes

$$\frac{dN}{dE_e} \simeq CF(Z,E_e)\frac{p_e E_e}{\epsilon_0^2}\left(1-\frac{E_e}{M_0}\right)\sum_k |W_{k0}|^2\,(\Delta_{k0}-E_e)^2. \tag{2.34}$$

The summation may be written in terms of binding energies and the atomic mass difference,

$$\sum_k |W_{k0}|^2\left[(Q_A-b_0+2m_e)\left(1-\frac{Q_A-b_0}{2M_0}\right)-m_e+b_{(f)k}-E_e\right]^2 \tag{2.35}$$

$$\equiv \sum_k |W_{k0}|^2\left(\delta+b_{(f)k}-E_e\right)^2 \tag{2.36}$$

where terms of order $b_{(f)k}m_e/M_0$ have been dropped and a parameter δ (the extrapolated endpoint energy for zero final-state binding) has been defined for brevity. The summation may then be carried out,

$$\frac{dN}{dE_e} \simeq CF(Z,E_e)\frac{p_e E_e}{\epsilon_0^2}\left(1-\frac{E_e}{M_0}\right)\left(\delta+\langle b_{(f)k}\rangle-E_e\right)^2 \times\left(1+\frac{\sigma_b^2}{\left(\delta+\langle b_{(f)k}\rangle-E_e\right)^2}\right) \tag{2.37}$$

The mean binding energy $\langle b_{(f)k} \rangle$ acts as a shift in the extrapolated endpoint δ, and the variance $\sigma_b^2 = \langle b_{(f)k}^2 \rangle - \langle b_{(f)k} \rangle^2$ of the (full) binding-energy distribution enters the expression as a shape distortion near the endpoint. Hence, both the first and second moments of the final-state distribution can be extracted from data for comparison with theory. Table 2.8 lists the first three moments of the binding-energy distributions for two theories.

In practice, experiments are not analyzed in this way. Rather, the FSD from theory is used to generate the spectrum to be fitted to data, from which values for Q_A and m_ν can be extracted. In addition, only three experiments have used gaseous tritium, and the most modern of these (Troitsk [56]) has a scattering contribution to the spectrum at energies more than 10 eV below the endpoint. However, the two remaining experiments, LANL [48] and LLNL [50] used differential spectrometers and magnetic field configurations designed for a broad spectral reach. The two experiments were in good agreement with each other, but, as is well known, both found an unexpected excess of events in the endpoint region, which is expressed numerically as a negative m_ν^2. They also yielded concordant values for Q_A, but only recently has an accurate determination of Q_A by a non-beta-decay method, ion cyclotron resonance in the Smiletrap apparatus [89], become available for comparison. Table 2.9 shows the results of the LANL and LLNL experiments as originally reported, both having been analyzed with the theory of Fackler *et al.* [2].

It is possible to estimate the changes that would be produced with the use of a more modern theory such as that of Saenz *et al.* [1] by applying Eqs. 2.37 and 6.1. The results are shown in the lower half of the table. There is excellent agreement between the atomic mass from beta decay and from ion cyclotron resonance, 18589.8(12) eV, and the large negative value of m_ν^2 is eliminated in both experiments, subject to the limitations of the approximations used. These results provide a striking measure of experimental confirmation of the calculations of Saenz *et al.*, especially in the difficult regime of electronic excited states.

Table 2.8: Comparison of zeroth, first, and second moments of theoretical final-state distributions [10].

Reference	Excitation energy range	$\sum_k \lvert W_{k0}\rvert^2$	$\langle b_{(f)k}\rangle$	σ_b^2
	eV		eV	eV^2
Fackler *et al.* [2]	0 to 165	0.9949	-17.71	611.04
Saenz *et al.* [1]	0 to 240	0.9988	-18.41	694.50

Table 2.9: Atomic mass difference and neutrino mass squared extracted from two experiments, in one case with the original 1985 theoretical calculations of the FSD and in the second case with a more modern calculation.

	LANL [48]	LLNL [50]
As published. Theory: Fackler *et al.* [2]		
Δ_{00} (eV)	18570.5(20)	18568.5(20)
Q_A (eV)	18588.6(20)	18586.6(25)
m_ν^2 (eV^2)	-147(79)	-130(25)
Re-evaluated. Theory: Saenz *et al.* [1]		
Δ_{00} (eV)	18571.2(20)	18569.2(20)
Q_A (eV)	18589.3(20)	18587.3(25)
m_ν^2 (eV^2)	20(79)	37(25)

Branching ratios to molecular and atomic species

The branching ratio to the bound molecular ion can be extracted from the theory in a straightforward way with certain assumptions. Two 1950s mass-spectrometry experiments measured this branching ratio for HT [113, 114]; one of the experiments also measured the branching ratio for T_2 [114]. The experimental results are consistent with each other but disagree starkly with the theoretical prediction.

Calculations of the dissociation likelihood rely on the theoretical dissociation energy of 1.897 eV and assume that all electronic excited states are dissociative, *i.e.* there are no fast radiative transitions between the excited states and bound states [90]. Under these assumptions, and working near the beta endpoint, Jonsell *et al.* [90] have calculated a branching ratio to the bound $^3HeT^+$ molecular ion of $0.39 - 0.57$, depending on whether the quasibound states above the binding energy dissociate. An absolute uncertainty of 0.2%, derived from requiring that the FSD integrate to 100%,

is given for calculation of the entire spectrum but no explicit uncertainties are indicated for the branching ratios.

A calculation of the differential spectrum as a function of electron energy would permit a more stringent test of the theory than the energy-averaged branching ratio. Experimentally, the ability to distinguish between dissociation products (*e.g.* between $^3He^+ + T$ and $^3He + T^+$) allows a stronger test than a simple measurement of the dissociation likelihood, yielding information about how the electronic states are populated after beta decay.

The first experimental measurement of molecular dissociation following tritium decay was reported for HT by Snell, Pleasanton, and Leming in 1957 [113]. The experiment used a mass spectrometer with a conical assembly of ring electrodes that focused ions from an equilibrated mixture of HT, T_2, and H_2 gas into a magnetic analyzer followed by an electron multiplier [141]. The measured intensity of the mass-2 peak (H_2^+) was used to correct the other peaks for ionization of the T_2 or HT gas caused by collisions with beta electrons. The mass-3 peak (T^+ or $^3He^+$) was corrected for the presence of T_2 in the sample gas, based on the ratio of the mass-6 and mass-4 peaks. The correction assumes that HT and T_2 have identical dissociation probabilities, which theory does not exclude [90]. The final published result was a 93.2(19)% branching ratio for HT decay to the bound $^3HeH^+$ ion [113].

The following year, Wexler used a mass spectrometer with significantly different ion optics to measure the dissociation probability for both HT and for T_2 [114]. In this apparatus, the entire source volume was contained within a cone of ring electrodes, which was followed by two distinct deflection stages, one to exclude neutral molecules and one for analysis. A measurement with T_2 gas, after correction for an 11.5% HT impurity, yielded a 94.5(6)% probability of decay to the bound $^3HeT^+$. With a pure sample of HT (0.4% T_2 contamination), the probability of decay to the bound $^3HeH^+$ ion was measured at 89.5(11)%, in broad agreement (1.2σ) with the Snell *et al.* measurement [113].

In the T_2 dataset, the Wexler apparatus was unable to resolve the difference between $^3He^+ + T$ and $^3He + T^+$. For an HT source, however, both Wexler [114] and Snell *et al.* [113] found that dissociation into a final state of $^3He^+ + H$ was about three times more likely than dissociation into $^3He + H^+$. This is qualitatively similar to the prediction shown in Table 2.6, which yields a ratio of 2.1 for the five electronic excited states considered.

Table 2.10: Branching ratio to the bound molecular ion for HT and T_2.

Molecule	Theory	Snell *et al.*	Wexler
	(Ref. [90])	(Ref. [113])	(Ref. [114])
HT	0.55–0.57	0.932(19)	0.895(11)
T_2	0.39–0.57	–	0.945(6)

Table 2.10 summarizes theoretical and experimental results for the branching ratio to the bound molecular ion. The experimental results for HT and T_2 are in stark disagreement with the theoretical predictions. While a problem of this magnitude with the theory seems unlikely, it is true that geminal calculations of the bound and continuum states are not done in the same basis, and the normalization between the calculations can bias the branching ratio.

To reconcile theory and experiment, other explanations have been advanced for the discrepancy. The applicability of the theory can be questioned in that the experiments integrated over the entire beta spectrum whereas the sudden approximation is valid when the electron energy is much larger than atomic binding energies. Another possible mismatch between theory and experiment arises from the evolution of the final state before the ions are detected. If fast radiative transitions from the electronic excited states to the ground state exist, the experimental measurements would have been too slow to prevent repopulation of the ground state. At the same time, the measurements may have been too fast for some quasi-bound states in the ground-state

manifold to dissociate. The time scales for radiative decays are, however, expected to be orders of magnitude longer than those for dissociation of all but the quasibound states.

A number of potential issues have also been identified, including:

1. The acceptance depends on the transverse momentum distribution which differs between the ion species

2. The Sudden Approximation is only valid near the endpoint while the measurements integrate over the spectrum

3. Contamination of mass-6 signal by ionized T_2 may not have been accounted for properly

4. Repopulation of the ground state would be possible if fast radiative transitions between electronic excited states and the ground state of $^3HeT^+$ exist

5. Error in the calculations arising from the parameterization of the bound versus unbound states in the electronic ground state

1. The acceptance depends on the transverse momentum distribution which differs between the ion species

2. The Sudden Approximation is only valid near the endpoint while the measurements integrate over the spectrum

3. Contamination of mass-6 signal by ionized T_2 may not have been accounted for properly

4. Repopulation of the ground state would be possible if fast radiative transitions between electronic excited states and the ground state of $^3HeT^+$ exist

5. Error in the calculations arising from the parameterization of the bound versus unbound states in the electronic ground state

For example, the experiments may not have properly accounted for contamination of the mass-6 signal by T_2^+ produced via ionization, artificially inflating the measured branching ratio to the bound molecular ion. Many of these issues were known the to the experimenters who took steps to mitigate them.

Wexler himself proffers the explanation that the relative efficiencies between ion species were poorly understood, as the acceptance of both mass spectrometers depended strongly on the initial transverse energy of the ion [114, 90, 42]. This transverse energy is dependent on the ion species and can range up to tens of eV following dissociation of excited states of $^3HeT^+$, although most of the dissociation processes should lead to ions in the energy range 3 – 13 eV. As computed in Sec. 2.3.3, the ion energies resulting from excited-state dissociation are larger than the $\sim$ 1-eV energies for mass-3 fragments in the breakup of the ground state, but whether this accounts for the experimental results is not possible to determine without a model for the acceptance of the mass spectrometers. A more telling observation, however, is that in the decay of HT the energies of the mass-3 fragments are lower than in the decay of T_2. That is consistent with Wexler's suggestion because the measured branch to the bound final state HeH^+ is smaller than that to HeT^+, perhaps a result of better efficiency for detecting the dissociation fragments. One may also surmise that while dissociation is energetically allowed from the ground-state manifold above 1.897 eV excitation, it is strongly hindered by the angular momentum barrier. A much larger fraction of the HeT^+ ground-state manifold can potentially decay this way than for HeH^+, and yet the data show the opposite behavior.

The disagreement between theory and experiment has not been satisfactorily explained, although many sources of possible unquantified experimental error have been proposed. However, no data are available to test these explanations and further mea-

surements with the potential to resolve this tension are desirable.

2.4.3 Desiderata for a modern experiment

A modern dissociation experiment could more closely reproduce the conditions for which the calculations are performed. Detecting the ion in coincidence with a beta electron of measured energy would allow the experimenter to examine the specific regime where the sudden approximation is valid and to study the variation of the dissociation fraction with electron energy. The acceptance of the instrument for ions with a range of initial kinetic energies needs to be quantifiable. Measurement of the ion energy distribution would provide a stronger test of the model. Complementary information is also available in the coincident photon spectrum but the expected emission falls in the vacuum ultraviolet regime, making it difficult to instrument. Operating conditions must be such that charge exchange is a minor and quantifiable perturbation.

An apparatus comprising semiconductor detectors imaging low-pressure tritium in uniform, coaxial electrostatic and magnetic fields achieves many of these objectives. Mass separation is achieved by time of flight, and the field arrangement offers high efficiency. When the magnetic field strength is sufficient to collect ions regardless of their transverse momentum, the species-dependent efficiency changes can be eliminated. The radial excursions of the ions can, moreover, be mapped to provide information about their energies and to provide assurance that all have been detected. Higher detection efficiency allows the source pressure to be lowered, reducing charge exchange, which can artificially lower the measured dissociation probability. An experiment utilizing this approach could more closely reproduce the conditions of the calculations and provide a direct test of specific aspects relevant to the neutrino mass measurement. Such an experiment, the Tritium Recoil-Ion Mass Spectrometer (TRIMS), is described in chapter 3.

A modern experiment making use of semiconductor devices for ion identification

and using an axial magnetic field to guide ions can provide a measurement that is directly comparable to the calculations. Provided the magnetic field is strong enough to guide all dissociated ions to the detectors such a setup has a higher detection efficiency and lower species dependence than traditional mass spectrometers.

The use of high efficiency detectors also allows lower pressures in the source, thereby reducing the mass-6 contamination from charge exchange. The use of coincidence also lowers the mass-6 contamination from T_2 ionized via processes other than beta decay. Additionally the effect of the sudden approximation can be tested by directly by measuring the beta energy and extracting branching ratios for the sudden approximation regime and the low-energy regime.

The repopulation of the ground state would result in the emission of photons that could potentially be measured in coincidence with the decay. The photon regimes of interest are the vacuum-ultraviolet and far infrared, both difficult for single photon detection. The effects of deexcitation in-flight between the decay and the detector depend on the energy and lifetime of the states. The lifetimes are expected to be short compared to the flight time of the ions in TRIMS and the energies are low compared to recoil. Thus post-decay radiation should not affect the interpretation of the TRIMS data in terms of branching ratios.

To address some of the difficulties that arise in normalizing the calculations new, independent calculations are being performed by Alejandro Saenz and Christoph Roll at Humboldt-University in Berlin [103]. The calculations include a treatment of post-decay deexcitation as necessary for comparison with TRIMS data. The updated calculations are discussed in more detail in section 2.2.2

Chapter 3

TRITIUM RECOIL-ION MASS SPECTROMETER

Tritium Recoil-Ion Mass Spectrometer (TRIMS) is an experiment to measure the molecular-tritium beta-decay branching ratio to the bound ion. In this chapter we describe the design of the experiment. Having previously discussed the history of dissociation measurements (2.4.2) and desiderata for a new experiment (section 2.4.3) we describe the modern techniques that will be used to make measurements that are directly comparable to calculated branching ratios.

3.1 Experimental Concept

We designed the Tritium Recoil-Ion Mass Spectrometer (TRIMS) experiment to measure the molecular tritium beta decay branching ratio to the bound molecular ion $^3HeT^+$. The apparatus consists of a time-of-flight mass spectrometer with a silicon detector at each end: one for beta detection and one for ion detection. The spectrometer is filled with high-purity molecular tritium gas at a pressure of $\sim 10^{-7}$ mbar. A potential difference of ∼50 kV is maintained between the two detectors for accelerating the ions and betas above a ∼15-keV detection threshold. An axial magnetic field guides the charged particles to the detectors. Figure 3.1 shows a schematic of the apparatus and the direction of travel of the particles in a decay event.

Eqn. 3.1 shows the relationship between ion energy E_{ion}, the distance ΔD_{ion} that the ion travels to the detector, length L_{chamber} of the experimental chamber and voltage drop V_{chamber} across the chamber. Accelerating potentials of > 50 kV provide reasonable ion-detection efficiency in silicon and contribute the largest fraction of ion energy. The few eV initial energy of the ion is negligible and the ion energy and time

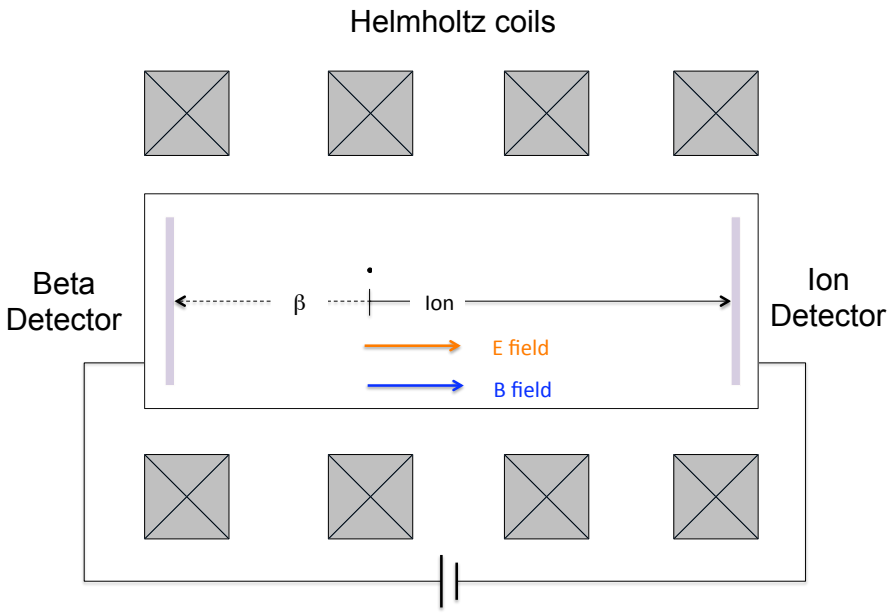

Figure 3.1: Schematic of the TRIMS detector with a sample decay. The solid line represents the direction of travel of the ion and the dashed line represents the direction of travel of the beta.

of flight are given by:

$$E_{\text{ion}} \sim \frac{qV_{\text{chamber}}\Delta D_{\text{ion}}}{L_{\text{chamber}}}, \tag{3.1}$$

$$t_{\text{ion}} \sim \sqrt{\frac{2mL_{\text{chamber}}\Delta D_{\text{ion}}}{qV_{\text{chamber}}}} \tag{3.2}$$

Section 3.4.2 provides more details on the derivation of the ion time of flight. From eqn. 3.2, the time of flight for the dissociated mass-3 ions ($^3He^+$, T^+) differs from the time of flight for bound mass-6 ions ($^3HeT^+$) by a factor of $\sqrt{2}$. The combination of energy and time of flight distinguishes between the mass states and can be used to extract the branching ratio to the bound molecular ion. The effect is clearly statistical and a signficant number of decays must be observed to provide adequate resolution to

deduce the fraction of decays that lead to the bound ion. The same equations applied to HT decay lead to mass-1 (H^+), mass-3 ($^3He^+$) and mass-4 ($^3HeH^+$) branches. The separation of the mass-1 branch provides plays an important role in the minimization of HT backgrounds in T_2 sources as discussed in sec. 3.3.

The mass-3 state actually consists of two branching ratios: one to $^3He^+$ and one to T^+. The relationship between nuclear charge and energy deposition may provide a way to differentiate the two ions, as a doubly charged helium nucleus loses more energy in the dead-layer (partially inactive entrance window) of the detector than a singly charged tritium nucleus of the same kinetic energy. Given very high energy resolution and an optimal dead-layer thickness the difference in energy deposition can distinguish T^+ from $^3He^+$. In such a setup the dead-layer acts analogously to dE/dx detectors in high-energy physics experiments. The technique is more effective at higher energies where the loss in the dead-layer is small compared to the total energy. Thus very high voltages would be required and further investigation is necessary to determine the possibility of separately measuring the T^+ and $^3He^+$ branching ratios. The first phase of the experiment does not distinguish between the two mass-3 species.

The new design has several advantages over the older dissociation measurements. The use of silicon detectors decreases the sensitivity to initial transverse momentum, thus lowering species-dependent differences in collection efficiency. Magnetic guiding increases the overall efficiency and, more importantly, reduces species dependence. The detection of the coincident primary beta allows determination of the branching ratio to the bound molecule as a function of beta energy, a more detailed test of theoretical calculations than the energy-averaged branching ratio that was previously measured.

Measurements of the branching ratio require an understanding of the lifetimes of the excited states of the daughter ion. De-excitation occuring between the decay and detection would skew the result. The Configuration Interaction calculations of Saenz and Roll will address the possibility of radiative decays [103], directly addresssing the

issue of de-excitation as a possible explanation for the defecit in measured dissociation rates. The new calculations will provide an apples to apples comparison with the TRIMS results as opposed to previous calculations and experiments which were not directly comparable.

3.2 Simulations

The original TRIMS experimental final-state simulation (FSSim) is a Monte Carlo (MC) description of radioactive decay within the volume of the chamber and the response of the apparatus to the decays. FSSim relies on the ROOT framework [142] and uses the same file structure as the TRIMS data files with the exception that simulation files contain MC truth information. Stopping and Range of Ions in Matter (SRIM) [143] output provides the ion energy deposition information for each ion species. For a given set of branching ratios and experimental parameters (e.g. high voltage) the simulation creates an energy-time-of-flight spectrum by generating decays and calculating the time of flight to the detector, energy deposited in the beta detector and energy deposited in the ion detector.

The nominal FSSim simulation uses the parameters of Table 3.1, randomizing the location of the decay within the apparatus and the initial direction of travel of the daughter ion. The initial beta energy is drawn from the standard spectrum (Fig. 2.1) and the initial ion energy is drawn from a set of initial spectra for each species. The intial state determines the time of flight and the energy of the ion at the entrance of the detector via eqn. 3.1-3.2. Using SRIM simulations we determine the energy deposition in the dead-layer and active layer of the detector. In following the findings of reference [144], we simulate the dead-layer as a partially-active region from which half of the charge is collected. In the energy range of interest, higher order effects such as plasma formation and the pulse-height defect are small, so we currently do not include them in the simulation. Both of these effects are percent level corrections, significantly smaller than the uncertainty on the energy loss in the dead-layer. We

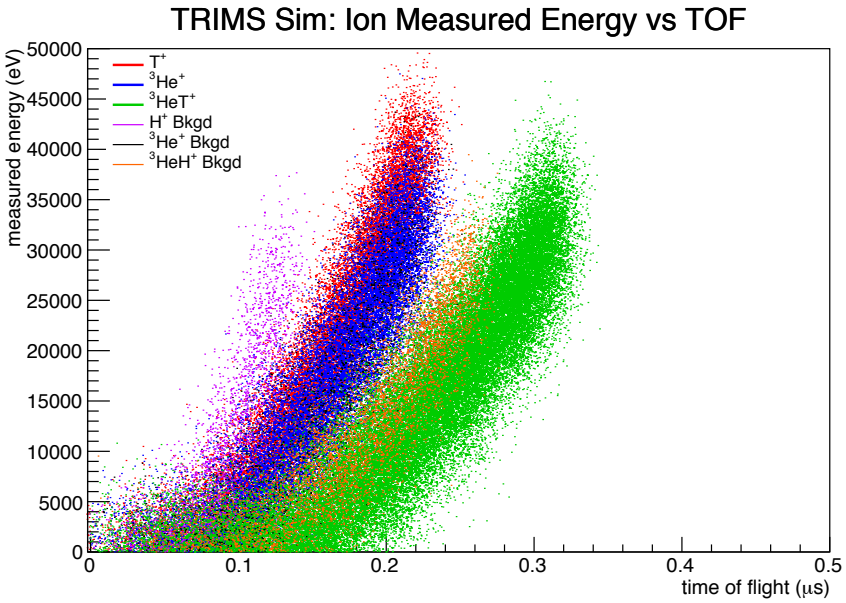

Figure 3.2: TRIMS Simulation showing the energy deposited in the active region of the ion detector versus time of flight for each ion species. This simulation used branching ratios of 0.57 to $^3HeT^+$, 0.22 to $^3He^+$ and 0.21 to T^+. The HT contamination is 10%.

convolve the results with Gaussian smearing with user-specified electronic and timing resolutions (nominally $\sigma_E = 3$ keV and $\sigma_t = 10$ ns) to provide realistic simulation of "measured" data, that is, spectra that closely approximate what would be seen in the experiment for a given set of parameters. ROOT trees store the simulation output for analysis. Post-processing of the simulation results provide reconstructed parameters for comparison with the MC truth values.

Figure 3.2 shows a simulated dataset consisting of 100,000 decays in a 20-cm chamber with a 50-kV electrode and a 100-nm dead-layer on the detector. The branching ratios used in this simulation are 0.57 for $^3HeT^+$, 0.22 for $^3He^+$and 0.21 for T^+. The simulation shows the clear time of flight separation for mass 3 and mass 6. Harder to

see is the energy separation of $^3He^+$ and T^+. Two-dimensional cuts (parabolas) are made to avoid species-dependence (i.e. to minimize differences in efficiencies)[1]. The curvature of each parabola is set by the voltage, length of the chamber and ion mass while the offset is related to the energy loss mechanisms.

The presence of HT contamination in the source leads to confusion between the mass states as it produces real mass-3 ions as well as mass-4 ions that can be mistaken for mass-3. The mass-1 ions, however, arewell separated and can be used to quantify and remove the mass-3 and mass-4 backgrounds.

The intermediate values of beta and ion energy are stored to provide checks on the implementation of the physics at each step of the simulation. Figure 3.3 shows the beta spectrum generated by FSSim with the familiar shape described in Chapter 2. Figure 3.4 shows the beta energy after acceleration through the electric potential. Figure 3.5 shows the ion energy generated in the decay. The initial energy spectrum of the ion is taken from table 2.5 and table 2.6. The low energy portion comes from the bound molecular ions while the structures around 10 eV arise from the excitation levels. The ion energy distribution is not treated exactly as the calculations are done within the sudden approximation. The contribution of the low-intensity tail (electronic continuum) is not included in the ion energy distribution as the asymptotic behavior is not well understood. Figure 3.6 shows the ion energy after acceleration through the field. Figure 3.7 shows the final simulation for the energy measured in the detector. The MC truth time of flight and the simulated measured time of flight are shown in Fig. 3.8 and Fig. 3.9, respectively.

Figure 3.10 shows the energy-versus-time-of-flight spectrum generated by the FSSim. The binned distribution shows a separation of the mass-3 and mass-6 branches as expected. The cuts shown are generated by fitting the energy-cut time-of-flight

[1]The two-dimensional approach is preferred over data manipulation as the latter causes the x-axis errors to vary with position along the axis. In the two-dimensional approach the x-axis (timing) errors are independent of the position and the plots have a clear interpretation.

Table 3.1: Parameters used in the simulations of the TRIMS apparatus shown in Fig. 3.3

parameter	**nominal simulation**	**high HT simulation**
Chamber length (m)	0.2	0.2
Chamber voltage (kV)	50	50
Pressure (mbar)	1E-7	1E-7
Magnetic Field (kG)	2	2
Fraction of HT	0.1	0.3
Timing resolution (ns)	10	10
Energy resolution (keV)	3	3
Dead layer (nm)	100	100
$\mathcal{B}(T_2 \rightarrow T^+ + {}^3He)$	0.21	0.21
$\mathcal{B}(T_2 \rightarrow {}^3He^+ + T)$	0.22	0.22
$\mathcal{B}(T_2 \rightarrow {}^3HeT^+)$	0.57	0.57
$\mathcal{B}(HT \rightarrow {}^3HeH^+)$	0.57	0.57
$\mathcal{B}(HT \rightarrow {}^3He^+ + H)$	0.22	0.22
$\mathcal{B}(HT \rightarrow H^+ + {}^3He)$	0.21	0.21

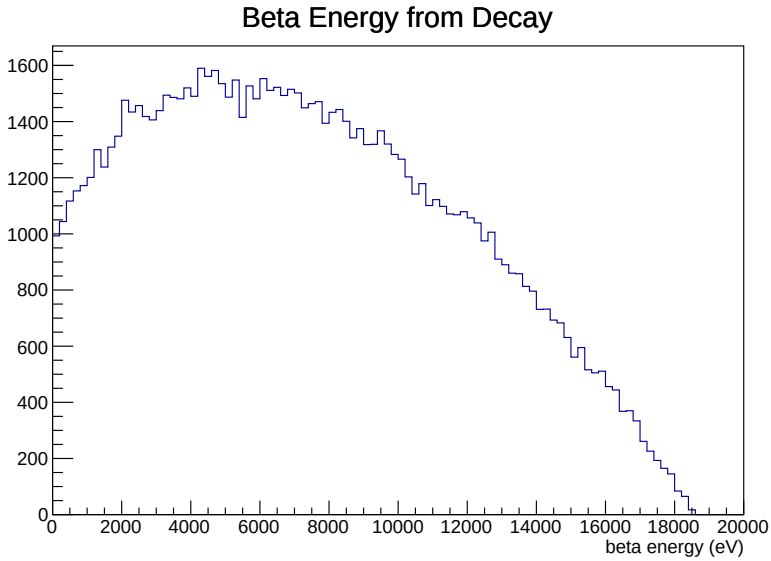

Figure 3.3: Beta spectrum from decay of T_2 in the TRIMS apparatus

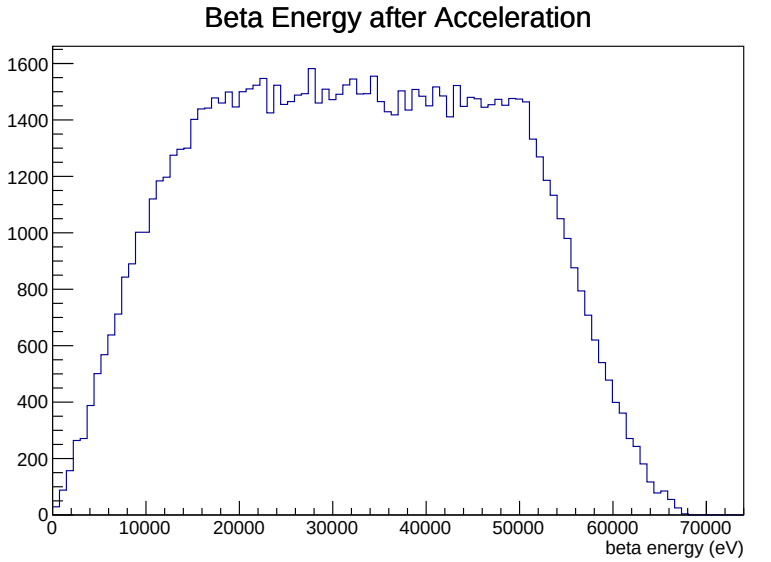

Figure 3.4: Beta energy spectrum after acceleration following the decay of T_2 in the TRIMS apparatus

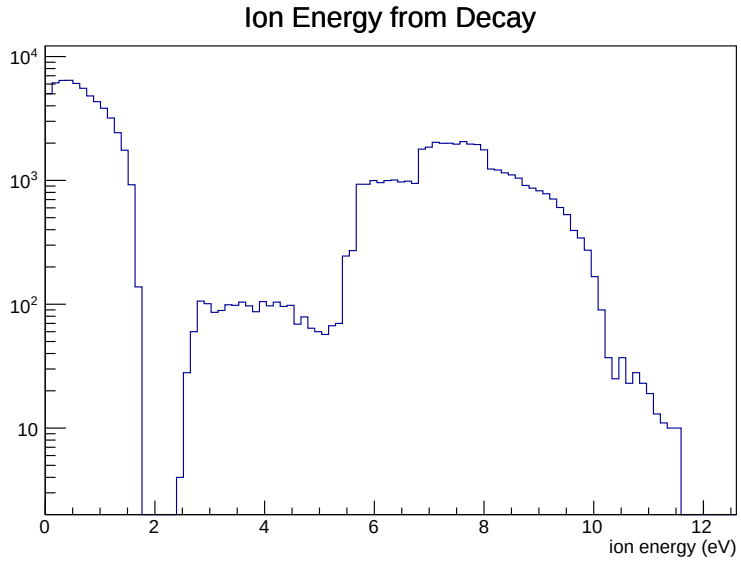

Figure 3.5: Ion energy spectrum from decay of T_2 in the TRIMS apparatus

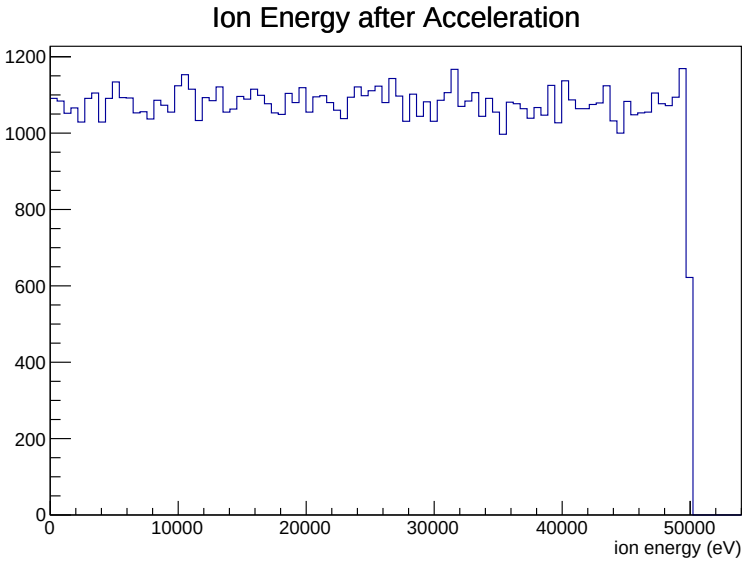

Figure 3.6: Ion energy spectrum after acceleration following the decay of T_2 in the TRIMS apparatus

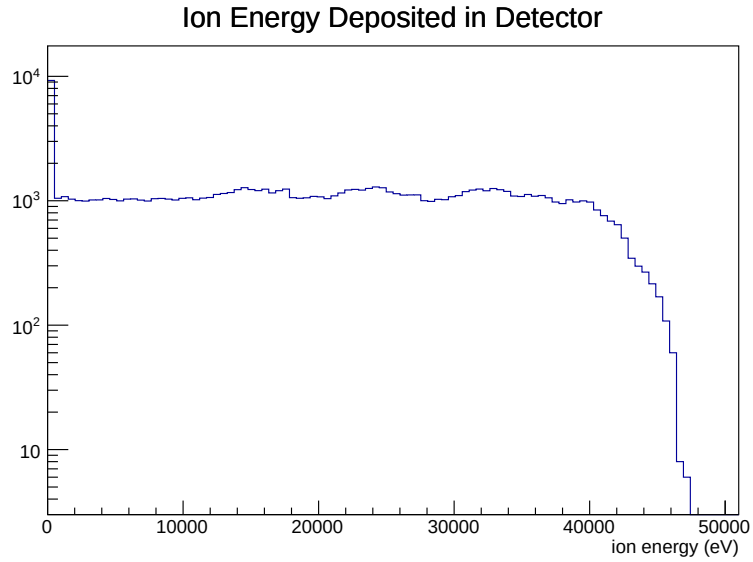

Figure 3.7: Ion energy deposition in the detector following the decay of T_2 in the TRIMS apparatus

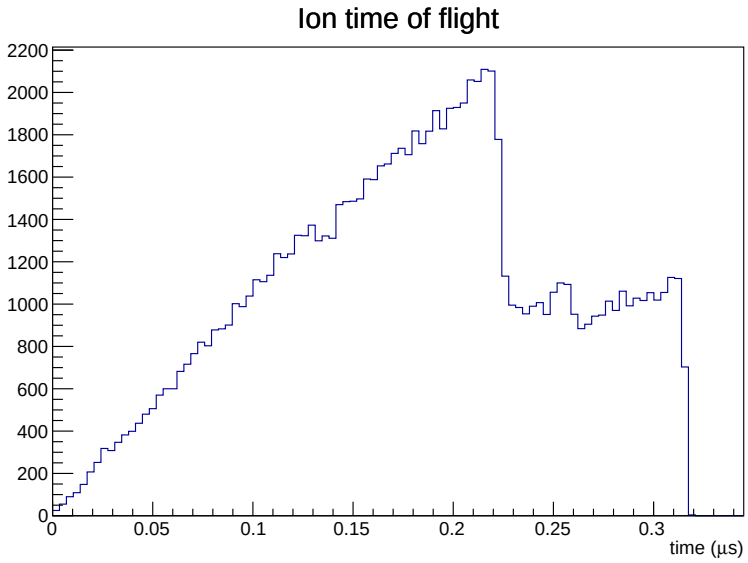

Figure 3.8: Ion time of flight for simulated decays of T_2 in the TRIMS apparatus

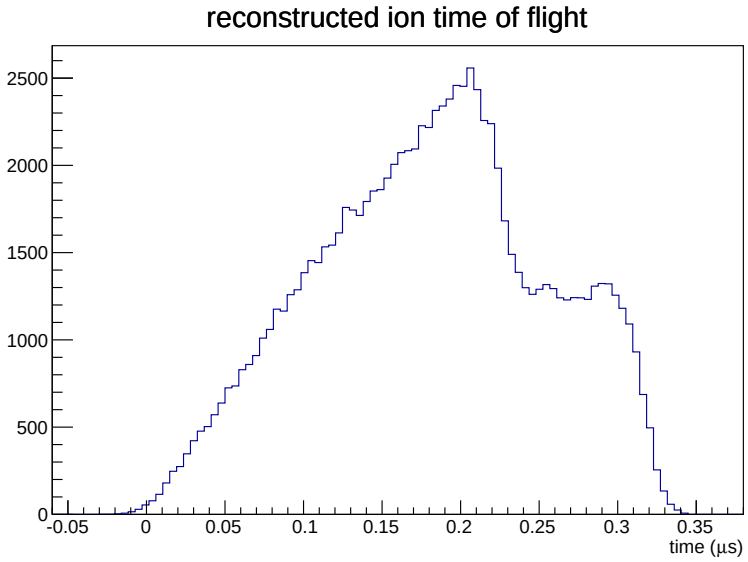

Figure 3.9: Reconstructed ion time of flight for simulated decays of T_2 in the TRIMS apparatus

histograms.

FSSim is currently a two-dimensional simulation, not accounting for the second transverse dimension. We are developing a three-dimensional simulation using the Geant framework [145, 146]. T. Lin, D. Parno and L. Bodine are benchmarking the model against the original simulation. The Geant version allows us to make use of the internal tracking code and visual event displays. Unfortunately the low energy physics packages in Geant are limited thus we use the SRIM energy deposition information and our own decay generator. The goal of the current campaign is to be able to quickly estimate systematics such as E-cross-B drifts. Geant simulation work is ongoing but early results are promising. The remainder of this section focuses on the FSSim package as it is further developed.

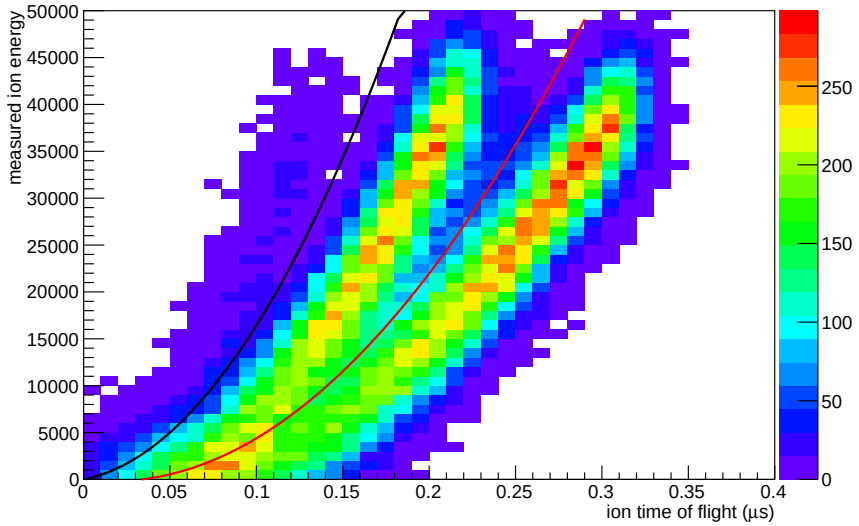

Figure 3.10: Ion energy versus time of flight of 100k simulated decays of T_2 and HT in the TRIMS apparatus with nominal parameters described in Table 3.1. The parabolic mass cuts are defined by the density profiles as described in sec. 4.5.

3.3 Extracting the Branching Ratio

The extracted molecular branching ratio is the number of observed mass-6 events relative to the total number of observed tritium beta decays (normalization). Determining the normalization requires removing background events, mainly mass-3 and mass-4 from HT decay. The clear visibility of the mass-1 events allows a data-driven reduction of the HT events in the region of interest. The process is as follows:

1. Data-taking: Take two data sets with different levels of HT contamination, preferably including one with a very high level of HT (see sec. 3.5.6 for details.) See fig. 3.2 and fig. 3.11.

2. Cutting: Make cuts on ion energy to fiducialize the volume. Make parabolic cuts in energy-vs-time-of-flight space to divide each data set into three regions labeled A (mass-1 like), B (mass-3/4 like) and C (mass-6/4 like). See fig. 3.10.

3. Normalization: Scale the high-contamination set to the low-contamination set so they contain the same number of events in the mass-1 region

4. Background subtraction: Subtract the scaled high-contamination data set from the low-contamination data set. See fig. 3.13.

5. Branching ratio extraction: Divide the number of remaining mass-6 events by the total number of remaining events to determine the branching ratio to the bound ion.

While this process eliminates nearly all HT events it also removes a fraction of the desired signal events arising from T_2 decays in the high-contamination data set. T_2 events are removed as the product of the scale factor between low- and high- contamination sets and the T_2 content of the high-contamination data set. For reasonably high statistics data sets this approach significantly reduces the overall normalization error,

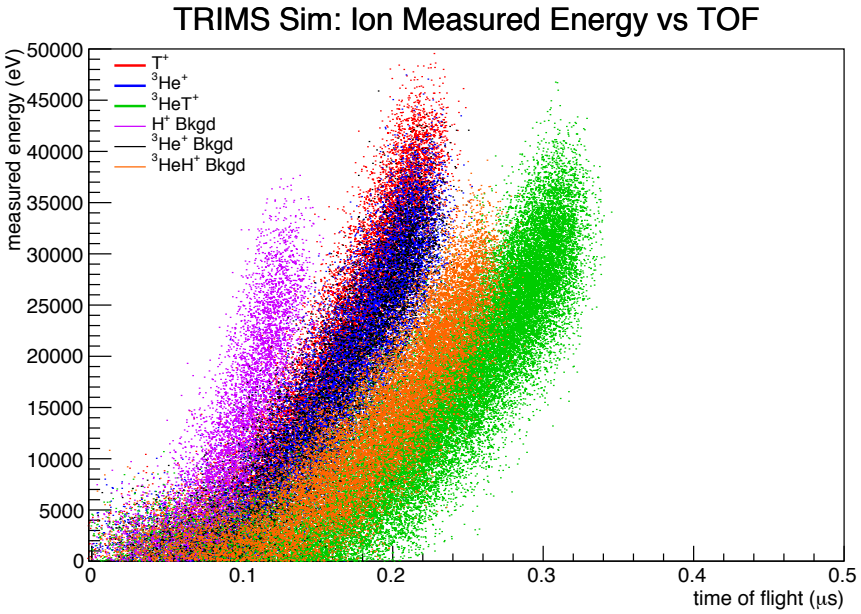

Figure 3.11: Ion energy versus time of flight spectrum for a high HT (30%) simulation of 100k events in the TRIMS apparatus.

reducing the uncertainty on the branching ratio. The data-driven background reduction is independent of any assumptions about the relationship between the branching ratios for T_2 and HT. In section 4.5 we provide a detailed description of the analysis approach, including simulation results.

The simulations show that for a 20-cm chambers timing resolution of $\sigma_{\Delta t} = 10$ ns and energy resolution of a $\sigma_E = 1.5$ keV are sufficient to provide sensitivity to the branching ratio. The desired resolutions are achievable with custom front-end electronics designed in the CENPA Electronics Shop and described in section 3.5.2. Furthermore, even for a fiducial volume crudely defined by energy cuts alone and a mass-6 energy cut estimated by average energy loss predicted by SRIM, the reconstructed branching ratio is within a few percent of the simulated value. See appendix A for a brief description of the analysis code used to determine the branching ratio.

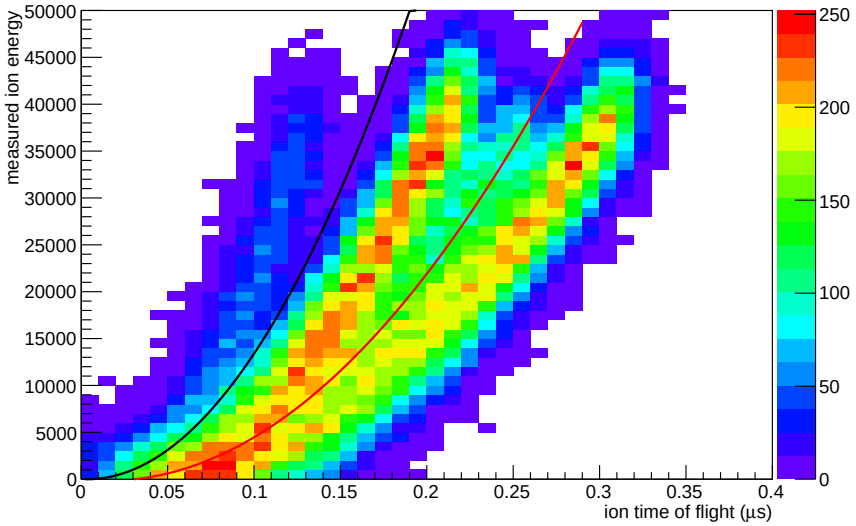

Figure 3.12: Ion energy versus time of flight of 100k simulated decays of T_2 and HT in the TRIMS apparatus with high HT parameters described in Table 3.1

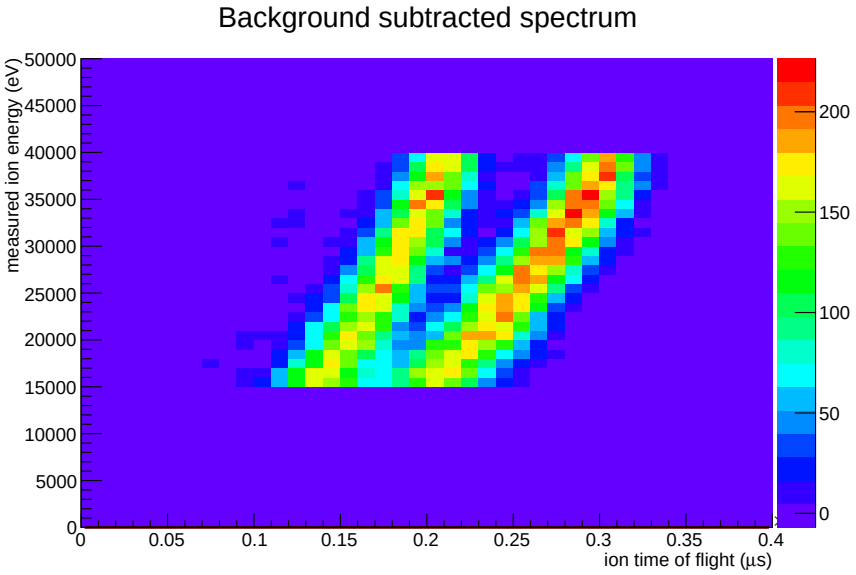

Figure 3.13: Difference between simulated high and low HT contamination energy-vs-time-of-flight distributions with fiducial volume cuts applied.

Table 3.2: Simulated branching ratios compared to branching ratios extracted by comparing simulations of low HT and high HT data sets. Note the analysis does not distinguish between T^+ and $^3He^+$ and does not extract the HT branching ratios.

Source	**Ion**	**Simulated $\mathcal{B}$**	**Extracted $\mathcal{B}$**
T_2	T^+	0.21	0.443
	$^3He^+$	0.22	
	$^3HeT^+$	0.57	0.557
HT	H^+	0.21	x
	$^3He^+$	0.22	x
	$^3HeH^+$	0.57	x

The background is expected to be negligible because the low pressure prevents signficant ionization, charge particles produced outside of the flux tube (such as off the stainless steel walls) cannot reach the detectors, and the background rates observed in test setups have been negligible. If the experiment does observe an unaccounted for background, runs with H_2 gas will allow us to explore the source in more detail. The time-between-events distribution will be used to estimate the livetime fraction and determine if a correction is necessary. Simulation work is ongoing and we plan to include other sources of background and geometrical efficiencies in future simulations.

3.4 Analytic Calculations

3.4.1 Pressure, Scattering and Source Activity

Balance between decay statistics and charge-exchange interactions determines the required chamber pressure. The partial pressure of tritium gas must be low enough to prevent charge-exchange interactions from ionizing the T_2 and contaminating the $^3HeT^+$sample. The peak hydrogen charge-exchange cross section is roughly $\sigma \approx$

10^{-15} cm^2 [147]. The scattering length is given by $\lambda \sim 1/n\sigma$, where n is the number density of the gas. Solving for n yields:

$$n(\lambda) = \frac{1}{\lambda\sigma} \sim \frac{10^{15}\text{cm}^{-2}}{\lambda}. \tag{3.3}$$

In order to limit the systematic error associated with scattering to the 1% level the mean free path much be 100 times larger than the average ion travel distance. To achieve a mean free path of 10^3 cm the molecular number density must be less than 10^{18} m^{-3}. For an ideal gas at room temperature this corresponds to a pressure of 4×10^{-5} mbar, readily achievable in an all-metal vacuum system.

The activity of the source (SA) is also proportional to the total number of tritium atoms in the volume.

$$SA = \frac{N}{\tau} = \frac{nV}{\tau} = \frac{pV}{kT\tau} = \frac{pV}{kTt_{1/2}} \ln 2 \tag{3.4}$$

For a 20-cm long main chamber and a 50-mm^2 detector the imaged volume is 10 mL. With energy-based fiducial volume cuts the imaged volume is lowered to roughly 5 mL. For an *atomic* number density of 2×10^{18} m^{-3} and a half-life of 12.3 years the source activity is ∼2 kBq. Thus the average time between imaged decays is 500 µs, assuring pileup events are rare.

The maximum data acquisition rate, assuming no pileup, is set by the sum of the maximum ion acceleration time and the throughput of the digitizer. The maximum time between the signal pulses is roughly 0.5 µs. The trace length required for accurate energy estimation pushes us to record significantly longer than a microsecond, thus decreasing the maximum event rate. The typical trace length is 33 µs corresponding to a maximum event rate of 30 kHz.

The scattering and source activity considerations fit nicely with a tritium partial pressure of 10^{-5} mbar. At this pressure the necessary statistics can be acquired over several days of running. The extra time compared to the source activity is required to account for the low coincidence efficiency and the ion detector positioning.

3.4.2 Time of Flight

At low pressures the ion time of flight can be modeled as ballistic motion. The electric field $V_{\text{chamber}}/L_{\text{chamber}}$ is independent of position and provides a constant acceleration a. The kinematic equation can be solved to find the ion time of flight in terms of ion charge q, ion mass m, initial velocity v_0, angle θ relative to the electric field and distance ΔD_{ion} between the decay point and the ion detector.

$$\begin{aligned} t_{\text{ion}} &= \frac{\sqrt{v_0^2\cos^2\theta + 2a\Delta D_{\text{ion}}} - v_0\cos\theta}{a} \\ &= \sqrt{\frac{v_0^2\cos^2\theta m^2 L_{\text{chamber}}^2}{q^2V^2} + \frac{2mL_{\text{chamber}}\Delta D_{\text{ion}}}{qV}} - \frac{mL_{\text{chamber}}v_0\cos\theta}{qV}. \end{aligned} \tag{3.5}$$

The initial kinetic energy of the daughter ion (1–26 eV) is much smaller than the energy acquired during acceleration ($\sim$ 25 keV). Thus the time of flight simplifies to

$$t_{\text{ion}} \sim \sqrt{\frac{2m\Delta D_{\text{ion}}L_{\text{chamber}}}{qV}}. \tag{3.6}$$

As shown in eqn. 3.2 the time of flight for mass-6 ions is $\sqrt{2}$ longer than for mass-3 ions and clear time separation of these events is possible. The separation for mass-1 and mass-3 appears roughly the same as the separation between mass-3 and mass-6 but there is not contamination from the intermediate (mass-2) state.

3.4.3 Particle Orbits

The actual paths of the beta and ion are helical. The mass m, charge q, initial speed v_0, angle between magnetic field and initial velocity θ, magnetic field B determine the gyroradius:

$$r = mv_0\sin\theta/qB. \tag{3.7}$$

The transverse speed depends on the kinetic energy (up to 1.7 eV for mass-6 ions and 26 eV for dissociated mass-3 ions) and the initial angle of the daughter momentum relative to the magnetic field. For a magnetic field of roughly 0.2 T the gyroradius of molecular ions should not exceed 2.5 mm and the gyroradius of dissociated ions should

not exceed 6.5 mm. The beta particles have energy up to 18.6 keV and subsequently the largest orbit has a radius of 2.3 mm. Measurement of the gyroradius of each ion species would allow comparison to the theoretical distributions. The details of such a measurement will be explored in future work.

In the transverse plane the atomic ion distribution extends to a radius of $R = R_{Det} + 2R_{\beta,max} + 2R_{ion,max} \sim 22$ mm, where R_{Det} is the detector radius. Several centimeters of clearance between the 4-in diameter beam tube wall and the ion-containing region provide an event-free region where the ion-detector can be placed for measurement of backgrounds and investigation of the ion distribution.

3.5 Hardware considerations

3.5.1 Detectors

The TRIMS silicon detectors are a low-leakage-current version of the 50-mm^2 area (4 mm radius), 500-μm thick Passivated Implanted Planar Silicon (PIPS) manufactured by Canberra (BKPD50-11-500AM). With an entrance window thinner than 50 nm, low capacitance of 25 pF and a room temperature leakage current of 10 nA [148], the PIPS detectors provide adequate energy resolution and threshold for ion detection as well as beta detection. An axial Microdot/SMA connector mounts the detectors and provides signal transmission.

The high-voltage end of the decay chamber contains a PIPS detector for beta detection. The beta detector floats at high voltage with the front-end electronics powered by rechargeable Li-ion batteries. A stack of 3-V button-cell lithium batteries (CR2032) supply the +110 Vdc bias . A reed switch turns on the detector bias when the magnetic field is turned on. Toggle switches on the electronics allow the power and bias to be turned on for testing when high voltage and magnet fields are not present.

The beta detector is mounted on a threaded tube connected to a 1.33-in Microdot-

BNC Conflat feedthrough. A thin stainless steel signal transmission rod is captured between the detector and feedthrough as the detector is mounted. The feedthrough is mounted on a bellows which allows us to tip the detector behind the electrode to shield it during high-voltage conditioning.

The low-voltage end of the decay chamber contains a second PIPS detector for ion detection. Given the appreciable gyroradius of the daughter ions, a single PIPS detector is not large enough to detect all recoil ions and the ion detector is mounted on a translation stage. We sample the recoil-ion distributions by scanning the ion detector radially across the end of the chamber. Corrections for the point spread function and geometric acceptances are applied to the data to extract the underlying distribution and examine the momentum distribution of the recoil ions.

The ion detector is mounted on a threaded tube clamped to the Conflat translation stage. The ion-detector signal travels along a stainless steel rod captured between the detector contact and a small insulator mounted at the translation-stage end of the mounting tube. From there the signal passes through a coil of stiff copper wire connecting to a BNC Conflat feedthrough. Glass insulating beads on the wire prevent shorting to the vacuum chamber. The helical wire configuration allows minimal displacement of the signal wire as the translation stage is actuated.

Canberra does not report the capacitance of the detectors and direct measurement is required to determine the input capacitance requirements for the preamplifier. To measure the capacitance when the detector is biased, an AC-coupled capacitance meter decouples the leakage current from the meter. Connecting the detector to an AC-coupled bias box and a capacitance meter splits the leakage contribution and reveals the capacitance of one detector (serial number: 98344) as 23.9 pF and the capacitance of the other detector (serial 98343) as 24.3 pF. The capacitance of the newest detector (serial number: 118088) is significantly higher at 41 pF. The capacitance of the detector BNC connector is 6.4 pF.

Unfortunately the direct measurements of the capacitance do not match the mea-

sured noise performance. For the older detectors the noise characteristics at low shaping time indicate a higher contribution, more consistent with the 43-pF value informally provided to us by Canberra. The performance of the electronics and offline filtering is sensitive to this contribution but is optimized based on data rather than capacitance measurements.

3.5.2 Electronics and Data Acquisition

Low-noise front-end electronics amplify the silicon detector signals. Tim Van Wechel, R. G. Hamish Robertson and David Peterson developed custom, resistive-feedback charge-sensitive preamplifers based on their previous design of the MAJORANA forward-bias preamp. The preamp front-end comprises a BF862 FET, a folded double-cascode stage, and a Darlington output stage from which the feedback is taken back to the gate. Figure 3.14 shows the schematic of the preamplifier design. Figure 3.15 shows the layout of the preamplifier. The first stage (FET) is run in unity gain mode while a second stage provides a factor of 10 gain. The PIPS detector bias is positive, thus the voltage signals are negative at the gate and positive at the output of the inverting preamplifier.

An on-board fiber-optic transmitter converts the output of the preamp to a light signal to allow transmission across the high voltage of the experiment. A fiber-optic receiver (previously used on the emiT experiment [149]) converts the signal back to an electrical signal for further signal processing and recording. The receiver is inverting and the voltage signals are negative at the output. A fiber-optic receiver on the preamp allows pulser signals to be sent across the high voltage for testing the electronics response *in situ*.

After amplification and fiber-optic conversion the signals are digitized by a 4-channel, 250 MS/s CAEN DT5720 desktop digitizer. The digitizer records the signal voltage every 4 ns for up to 128 μs. Digitizing the waveform allows signal pulse-shape analysis to extract energy and timing information. The downside of this approach

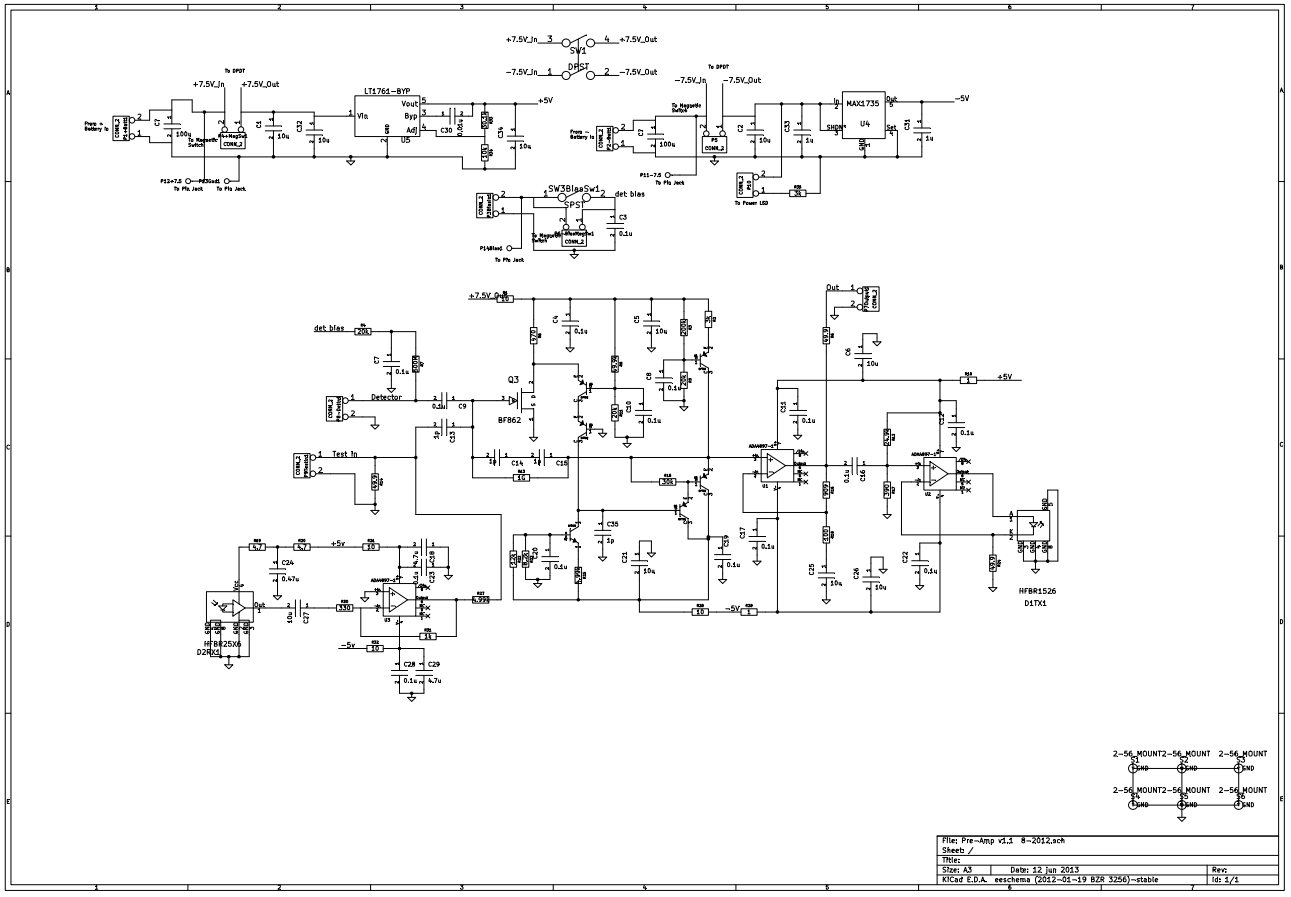

Figure 3.14: Schematic of resistive-feedback charge-sensitive preamplifier for TRIMS

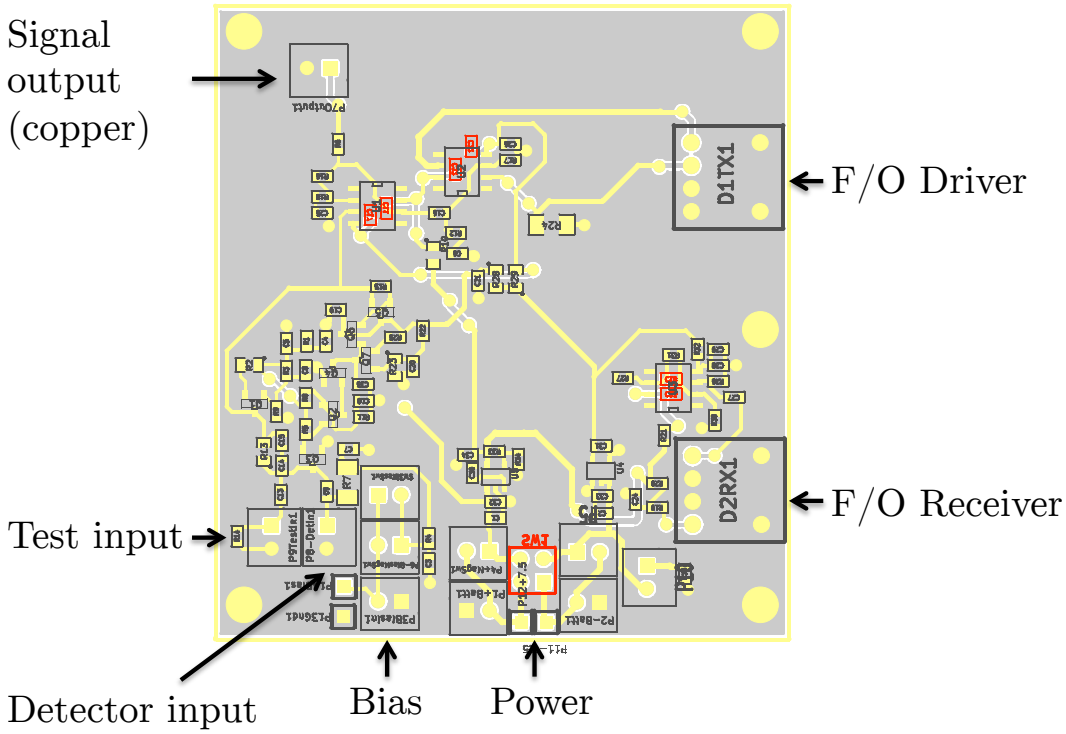

Figure 3.15: Board layout of resistive-feedback charge-sensitive preamplifier for TRIMS. (Figure produced by D. A. Peterson for fabrication.)

is that it necessitates post-processing to determine the ion energy, beta energy and time of flight as this specific digitizer does not have an on-board FPGA setup for the computations. The digitizer can be set to trigger on any individual channel or via an external NIM-logic-level trigger input. When a trigger occurs, the digitizer records the waveforms on each enabled channel with a common clock.

Online or near time processing is required to view the spectrum during data-taking. A NIM-based trigger is used to record coincident beta and ion detections. The trigger is done with fanned out signals from the preamplifiers. The signals from each preamplifer are fanned out with one path sent to the digitzer and another to the trigger setup. The trigger comprises a spectroscopic amplifier (Ortec 571), leading-edge discriminator (LeCroy 821) and a coincidence logic unit (LeCroy 622). The filtering of the spectroscopic amplifier is necessary to reduce the trigger rate associated with very high frequency noise. Singles rates are studied to monitor the source strength and estimate thresholds and efficiency.

The data is read out in Object-oriented Realtime Control and Acquisition (ORCA), a general-purpose data-acquisition program written and maintained by Mark Howe at the University of North Carolina, Chapel Hill[150]. ORCA performs both run control and slow controls, recording the relevant data in an SQL-based database. See section C.1 for more information about slow controls; see section C.2 for more information about the database.

A schematic outline of the signal processing chain is shown in Figure 3.16. Following acquisition the data is converted to ROOT files for analysis. We use the same file format for simulation as we do for the actual data. Thus we use the same analysis tools on both simulation and data, allowing direct comparison. See sec. 4.1 for more information on the data format.

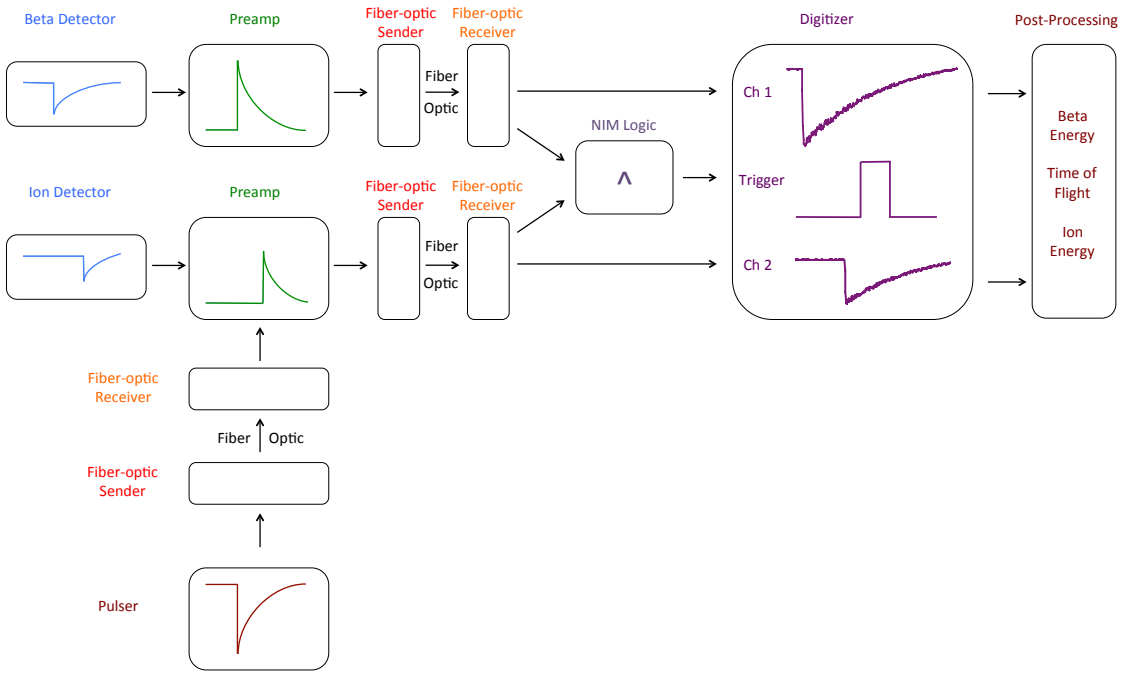

Figure 3.16: TRIMS signal processing chain. The link between the preamp and digitizer is fiber-optic for high-voltage isolation; all other connections are copper.

3.5.3 Calibration

Calibrations consist of runs with photoelectrons generated by a UV light source, gammas from an americium-241 gamma source, artifically generated voltage signals from a pulser, and monoenergetic conversion electrons from a krypton-83m source.

Photoelectrons generated by UV light calibrate the energy scale. Light from a Spectroline short-wave lamp enters the chamber through a UV window behind the translation stage. The light scatters off the chamber walls and shines on the stainless steel detector housing. As a result of the magnetic field and the high accelerating potential only electrons from the region of the chamber directly opposite the detector are imaged. Hence the detected electrons have accelerated through the full potential and an energy calibration is obtained by varying the high voltage setting. The de-

tectors are aligned by examining the rate at different beta detector tilt positions in which the housing to the ion detector is in the line of sight of the beta detector. An effective ion energy scale can be inferred from the electron calibration with the use of SRIM [143] compiled energy deposition data.

A secondary energy calibration uses the 59.5-keV gamma peak from a 100-μCi americium-241 source placed outside the acceleration chamber aluminum housing. The width of this peak is a good measure of the energy resolution of the electronics and is regularly monitored to check performance.

In addition to the two-detector calibrations a pulser is used to monitor the response of the front-end electronics, check linearity and monitor for drifts. A dedicated fiber-optic receiver incorporated into the preamplifier design electrically isolates the preamp from the pulser, allowing the pulser signal to be used in the high voltage environment.

A krypton-83m calibration is used as a proof-of-principle for the TRIMS experiment. Details of the activation and measurement of the source are discussed in chapter 5.

3.5.4 High Voltage

The nominal high voltage of the TRIMS experiment is 50 kV. An LG-80P-1.5 Glassman power supply and a resistive chain surrounding the decay chamber provide the linear accelerating potential. The system is operated single-ended with the ion-detector side held at ground potential. In this configuration the full potential is maintained between the magnet bore and the vacuum chamber. A 3-mm thick quartz tube surrounding the vacuum chamber and sitting inside an aluminum enclosure prevents breakdown. The enclosure can be filled with dry N_2 gas to further suppress high voltage discharge as even microdischarges influence the electronics.

Metal electrodes mount flush with the glass-to-metal seal on the inside and outside of the glass. This setup mimics a parallel plate and ensures the potential gradient in the detection region is well-defined and as uniform as possible. On the beta-detector

side the inner electrode is welded to a tube extending from the Conflat flange on the main chamber. A second, polished electrode is mounted on the structural plate and held in place by a nut installed from behind the plate.

On the ion-detector side the electrode is mounted from a ring installed in the 4-in tube of the reducing cross that holds the detector mount. Four rods extend from the ring to support the electrode. A slot in the ground electrode allows the ions to pass the electrode. The slot extends to the full radius on the top of the chamber but does not extend to the bottom so the electrode can shield the detector during high voltage conditioning. Figure 3.17 shows the engineering drawing of the main chamber and detector mounts.

The experimental chamber and front-end electronics float at high voltage. Fiber-optic transmitters electrically isolate the front-end electronics and allow for signal extraction across the high voltage. Fiber-optics are only needed on the high-voltage (beta) side, allowing both copper and fiber connections to be used on the grounded (ion) side. The non-linear response of the fiber is characterized by directly comparing the pulser signals observed on the fiber-optic and copper lines. The standard setup operates symmetrically with fiber-optic connections on both sides. We will take runs with copper at the ion (grounded) end to examine the effect of lowering the threshold (see section 4.3.1).

Voltage and current taps allow monitoring of the power supply output. The voltage and current are recorded with the use of LabJack ADCs read out in ORCA. Refer to section 3.5.2 and section C.1 for more information on slow controls.

3.5.5 Vacuum System

The all-metal-sealed, tritium-compatible vacuum system consists of the experimental chamber, a molecular-tritium acceleration chamber and a vacuum manifold. Figure 3.18 shows a schematic of the vacuum system. The main vacuum manifold is comprised of Conflat hardware while the gas-handling manifold is comprised mainly

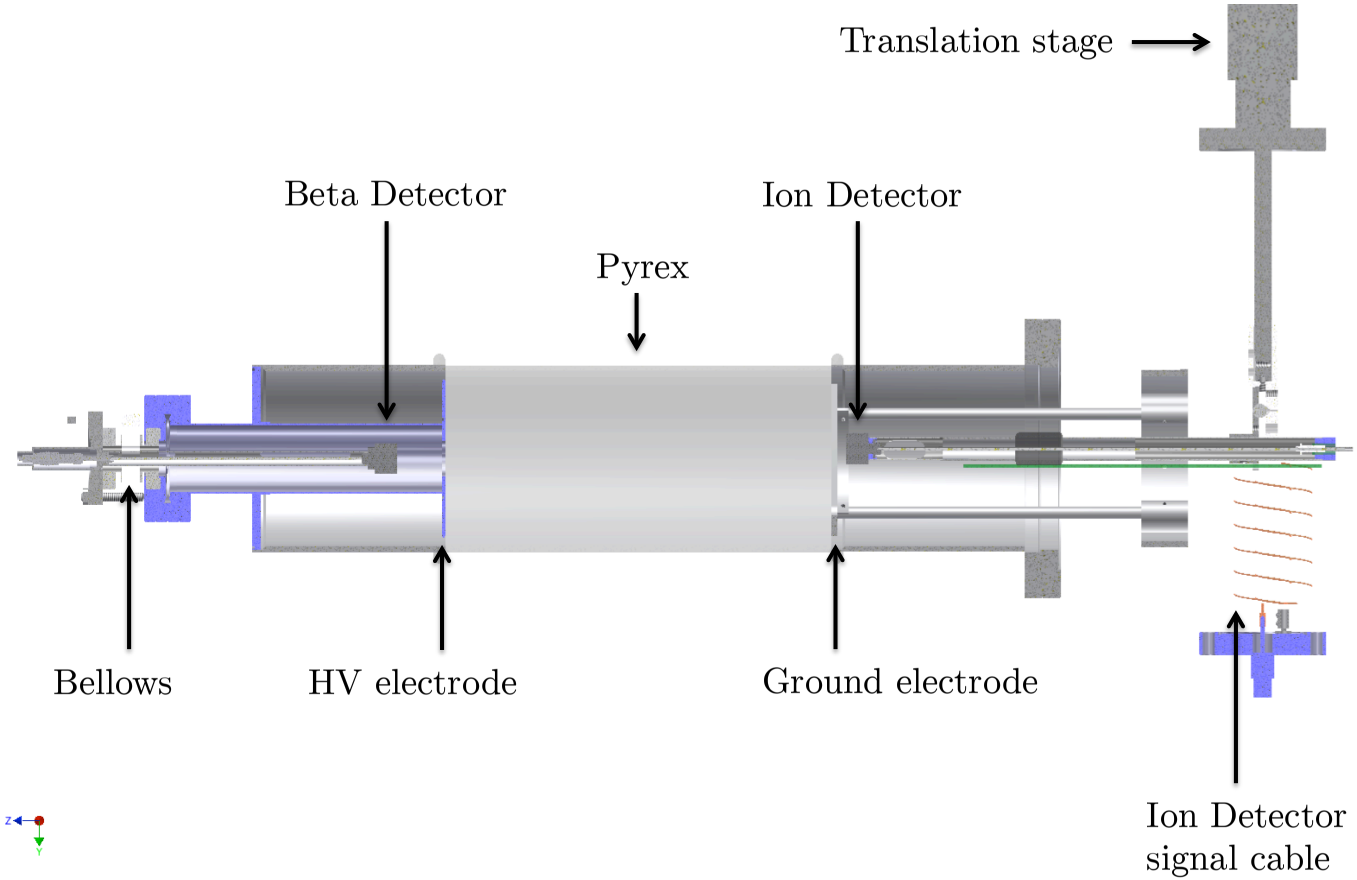

Figure 3.17: Engineering model section view of the acceleration chamber and detector mounts

of VCR hardware.

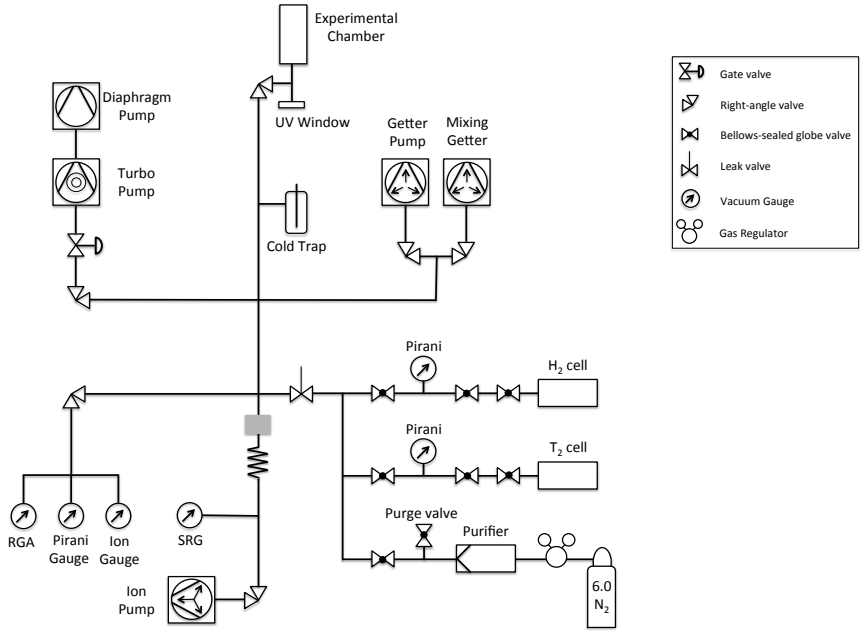

Figure 3.18: TRIMS vacuum system schematic

A double-ended glass-to-metal seal acts as the experimental chamber. The 4-inch diameter, 20-cm long PYREX tube joins 4-inch stainless steel tubulations at each end. A 2.75" Conflat flange is welded to the beta (HV) end and a 6" Conflat flange is welded to the ion (ground) end. The beta detector mounts on a 2.75-inch-Conflat-flanged BNC-Microdot (10-32 thread) feedthrough on the HV-end of the decay chamber. The ion detector mounts on a 2.75-inch-Conflat-flanged linear-translation feedthrough which attaches to the detector system via a Conflat reducing cross. The ion detector signal is routed to a 2.75-inch-Conflat-flanged BNC-pin feedthrough in the Conflat flange mounted on the 2.75-in flange opposing the translation stage.

A Pfeiffer HiCube Eco80 diaphragm-backed turbomolecular pump and an ion

pump evacuate the vacuum system. The valve to the turbomolecular pump closes during standard runs, providing a completely sealed system. During tritium runs a liquid-nitrogen-cooled cold trap maintains the low pressure. During bake-out of the vacuum system the turbomolecular pump station is used to handle the gas load. The turbomolecular pump connects to the system by a 2-foot Conflat bellows attached to a right-angle valve. During data-taking the valve closes and turbopump is removed.

A nonevaporable getter (SAES SORB-AC Mk 5 pump with ST-101 getter material) provides additional low-pressure pumping. The getter pump traps tritium prior to venting as a means of minimizing the amount of radioactive materials vented to the atmosphere. A second getter utilizes the reversibility of hydrogen adsorption to mix tritium and hydrogen as discussed in sec. 3.5.6. Each getter sits in its own 4.5"-Conflat full nipple which connects to the main vacuum system by its own right-angle valve.

A full complement of vacuum gauges monitors the system pressure during various stages of pumpdown and operation. A Pirani gauge, a nude ion gauge, and a spinning rotor gauge (MKS, SRG-3) provide coverage of pressures ranging from atmosphere to 1×10^{-9} mbar. A residual gas analyzer (RGA, SRS RGA-100) measures partial pressures between 1×10^{-4} and 6.5×10^{-11} mbar for masses up to 100 u. The Pirani gauge works at atmospheric pressure and monitors the initial pump down. The nude ion gauge and RGA intermittently monitor the pressure in the chamber but are generally off during data-taking because they pump tritium. During standard operation the spinning rotor gauge operates continuously. Only the nude ion gauge functions at the high bake-out temperature and the gauge provides continuity of measurement from before and after bake-out. An extra set of gauges (Pirani, nude ion gauge) attach to the turbopump line during bake-out for extra monitoring.

The gas line portion of the vacuum system mainly consists of VCR parts with Conflat pressure reduction chambers connected to the main chamber via a leak valve (NorCal LL-275-133). The tritium gas is kept in a separate metal cell connected to

the main chamber by a series of valves designed to reduce pressure, prevent accidental exposure to tritium, and allow removal of system components for maintenance work. A Pirani gauge monitors the pressure in the tritium line during transfer to the main chamber. A second metal cell houses hydrogen gas for HT mixing.

A high-temperature bake-out of the vacuum system reduces the residual hydrogen content in the chamber prior to introducing tritium. For bake-out, heating tapes wrap around the system and heat to a temperature of ∼230°C. The maximum tolerable temperature of each component was carefully considered during the design and selection process. Section B details the bake-out design and equipment. The design goal is a pressure on the order of 10^{-11} mbar.

The decay chamber is a custom double-ended adapter manufactured by Larson Electronic Glass and modified by the UW Physics Instrument Shop. The translation stage is a standard Kurt J. Lesker push-pull translation feedthrough (KLPD) with a 4-inch range. The main valves on the vacuum system are Conflat, all-metal right-angle valves manufactured by VAT, Inc.

The main vacuum manifold valves are all-metal right-angle valves with Conflat flanges and manual actuation. The leak valve for introducing tritium is a Norcal LL-275-133 with a minimum leak rate of 10^{-10} torr-l/s. The gas-line valves are all-metal globe valves manufactured by Nuclear Products Company (also known as Nupro, now a subsidiary of Swagelok Company) with 0.5-inch VCR connections. The tritium and hydrogen chamber valves are all-metal globe valves from Swagelok with 0.25-inch VCR connections. Two Viton®-sealed gate valves from VAT with Conflat flanges isolate the turbomolecular pump and sorption pump from the system. These valves are only used for high pressure pumping and are not exposed to large amounts of tritium which would degrade the elastomer seals.

All vacuum chamber components are considered tritiated and are only reusable on tritium systems.

3.5.6 HT Mixing

The TRIMS background reduction method requires the ability to vary the HT content of the source gas. An initial low HT level is achieved through high-temperature bake-out of the system. Later, a high HT level is achieved through mixing hydrogen and tritium in a SAES St-101 (84% Zr, 16% Al) getter [151]. Following the initial run, we will pump out the T_2 remaining in the vacuum system and open the valve to the mixing getter in order to allow known quantities of H_2 and T_2 into the vacuum system. The hydrogen and tritium will be pumped by the mixing getter in atomic form. When we heat the getter, the atomic H and T will desorb, forming H_2, HT, and T_2 molecules. The H_2 level is important as it affects the mean free path of the beta and ions. We will keep the pressure in the system constant to keep the scattering length significantly longer than the chamber. The background subtraction method remains practical as long as the HT-to-T_2 ratio can be elevated above that of the earlier data run by at least 10 percentage points.

SAES getters adsorb atomic hydrogen in a reversible process [151]. The process is a balance of the adsorption rate k_a and the desorption rate k_d. For example hydrogen pumping on St-101 getter material is described as:

$$H_2 + 2(ZrAl) \underset{k_d}{\overset{k_a}{\rightleftharpoons}} 2(ZrAl - H). \tag{3.8}$$

The rates are generally expressed as exponentials $k = be^{c/RT}$. While the adsorption and desorption rates may differ for each isotope, the St-707 desorption rates for protium, deuterium and tritium are all consistent within error bars [152]. Unfortunately data on the rates for St-101 are not readily available. The important thing to note is that the analysis technique does not require exact knowledge of the HT fraction and differences in desorption are not likely to cause the mixed gas to be unuseable. The expulsion of larger amounts of H than T will result in high H_2 values but will not adversely affect the HT to T_2 ratio.

For a fixed loading, the desorption rate depends on the mass, so isotopic loading must offset this difference. Higher levels of protium loading are required to achieve equal desorption. Initial calculations indicate that uniform mixing requires introducing an H_2 load 5.4 times larger than the T_2 load. Higher mixing temperatures bring the desorption-rate ratio, and thus the optimal load ratio, closer to 1.

3.5.7 Magnetic Field

A solenoidal magnet field ensures that for beta decays visible to the beta detector the ions are contained within the chamber. Some of the ions have appreciable transverse momentum and the gyroradius is accounted for in the design. For a single reasonably sized ion detector the magnetic field to focus all ions is 1 T. Such a field cannot be achieved over a large volume with copper coils, requiring expensive superconducting coils. The TRIMS design compensates for lower magnetic fields by scanning the detector across the diameter of the chamber, sampling the ion distribution as a function of radius. This requires a field of 0.2 T to constrain the ions within the central part of the chamber.

The 0.2-T magnetic field is provided by a double Helmholtz arrangement composed of four coils recovered from Varian NMR magnets. A Varian V3400 NMR magnet was recovered from the Physics Astronomy Building where it had not been used in 20 years. A Varian V3401 magnet was purchased from BMI surplus. Danfysik 823 regulated magnet power supplies, taken from the decommissioned CENPA LINAC, provide the magnet current.

The inner pair of coils were part of the V3400 magnet and have a 23-cm bore, 9-cm depth and 56-cm outer diameter. The coils can run at $\sim$140 A of current, 40 VDC. The outer coils were part of the V3401 magnet and have a 25-cm bore, 10-cm depth and 58-cm outer diameter. The maximum operating current of these coils is unknown but they have been successfully operated at 140 A.

The standard configuration consists of all coils running at 140 A with a 15 cm gap

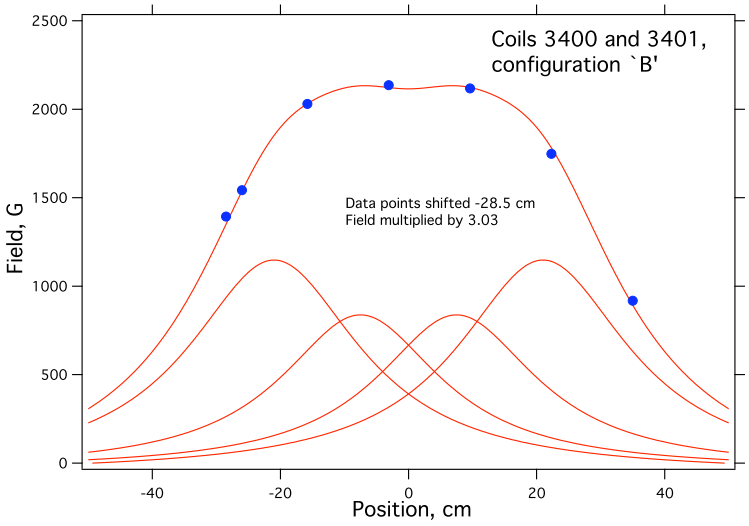

Figure 3.19: Red lines are the predicted axial magnetic field from each coil and the sum. Blue dots are from a field survey done at 46 A that was scaled to 140 A. (Figure made by R. G. H. Robertson.)

between the midplanes of the inner pair and a 42 cm gap between the midplanes of the outer pair. Figure 3.19 shows the predicted axial magnetic field strength in this configuration, "configuration B." Also shown is data taken at 46 A of current scaled to the full current. The measured magnetic fields are in good agreement with the predicted field values.

The magnet coils and power supplies require water cooling. The power supplies require 208-VAC, 3-phase, 40-A power. In the CENPA Hot Lab, where the experiment will be performed, the high voltage power is drawn from the neighboring ATHENA cluster and the cooling water is drawn from the CENPA cooling tower. In room B037 of the UW Physics and Astronomy building, where the experiment is being constructed and calibrated, the high voltage power is drawn from the breaker panel PCB-BNO-N4 and the water is provided by the Physics Department Chilled Water system.

The magnets are installed on a movable stand with the solenoid axis in the horizontal position. The coils mount in a u-channel that can slide along the stand to allow access to the vacuum system without repositioning the stand itself. Delrin® spacers and aluminum clamps maintain the distance between the coils. A water distribution bar on the stand distributes cooling water to the coils, which are connected in parallel. Electrically the two pairs of coils are independently wired with the coils within a pair connected in series to their own power supply. The inner and outer pairs can be run at the same or different currents as needed to produce different field configurations. All coils at the same current provides the standard field configuration of 2.13 kG axial field uniform to better than 1% over the length of the chamber.

3.5.8 Inventor Model

We use a full three-dimensional Autodesk Inventor model of the TRIMS apparatus to help determine dimensions of parts and aid design. The majority of the model was constructed by T. H. Burritt and D. S. Parno with the krypton section added by L. I. Bodine. Fig. 3.20 shows one view of the full assembly model.

3.5.9 Laboratory Preparations

The intial krypton calibration is performed in the Physics & Astronomy Building Lab B037 to allow easy access to the cleanroom facility in case of a need to revamp the vacuum system.

The tritium experiment is performed in the CENPA Hot Lab, which is authorized for the use of radioactive isotopes. The lab is kept at negative pressure by two fume hoods with make-up air coming from the high bay. For safety the laboratory is locked to prevent unauthorized access to the tritium area. The Hot Lab is considered a restricted access area and personnel are required to wear radiation badges (Landauer Luxel+) while in the laboratory. These badges are not sensitive to tritium and we

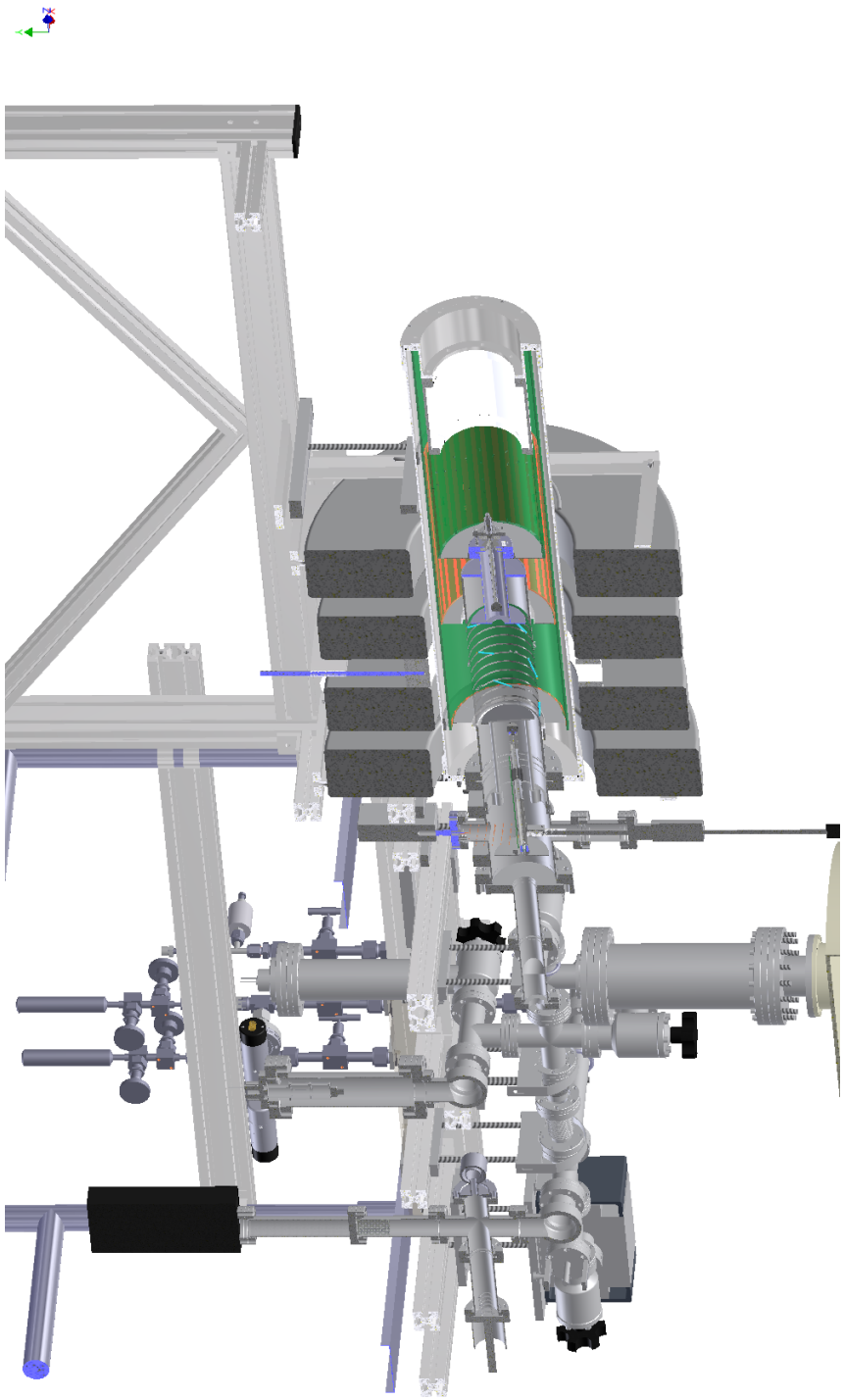

Figure 3.20: Cut-away view of the TRIMS inventor model

implement separate monitoring for personnel by arrangement with UW Environmental Health & Safety. Doug Will, a UW Radiation Safety Office Authorized User, and Eric Smith have cleared the lab of unnecessary materials, surveying for radioactivity as necessary.

Upgraded electrical and water connections in the lab meet the needs of TRIMS. In addition to the original three 120-VAC, 20-A circuits in the lab a QO load center with a 40-A capacity provides 120-VAC circuits. Two 208-VAC, 3-phase, 40-A circuits are drawn from the neighboring ATHENA server room. See section D for detailed power requirements.

Recirculated water for cooling the magnet power suplies and coils is drawn from cooling tower and routed to the Hot Lab via the ATHENA server room. Three 4-in diameter wall cores accommodate the required power and water lines between the lab and server room. The water lines are separated from the power lines in accordance with electrical standards. The third core is used for signal transmission such as ethernet service.

3.6 Statistical and Systematic Errors

The error on the branching ratio $\mathcal{B}$ can be broken down into statistical and systematic components. The expected sources of errors are listed below along with our plans to address them.

3.6.1 Statistical errors

The analysis consists of two data sets cut into three regions: A (mass-1), B (mass-3 and mass-4 background), and C (mass-6 and mass-4 background). For a detailed description of the branching ratio extraction see sec. 4.5. The branching ratio $\mathcal{B}$ can be written in terms of the counts in each region for the two runs:

$$\mathcal{B} = \frac{N_{C1} - \frac{N_{A1}}{N_{A2}} N_{C2}}{N_{B1} + N_{C1} - \frac{N_{A1}}{N_{A2}}(N_{B1} + N_{C1})} \tag{3.9}$$

The statistical errors on the counts N_i in each region (A1, A2, ...) are Poissonian with $\sigma^2 = N_i$. We treat the counts in each region as independent because they are drawn from Poissonian distributions. The position of the cuts between the two regions does introduce a small systematic effect. This systematic is negligible as it comes from mass-4 contamination that is statistically removed by the subtraction method.

The counts N_i in each region can be as treated independent and the statistical uncertainty on each is at most a few percent. Thus standard error propagation methods can be used and the statistical error takes the form:

$$\sigma^2_{\mathcal{B}\,\mathrm{stat}} = \sum_i \left(\frac{\partial \mathcal{B}}{\partial N_i} \right)^2 N_i. \tag{3.10}$$

3.6.2 HT Contamination

The level of HT contamination can be kept low by following good vacuum practices (see section 3.5.5) including a high-temperature bake-out. The method outlined in sec. 3.3 minimizes the effect of remaining contamination. Runs are temporally separated and this technique is sensitive to long term field drifts and the time sequence of measurements must be carefully considered.

The background subtraction technique cuts an appreciable fraction of signal events in addition to background, dramatically affecting statistics. While subtraction can introduce systematic bias toward a given ion species the simulation (see sec. 3.3 does not show systematic bias for reasonable statistics (100k events). For simulations with low statistics, the impact of statistical fluctuations reduces sensitivity but does not appear to introduce a species-dependent effect.

3.6.3 Magnetic Field Stability

Monitoring of the magnetic field stability is necessary to ensure collection efficiencies do not vary over time. Short runs and defined reference values, such as the coincidence rate at the central position, look for short-term field drifts.

We do not directly monitor the field outside the decay chamber as the measurement precision would not exceed the precision of the current stabilization. Monitoring the current and voltage of the power supplies is difficult because the supplies are older units without full instrumentation. A computer interface for the supplies exists but is severely outdated. A LabJack readout is planned but is not yet implemented.

3.6.4 Electric Field Uniformity

Maintaining the electric field uniformity both across the transverse plane and along the axis is essential. We plan to look for broken symmetries using Fe-55 induced electrons tthat are kicked out from the walls of the chamber and are collected on the detectors with the high voltage polarity switched back and forth. Differences in the collection efficiencies would reveal broken symmetries that can potentially be identified.

3.6.5 Field Alignment

The relative alignment of the electric and magnetic fields determines the acceptance of the system. A very rough calculation shows that a 1-cm misalignment between E and B at one end of the chamber would result in a 6-cm displacement from E×B drift (assuming 1 μs ion time, 20-cm chamber, 0.2-T constant magnetic field). Thus mm-level precision on the alignment is necessary. The solution is good mechanical alignment but this is made difficult by the long lever arm on any alignment measurement. During normal operation the decay chamber is shrouded. Thus all alignment measurements are done on the reducing cross rather than the chamber itself. Once the

alignment is set, saddles clamp the vacuum system to stand, reducing the likelihood of movement between runs.

The krypton calibration run data rate can be used to check alignment. The decay produces two electrons within a short window. With magnetic field on but high voltage off, half of the decays should produce a coincidence in the two detectors. Thus the rate of coincidence between the higher energy and lower energy conversion electrons is related to the alignment of the mechanical and magnetic axes. The beta detetor tipping mechanism allows side-to-side adjuments to check the rate as a function of detector position. Tipping the detector does slightly change the area but for small angular deflections this does not present a problem. Larger deflections can be achieved by physically shifting the vacuum system on the stand.

3.6.6 Moving/Positioning the Detector

We investigated the reproducibility of the positioning of the ion detector. Motion-induced vibrations in the ion detector/mount are possible and we investigated the movement and positioning. Vibration of the detector on the mount occurs during detector placement and when the side of the vacuum system is tapped. The bulk of these motions relax within a second. Movement of the vacuum system when the detector is not being positioned should be minimal but we will measure noise performance *i*n situ.

We measured the reproducibility of detector positioning in the cleanroom to avoid contaminating the vacuum system components during testing. We installed the detector mount on the reducing cross with the translation stage. Using the translation stage to set the detector position we measured the distance between the detector and the table. We repeated these measurements going down and coming back up. We had two people measure and record the distances without discussion. We found that the positioning was reproducible to within 0.25 mm, the precision of the translation stage readout. The positioning precision is sufficient for the purposes of scanning the

detector.

The accuracy of the detector position is more difficult to determine and the symmetry of the trigger rates on either side of perfect alignment determines the center. We measure the actual position using the translation stage, referencing distances relative to the central position. The side-to-side detector position is optimized using the tilt of the beta-detector-mount bellows.

3.6.7 Fiducial Volume Cuts

The acceptance of the device varies with position and orientation of the decay. A fiducial volume cut rejects events from decays in regions near the detectors where detection is strongly dependent on the beta momentum.

The most basic fiducial volume cut is a hard cut on ion energy. Flat energy cuts (E_{high} and E_{low}) image slightly different volumes for mass-1, mass-3, mass-4, and mass-6 ions. This effect is visible within the simulation but a more detailed, quantitative analysis is necessary to correct for this bias. Future analysis work will investigate the optimal fiducial volume cuts.

3.6.8 Energy Reconstruction

A trapezoidal filter provides reliable energy determination from the digitized waveforms as described in section 4.3. The filter parameters (integration time, filter gap) are optimized in offline analysis based on the noise environment and leakage current of the detector. The original TRIMS simulations assumed a very conservative $\sigma_E = 3$ keV electronics energy resolution. While the electronic noise is the limiting factor in the beta energy reconstruction the ion energy reconstruction is limited by the spread in energy loss in the dead-layer. While the dead-layer is traditionally treated as completely inactive, we treat it as a 100-nm thick half-active region in accordance with recent detailed measurements of energy deposition in thin silicon detectors [144].

One possible issue is temperature-induced fluctuations in ADC/FET signals. Runs taken right after a cold-start of the electronics reveal a small time dependent drift that could be associated with temperature.

3.6.9 Timing Reconstruction

A single common clock with synchronous readout of all digitizer channels provides stable relative timing between the signals. Timing resolution is limited by the sampling rate, trapezoidal filter software, and jitter in the fiber-optic sender risetime. The comparison of the fiber-optic and copper connection on the low-voltage side provides an online assessment of the the timing jitter. Timing jitter runs require swapping fiber-optic senders between high- and low-voltage sides of the system. The effects of temperature fluctuations on the timing jitter have yet to be determined but standard operating procedure is to run electronics for at least 30 minutes prior to data runs to be used in the physics analysis.

Secondary electrons produced by ion incidence on the detector have clear timing and energy. Studying events where ions produce secondary electrons that are detected in time-delayed coincidence provides an *i*n situ measure of the timing resolution with real detector signals.

3.6.10 Triggering

The throughput of the digitizer is limited to 30 MB/s. The corresponding event rate depends on the number of samples and number of active channels. For the nominal TRIMS setup with 8k samples and two channels the highest trigger rate is 30 kHz. A low threshold is desired to ensure that low energy ions are not missed. The digitizer internal trigger is susceptible to high frequency noise thus an external trigger utilizing a filtered signal limits the data rate. The effect of the trigger on the resulting spectra is taken into account in determining the trigger conditions. While the trigger threshold

imposes an energy cut on the signals, this cut is more inclusive than the fiducial-volume cut, thus limiting the impact of the trigger setting on the analysis. Early runs provide information necessary to optimize the coincidence window.

Runs with triggers on either detector provide comparison with the coincidence data to examine bias introduced by the coincidence trigger. Random trigger data (pulser software trigger rather than signal trigger) quantify pileup and accidentals.

Chapter 4

TRIMS DATA ANALYSIS

In this section we describe the TRIMS data analysis techniques and elaborate on the run plan. First we describe data format and data processing required to extract the physical quantities of interest. In the middle sections we discuss how we analyze the physical quantities (energy, time of flight) to extract a branching ratio from the data. In the final section we outline the run plan as it relates to the statistical uncertainties on the branching ratio.

4.1 Analysis parameters

Object-oriented Real-time Control and Acquisition (ORCA) (described in section 3.5.2) records the TRIMS waveform data in binary files with custom format. The ORCA files are converted to ROOT trees [142] using a custom data processor added to OrcaRoot [153].

The data tree contains one entry for each trigger of the CAEN DT5720 digitizer. Each entry contains the waveforms for all active channels, each stored in its own branch. The waveform peak height and relative timing are reconstructed during post-processing and the values are appended to the tree. The main values used in the analysis are the peak height of waveform0, the peak height of waveform1 and the time difference between the two signals.

The peak height of waveform0 is associated with the beta energy. The peak height of waveform1 is associated with the ion energy. The timing difference is asociated with the ion time of flight. This provides the necessary variables to produce the energy-time-of-flight spectra needed for analysis.

4.2 Data run plan

For general data-taking we employ a two-fold coincidence trigger using NIM logic. For background analysis we look at singles events as a means of estimating the accidental coincidence rate as well as to look at estimates of secondary electrons.

4.2.1 Single events

Data runs taken with a single-detector trigger help test systematics and establish performance of the system. Runs with only an electron trigger included show the beta spectrum along with background sources of electrons and any sources of negative ions. Runs with an ion detector singles trigger provide information about backgrounds and other physics processes occurring within the detection volume. Runs with only an ion trigger can determine the level of ionization of the gas from outside sources including cosmic rays, high voltage microdischarges and electron-molecule interactions. Beta decays that occur near the ion detector have a chance of triggering the ion detector as the electric potential is not sufficient to turn them around. The rate can be estimated using the beta spectrum and electrical potential configuration.

Additionally secondary electrons produced by ion impact on the detector give a characteristic full energy peak at a fixed time after ion incidence. These events are useful in determining the timing resolution. We will look for this effect in ion-detector-singles-triggered data because the standard coincidence trigger requires the beta detector signal to arrive before the ion detector.

4.2.2 Coincidence events

The detection of an ion signal within 0.4 μs of the beta signal is the signature of the events of interest. The beta signals are treated as the start of the clock because while the electrons are emitted in all directions, their low mass means they are quickly oriented along the field lines and accelerated toward the beta detector end of the

chamber. The relative timing of the events varies between 0 and ~ 0.4 μs based on the location of the decay within the chamber and the orientation of the daughter recoil momentum. The orientation of the daughter momentum mildly distorts the distribution along the time axis but the timing error is dominated by our timing resolution.

We use the ion energy versus ion time of flight (E-TOF) plots as the basis for extracting branching ratios. The different mass states reveal themselves as separate groups, following parabolas in E-TOF space. Hard cuts on the energy fiducialize the volume and assure good efficiency for detection of both the beta and ion.

Moving the detector

As a result of ion species-dependent momentum the acceptance of events varies with the radius of the detector. The detector is not large enough to contain all ion events. Thus we scan the detector across the diameter of the chamber to sample the momentum distribution and build a profile of the branching ratio with respect to daughter momentum. We can correct the spectra for geometric acceptance factors that decrease with distance from the central axis of the chamber.

4.2.3 Calibration

Americium-241 spectra provide energy calibration peaks for converting ADC bins. The peaks at 59.5 keV and 26 keV reasonably span the most interesting energy regime for the TRIMS experiment. The energy calibration is repeated every few days to minimize errors due to drifts in the electronics performance. The energy calibration runs consist of data taken with a sealed Am-241 γ-source (NPL041, 100 μCi in 12/1969) placed outside the aluminum housing near the central z-value of the chamber.

A typical Am-241 calibration spectrum is shown in Fig. 4.1. This spectrum was taken with detector 118088, the ion-detector preamp and channel-0 of the digitizer. The fit peak position is 36.2$\pm$1.3 bits for the 59.5 keV peak. The lower energy portion

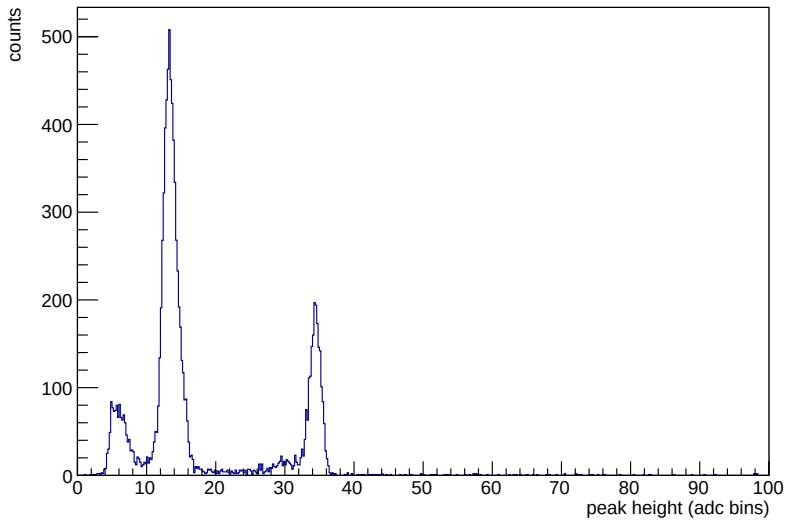

Figure 4.1: Typical calibration spectrum taken with an Am-241 source, detector 118088 and the ion-detector preamplifier and filtered with a 8 μs peaking time.

of the spectrum is contaminated with a large number of x-rays from the intermediate material which prevent the use of the lower Am-241 peaks for calibration. We plan to improve the energy calibration using additional radioactive sources (e.g. Cd-109).

4.2.4 Krypton calibration

A krypton-83m calibration with conversion electrons will provide a proof of principle for the TRIMS apparatus. The conversion electrons provide both singles and coincidence triggers. The krypton charge states provide a test of the ability to separate charge-to-mass states in the TRIMS setup. The calibration plan and source are described in detail in Chapter 5.

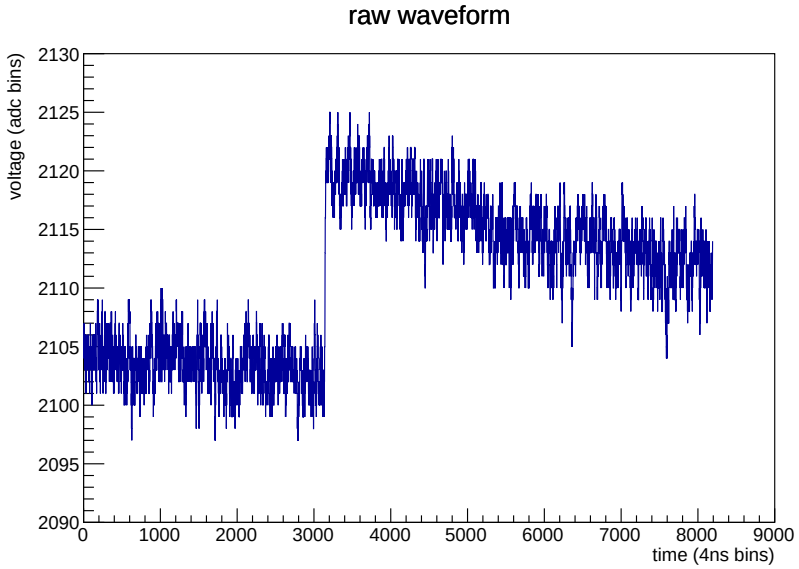

Figure 4.2: Sample pulser signal. On the x-axis, each bin is 4 ns. On the y-axis, each adc bin is 0.49 mV.

4.3 Waveform Filtering

A trapezoidal filter algorithm [154] determines the energy and timing of the signals. The filter uses an adjustable integration time and a rise-time gap. The optimized filter parameters balance high-frequency noise and leakage current contributions. The PIPS leakage current of up to 10 nA necessitates AC-coupling and pushes the optimal shaping time to shorter values.

Figure 4.2 shows a sample waveform obained with a pulser set to mimic the input signals from a PIPS detector. Figure 4.3 shows the first shaped pulse created by the trapezoidal filter; the shaped pulse determines the peak height of signal pulse. Figure 4.4 shows the second shaped pulse created by two consecutive trapezoidal filters; the second shaped pulse determines the arrival time of the signal pulse.

Fig. 4.5 shows the pulser linewidth (standard deviation) as a function of filter peaking time for the pulser runs with electronics connected to a biased detector and

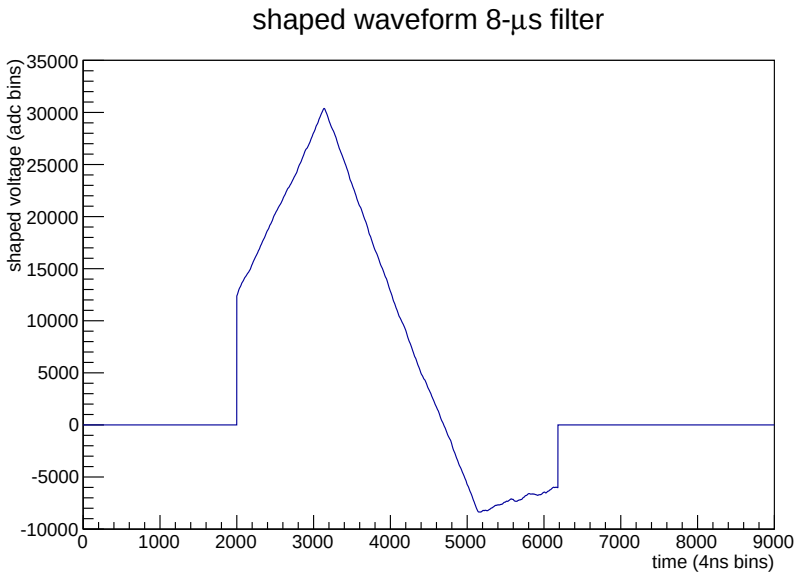

Figure 4.3: Sample pulser signal shaped with a trapezoidal filter.

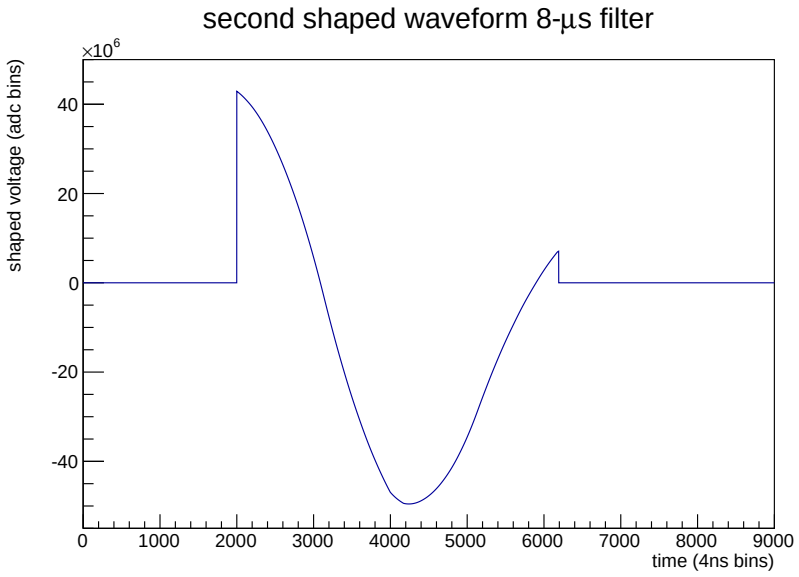

Figure 4.4: Sample pulser signal shaped with consecutive trapezoidal filters

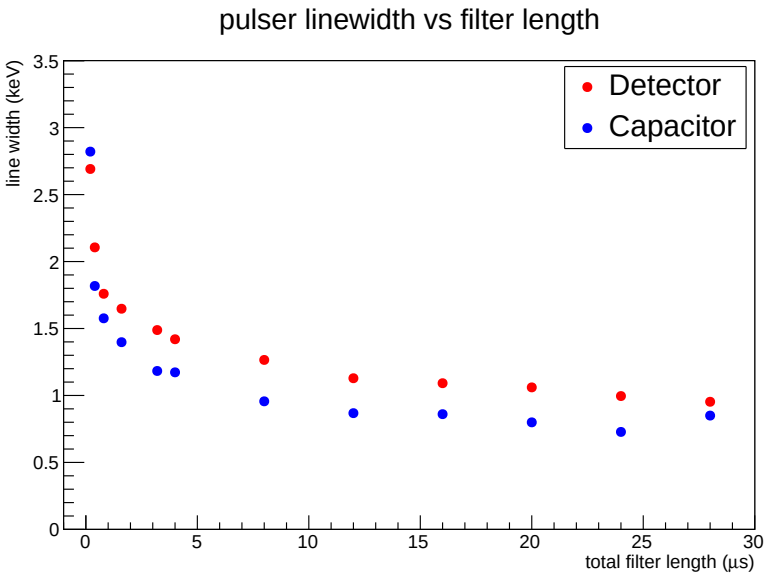

Figure 4.5: Linewidth (standard deviation) of pulser signal as a function of filter peaking time. The red dots are from a run with the detector connected to the preamp input and the blue dots are for a run with a 43-pF capacitor at the input. The same 5-second run was used for each waveform setting.

electronics connected to an equivalent[1] 43-pF capacitor [155]. Comparison of the standard deviation of the pulser line shows that marginal gains are achieved for shaping times above 4 µs. At higher peaking times the filter loses performance due to the limited acquisition window. For very long traces the linewidth should rise from the leakage current noise contribution.

4.3.1 Peak height

The height of the signal peak determines the energy of the incident radiation. The height in ADC bins is determined by the trapezoidal filter output. The gap length

[1]Canberra does not publish information on the capacitance of their detectors. This information was obtained courtesy of M. Morelle at Canberra.

of the filter can be used to avoid incorporating the rise time of the pulses in the calculation of the peak height. In the future pole-zero correction will be applied to account for the RC discharge of the signal following the voltage spike. For short shaping times, the pole zero correction is small but can improve the performance of the filter for longer shaping times. We plan to implement the pole-zero correction in the waveform filter.

4.3.2 Timing

The timing of the signal is taken from the zero crossing of the second shaped waveform. The global arrival time of the pulse requires correction due to the filter parameters but the relative timing only requires the same definition be used across channels. The four channels of the DT5720 share a single clock, allowing direct comparison of sample numbers for relative timing values that are more precise than the 10-ns trigger clock tick. Figure 4.6 shows the timing resolution of the signal fanned out to two preamplifiers. The resolution improves with shorter filters. Figure 4.7, however, shows that the filter becomes more sensitive to high frequency noise and the efficiency goes down with filters that are too short. We select a timing filter of length 100 ns to balance resolution and efficiency.

4.3.3 Linearity

We tested the linearity of the electronics with an Agilent 33220A pulser with linearity specification <0.1% of peak output. We vary the amplitude of test signals injected into the preamplifier and map the peak position. The pulser amplitude varied between 1 mV and 100 mV with higher density at the lower settings. Figure 4.8 shows the spectrum obtained from 5-second runs at each voltage setting. Figure 4.9 and Fig. 4.10 show the Gaussian fit line position for each voltage setting for copper and fiber optic readout, respectively.

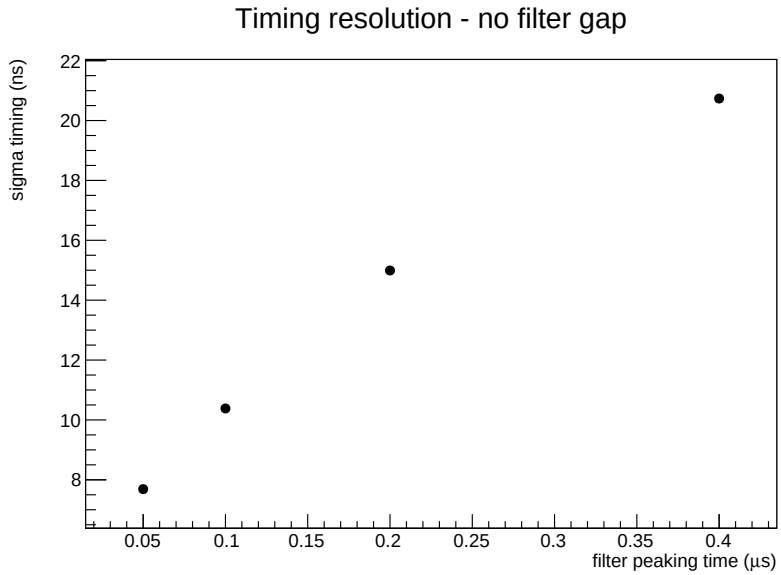

Figure 4.6: Timing resolution (Gaussian width) for pulser signal fanned out to two preamplifiers and digitizer channels.

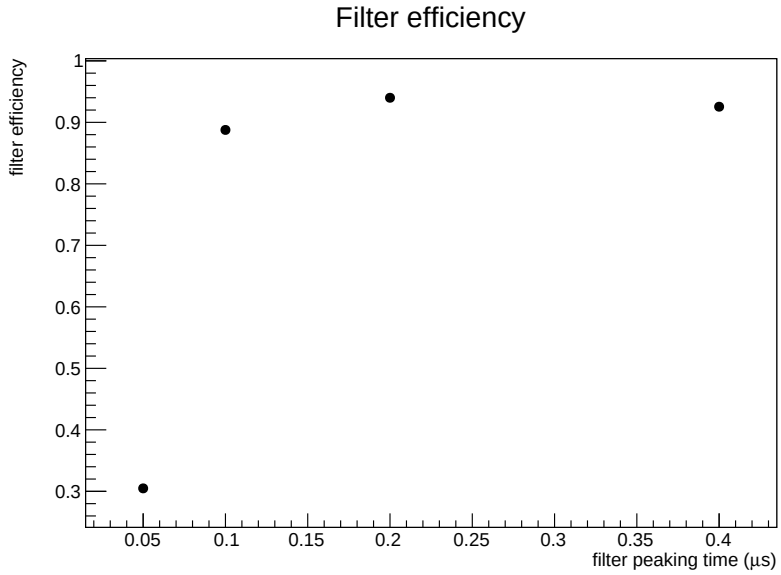

Figure 4.7: Timing filter efficiency: normalization of the Gaussian fit around $\Delta t = 0$ divided by the total number of events in the run as a function of filter peaking time.

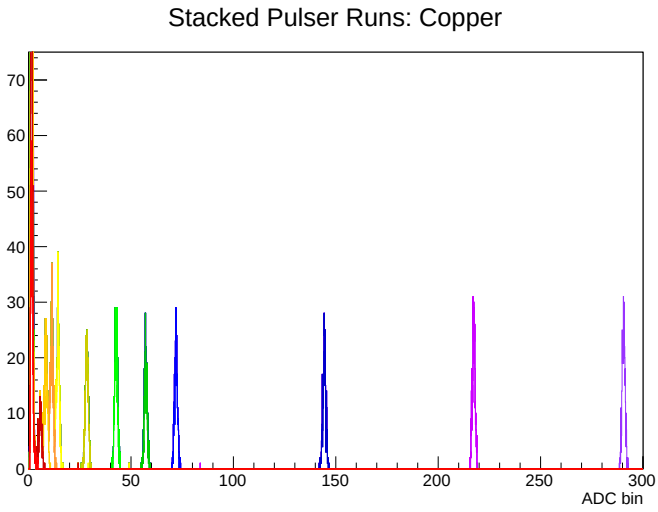

Figure 4.8: Energy spectrum created by 5-second runs at voltage settings between 1 mV (red) and 100 mV (purple). This run used detector 98344 and the ion detector preamplifier box.

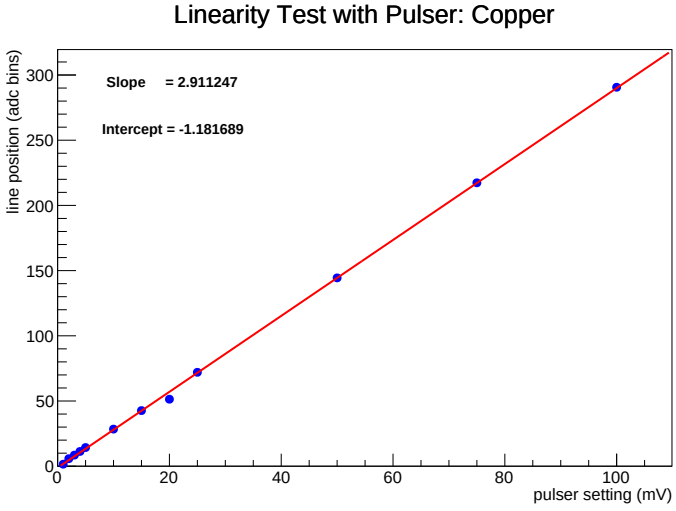

Figure 4.9: Linearity test of copper signal showing linear behavior. Line positions are from Gaussian fits to the pulser signal position for a set of pulser settings ranging from 1 mV (red, unresolved) to 100 mV (purple).

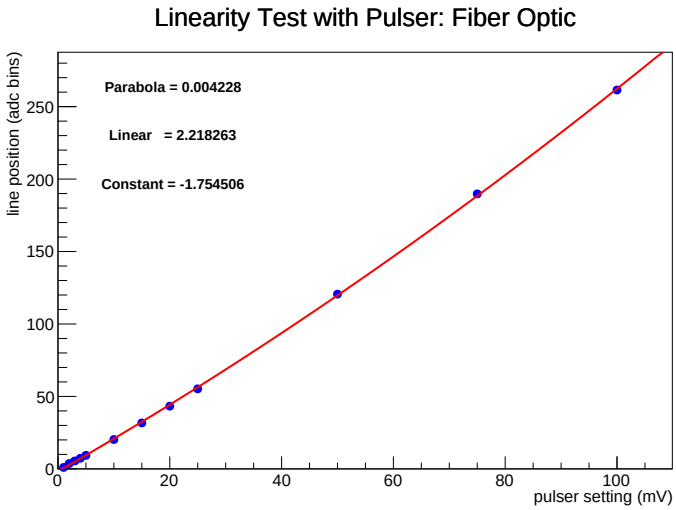

Figure 4.10: Linearity test of fiber optic signal response showing quadratic behavior. Line positions are taken from Gaussian fits to the pulser signal position for a set of pulser settings ranging from 1 mV (red, unresolved) to 100 mV (purple).

4.3.4 Pileup

Pileup occurs when two or more signals fall within the waveform window. The TRIMSWaveformFilter does not currently identify or adjust for pileup events. Depending on the relative positions and heights of the peaks the event can be reconstructed correctly or incorrectly. In association with returning the incorrect pulse height (energy) the waveform filter can return the wrong timing information as it is drawn from the zero crossing of the second shaped pulse. The double-hit on timing and energy is troublesome for creating energy vs time of flight spectra. The impact of pileup on the TRIMS measurement is controlled by keeping the pressure very low. A short waveform filter is planned that will identify events with multiple peaks above the noise level and flag them as pile-up. The analysis will reject pileup events because a correct time of flight cannot be identified.

A sample pile-up event from an Am-241 run is shown in Fig. 4.11 and the shaped

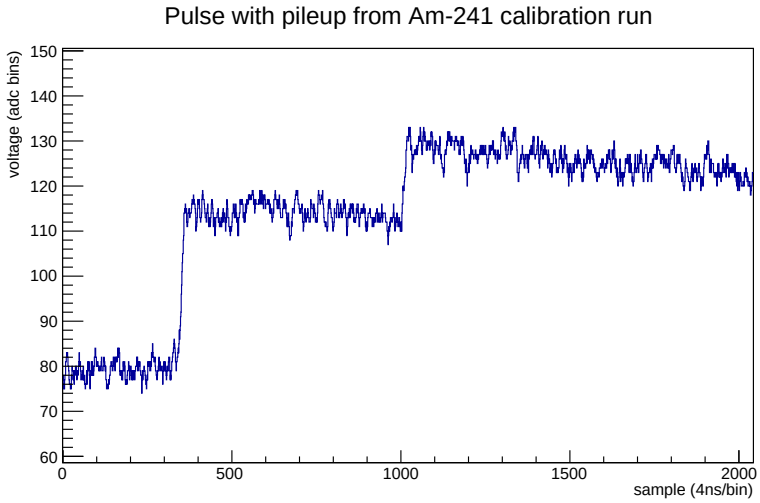

Figure 4.11: Pileup event from Am-241 calibration run taken during commissioning of the digitizer.

waveform is shown in Fig. 4.12.

4.4 Energy-vs-time-of-flight spectra

4.5 Branching Ratio Analysis

The TRIMS branching ratio analysis is performed on the energy-vs-time-of-flight spectra. The cuts are generated by looking at ion energy binned data and fitting the peaks that correspond to mass-3 and mass-6 events. The times of flight associated with the mass-3 and mass-6 peaks are averaged to get optimal cut at that energy. A parabolic fit of the optimal cut values determines the actual cut parameters. The same approach is used to determine the mass-1 cut based on the location of the mass-1 and mass-3 peaks.

We histogram the data to produce energy-vs-time-of-flight spectra with 1-keV energy bins and 10-ns time bins. For each ion energy bin, the time-of-flight profile histogram is produced, revealing a multipeak structure corresponding to the different

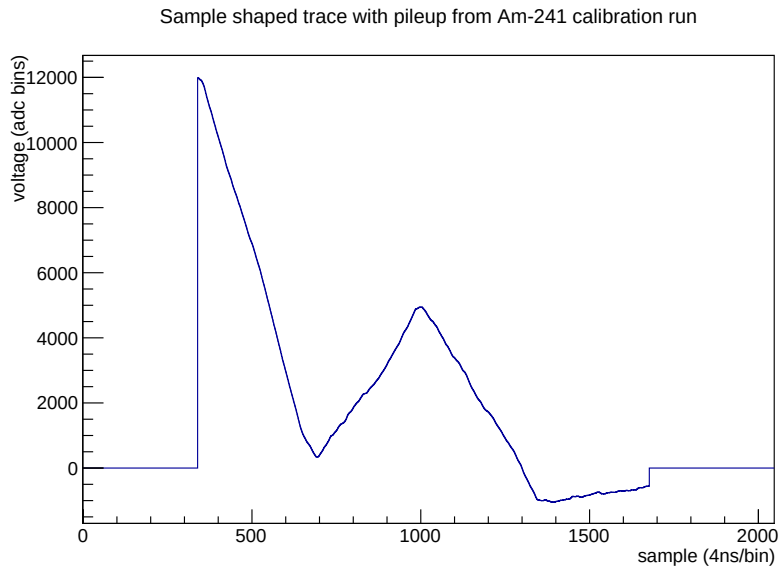

Figure 4.12: Sample of the pileup trace from Fig. 4.11 shaped with a shorter than usual peaking time to reveal the double peak structure. Peaking time of 0.7 μs and gap of 80 ns were used compared to the normal 4 μs peaking time.

ions produced in the decays as shown in Fig. 4.13. The cut between the mass-3 and mass-6 peaks is determined by a cut-finding algorithm.

The cut algorithm determines the locations of the mass-3 and mass-6 peaks with a custom peak finding algorithm. The first peak is identified as the highest bin in the histogram. The 8 bins around the peak are fit to a Gaussian and subtracted from the histogram. The second peak is identified as the highest bin in the peak-subtracted histogram. The primitive cut is taken as the average of the two peaks. The primitive cuts are fit to a parabola to mimic the shape of the branches in the histogram. The resulting parabola defines the cut between mass-6 and mass-3 events.

A similar procedure determines the cut between mass-1 and mass-3. The mass-1 peak of the double-subtracted (mass-3 and mass-6) histogram is found under the restriction that it be at least 5 bins below the mass-3 peak. The peaks are averaged with a weight of 2 for the proton peak and 1 for the mass-3 peak. The parabolic fit of the weighted averages determines the proton identification cut.

With both parabolic cuts defined the data are sorted into three regions: A (mass-1 like), B (mass-3 like) and C (mass-6 like) events. The mass-4 events are split between the B and C samples. The HT background mass-3 and mass-4 events are removed statistically by subtracting the results of the two samples weighted by ratio of events in the A sample. Thus we can write the branching ratio $\mathcal{B}$ in a parameterization that is only dependent on observed quantities:

$$\mathcal{B}(\mathrm{T}_2 \rightarrow {}^3\mathrm{HeT}^+ + \beta^-) \;=\; \frac{N_{\mathrm{C1}} - \frac{N_{\mathrm{A1}}}{N_{\mathrm{A2}}}(N_{\mathrm{C2}})}{N_{\mathrm{B1}} + N_{\mathrm{C1}} - \frac{N_{\mathrm{A1}}}{N_{\mathrm{A2}}}(N_{\mathrm{B2}} + N_{\mathrm{C2}})}. \tag{4.1}$$

The A, B, C parametrization has a clear statistical interpretation with Poissonian, independent errors on each N_i. The lack of dependence on the cuts illustrates the power of the A, B, C parametrization. The alternative parameterization in terms of the mass states has a clear interpretation of the mass-4 cancellation, however, the mass-4 contribution to each region is highly dependent on the cuts applied. The

mass-6 and mass-1 states are relatively easy to separate from the mass-3 states. The mass-4 contribution to the B and C categories is the troublesome factor. Given the separation of the high and low mass states the relationships to A, B and C are given by:

$$N_{\mathrm{A}} = N_{\mathrm{mass1}} \tag{4.2}$$

$$N_{\mathrm{B}} = N_{\mathrm{mass3}} + (1 - f_{\mathrm{mass4,C}})N_{\mathrm{mass4}} \tag{4.3}$$

$$N_{\mathrm{C}} = N_{\mathrm{mass6}} + f_{\mathrm{mass4,C}}N_{\mathrm{mass4}}, \tag{4.4}$$

where the $f_{\mathrm{mass4,C}}$ factor quantifies how much of the mass-4 peak falls in the C window. In reality this term has energy dependence because of the different energy deposition characteristics of the ion species. With work to characterize the line shapes this factor could potentially be measured. The method we use, however, does not rely on knowledge of the shape, instead canceling the contribution to first order by comparing two datasets with different levels of contamination. The cancellation occurs because any mass-4 events contribute to the overall normalization (B+C) in addition to contributing to the C branch. With these events removed the only remaining contribution is due to statistical fluctuations around zero amplitude in the mass-4 branch. Such statistical error is captured in the statistical errors on the B and C counts as they are propagated through to the error on the branching ratio.

4.6 TRIMS run plan

The general TRIMS run plan consists of taking coincidence data at a variety of ion-detector positions. Using the linear translation stage we set the ion detector at a specific location across the diameter of the chamber and record data when the ion detector triggers within 0.5 μs after the beta detector trigger. The data from the central region has the highest efficiency and thus the lowest error bars. Data taken with the ion detector at large radius has the lowest probability and the highest

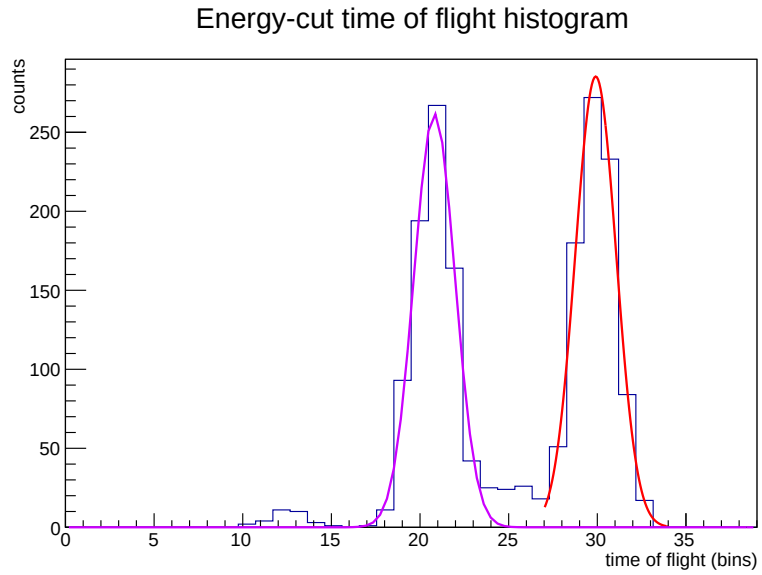

Figure 4.13: Simulated energy-cut time-of-flight histogram (nominal parameters) for a 1-keV, 10-ns bin widths. The peak structures reveal the different ion species. The red line is the fit to the mass-6 peak and the purple line is the fit to the mass-3 peak.

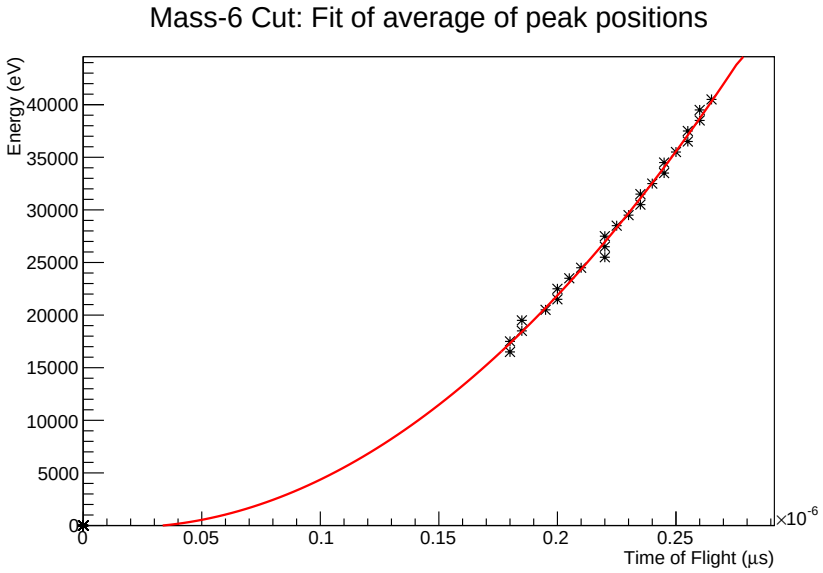

Figure 4.14: Parabolic fit to average of mass-3 and mass-6 peak positions. Fit represents the cut used to determine the number of mass-6 events.

geometric corrections. We scan across the center of the chamber and compare data taken on each side of what is believed to be the center of the chamber. This allows us to look for any field variations that may affect sensitivity.

The length of runs at each detector location is set by the trigger rate and will be decided at run time. We plan to acquire order 10^9 events in order to achieve reasonable statistical uncertainty on the branching ratio.

Chapter 5

KRYPTON CALIBRATION

A krypton calibration for the TRIMS experiment acts as a proof of principle. The krypton-83m isomer has a conversion factor over 2000, strongly favoring the emission of an electron. The state has a half-life of 1.8 hours and is itself the daughter of rubidium-83. The K-conversion electron energies is close to the tritium beta decay endpoint, making it a good calibration line for tritium beta decay experiments.

In addition to the conversion electron the decay produces a krypton-83 ion that can be multiply ionized via an Auger cascade. The combination of an electron line and a spectru, of ions with different charge-to-mass ratio allows a convenient proof of principle for the time-of-flight spectrometer because it is short-lived and non-contaminating.

5.1 Krypton decay scheme

The ^{83m}Kr metastable isomer of interest has a 1.8 hr half-life, making it an ideal calibration source that will not contaminate the system. The isomer of interest is efficiently fed by the beta decay of ^{83}Rb, an isotope with an 86.2 day half-life. Fig. 5.1 shows the ^{83m}Kr decay scheme. The ^{83}Rb decay scheme is signficiantly more complicated with a large number of gamma rays feeding the isomer of interest as well as the ground state as shown in fig. 5.2. The large number of gamma rays following the rubidium decay requires the source be shielded and installed away from the detectors. Both decay schemes are taken from the National Nuclear Data Science references [5, 6].

The main line of interest in tritium experiment is the 17.8 keV K-shell conversion electron. This line is close to the tritium beta endpoint and thus can check the

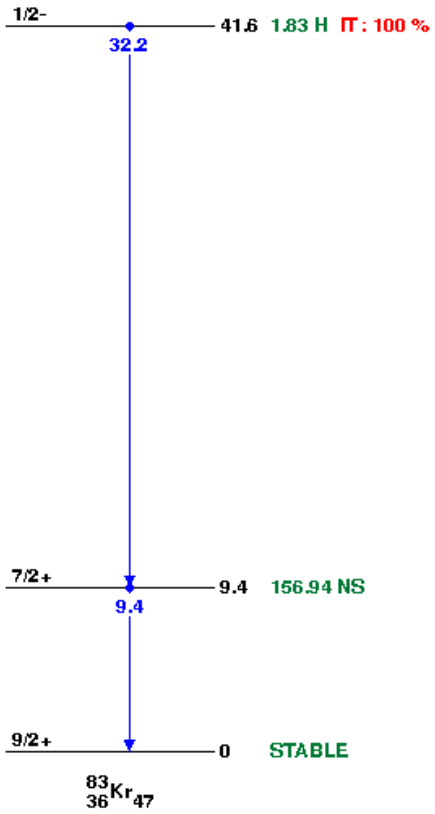

Figure 5.1: ^{83m}Kr decay scheme from NNDC [5]

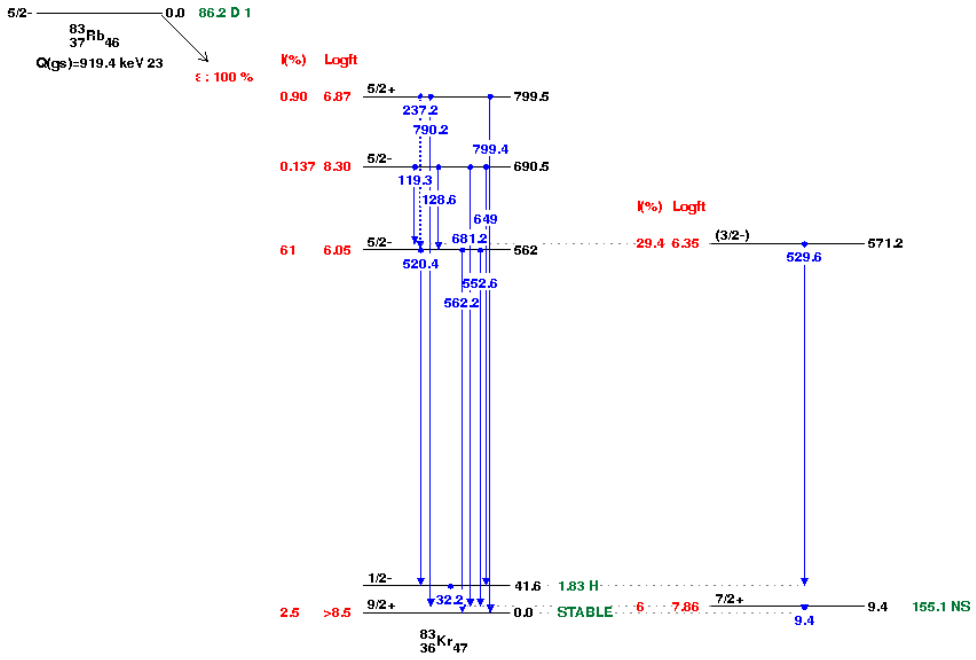

Figure 5.2: ^{83}Rb decay scheme from NNDC [6]

response at energies near the endpoint. In the TRIMS apparatus we do not distinguish between the different electron lines during online running. The high number of shake-off and shake-up electrons that occur following the internal conversion provide some overlap betwen the states in the beta-energy vs. time of flight plane. There are, however, regions of the phase space where the conversion energy is well defined. Table 5.1 shows the ENDSF data for electrons from the decay of ^{83m}Kr.

5.2 Krypton in TRIMS

Although we designed the Tritium Recoil-Ion Mass Spectrometer (TRIMS) time-of-flight spectrometer to measure the *m*ass of ions produced in a decay the same principle works on the *c*harge state of the ions. We will use the decay of ^{83m}Kr to demonstrate functionality of the spectrometer prior to introducing tritium to the

Table 5.1: Electrons from ^{83m}Kr decay taken from the NNDC Nuclear Data Sheets [5]

Type	**Energy (keV)**	**Intensity (%)**
Auger L	1.5	168.4
CE L	7.4847	80.0
CE M	9.1177	12.9
CE N	9.3817	1.26
Auger K	10.8	8.62
CE K	17.8260	24.8
CE L	30.2306	63.7
CE M	31.8636	10.66
CE N	32.1276	0.782

spectrometer. The decay of ^{83m}Kr produces a 17.8-keV conversion electron and a ^{83}Kr ion. Following the emission of the conversion electron shakeoff from Auger cascades results in a highly charged krypton ions at appreciable rates [156]. The timing between the prompt conversion electron and the ion identifies the charge state of the ion. While TRIMS is nominally designed to measure the mass of singly charged ions for the ^{83m}Kr calibration the spectrometer will measure the charge state of highly-ionized atoms with fixed mass.

A radionuclide generator is necessary because the 1.8-hour ^{83m}Kr half life is too short for a pure source to remain useful over the lifetime of an experiment. Taking advantage of the 86.2 day half-life of ^{83}Rb [157] we employ a ^{83}Rb/^{83m}Kr radionculide generator. The chemical reactivity of rubidium traps the parent nuclei on the source walls, preventing it from contaminating our vacuum system. The decay of ^{83}Rb creates the inert ^{83m}Kr daughter that readily diffuses through the vacuum system, entering the spectrometer where we can measure the decay products.

To achieve reasonable statistics an activity of a few microcurie is required. In ad-

dition to producing the isotope of interest, the source must release the krypton gas so it can diffuse through the system and decay in the chamber. We measure the emanation of the krypton from the walls in order to estimate the effective source activity for gaseous measurements in the TRIMS apparatus. As described in sections 5.3-5.7 we produced an adequate source on the CENPA Tandem Van de Graaff with a measured effective activity of 12 μCi. The activity is sufficient for the TRIMS calibration needs.

5.2.1 TRIMS Hardware considerations

The krypton calibration presents its own set of challenges to the TRIMS hardware. Specifically the detection efficiency and the electronics chain dynamic range are vital to the success of the calibration campaign. Below we discuss major aspects of the hardware that differ from the standard TRIMS setup as described in section 3.5.

Detector

The krypton ion has significant mass and for fixed charge the penetration into the detector is appreciably decreased over the lighter isotopes of interest in TRIMS. This effect is partially compensated by the existence of high charge states (higher than 10 e) due to the additional energy gained over the same potential drop.

High voltage

We vary the high voltage settings to demonstrate an understanding of multiple aspects of the spectrum. At the typical high voltage settings for TRIMS (50 kV) the singly charged ion parabola defines a cutoff below which ^{83m}Kr decays do not appear. At this setting, however, the highly-charged ions are accelerated to extremely high energies that may saturate the preamplifier fiber optic driver and thus would not be observed in our system. The fiber-optic saturates at 1 V. The typical Am-241 calculation of 1.7 keV per adc bin and the bin width of 0.49 mV, we find the saturation point occurs

is 3.5 MeV of deposited energy. This means that even for charge states up to 10+ we do not expect to saturate the fiber-optic.

5.2.2 Expected spectra

The expected krypton spectrum is drawn from the characteristics of the decay. Runs without HV will show the standard krypton spectrum including the 17.8-keV and 30.2-keV peaks. The 9.1 keV peak, while below threshold, can be seen in coincidence with the 17.8 keV peak when triggering on the higher energy pulse. The 157-ns lifetime means coincidence within the same detector results in pileup that fills the regions between the peaks while coincidences between the two detectors can be fully reconstructed. We also use the two-electron coincidence rate to align the detector axis with the magnetic axis.

For runs with high voltage, the singles electron spectrum should have a flat regions extended between $E_{\text{conversion}}$ and $\text{HV}_{max} - E_{\text{conversion}}$ corresponding to each conversion line. Thus we expect to see steps in the spectrum at each of the conversion energies and at the conversion energies plus the high voltage. The ion energy depends on the charge-state distribution of the daughter ions. Shakeup and shakeoff play major roles in the $^{83\text{m}}$Kr decay and the charge distribution is not necessarily straightforward. D. Decman and W. Stoefflˆs measurements of the 9.4 keV transition indicate the most probable charge-state is 5+ and that states up to 10+ are appreciably populated [156]. In the TRIMS setup the extra soft electrons have some probability of being measured in addition to the original electron.

5.3 Krypton source

The krypton source was produced indirectly by creating a rubidium-83 source that beta decays to the isomer of interest with an 86.2-day half-life [157]. The rubidium was created via the ^{nat}Kr(p,xn)^{83}Rb reaction with protons from the CENPA Tandem Van de Graaff accelerator. The ^{nat}Kr(p,xn)^{84}Rb reaction produces undesireable radi-

ation and increases the base pressure. The presence of rubidium-84 results in excess shielding requiremetns for the same krypton-83m source activity.

The beam parameters were optimized based on the rubidium production cross sections measured by Kovacs et al [7] and shown in figure 5.3 and figure 5.4. A beam energy above 15 MeV is required to significantly reduce the activation of rubidium-84 and beam energy of 20 MeV is preferred. Given the limitations of the CENPA accelerator a beam energy of 17.5 MeV was selected.

5.3.1 Gas cell design

A custom gas cell was designed based on previous krypton activations performed by Nora Boyd, Noah Oblath and Brent VanDevender. Many updates were made to the old design, the most important of which was a novel window sealing scheme using crushed aluminum wire. The new design uses all metal seals in the main body of the gas cell. An elastomer sealed valve is used to isolate the window from the beamline in case of window failure.

We pumped the gas cell with a diaphragm pump to low vacuum and backfilled with 1 atmosphere of high purity natural krypton. The krypton pressure was monitored using a compound mechanical pressure gauge (-30 inHg to 30 psig) attached to the fill line.

The range of 17.5-MeV protons in 1 bar of krypton is roughly 1.6 m, infeasibly long for a source cell dimension. The range of the proton beam in aluminum is 1/16 inch allowing high purity aluminum to be used as a beam stop. We used a 5 inch 2.75-inch CF to miniCF reducing tee with a high purity (99.999%) aluminum plug installed on the back flange.

5.3.2 Activation

A 17.5-MeV proton, $\sim$ 10 μA beam from the CENPA tandem was focused on the krypton cell for an activation time of 9 hours and integrated beam current of 0.32 C.

The beam current should produce an activity of 0.69 mCi. The activity was measured using a high-purity germanium detector to collect the gamma rays. In estimating the activity of the source from the spectrum we correct for the live time and efficiency of the detector based on previous measurements by A. García and his students.

The signature of rubidium-83 is a triplet of gamma lines at 520 keV, 530 keV and 553 keV [157] with combined intensity of 90.3%. The gamma lines are close to the 511 keV annihilation peak which can be used to quickly identify the region of interest. The lines are fit to Gaussian peaks. The relative normalizations of the peaks are compared to the values from the National Nuclear Data Center [6]. The gamma yields were corrected for the intensity, the solid angle and attenuation caused by material between the source and germanium crystal. Section 5.4 discusses the activation and the measured spectrum. The measured activity was 0.68 mCi.

5.4 Source Production

We produce a ^{83}Rb/^{83m}Kr radionuclide generator via the ^{nat}Kr(p,xn)^{83}Rb reaction. Unfortunately ^{nat}Kr(p,xn) reactions also produce other isotopes of rubidium and we have to balance the production of the desired isotope with that of the undesired isotopes. Kovacs et al. measured the production cross sections for various rubidium isotopes in proton induced reactions on natural krypton [7]. Figures 5.3 and 5.4 show the Kovacs data for ^{83}Rb and ^{84}Rb production cross sections as a function of beam. The ^{81}Rb and ^{82}Rb cross sections are several orders of magnitude smaller than the cross section for ^{83}Rb production and are flat over the energies measured. Table 5.2 shows the half-lives of the rubidium isotopes produced in ^{nat}Kr(p,xn) reactions.

We can minimize the production of the undesired isotopes by tuning the proton beam energy. At 17.5 MeV the ^{81}Rb and ^{82}Rb production cross sections are two orders of magnitude lower than that of ^{83}Rb. The ^{84}Rb cross section, however, is only an order of magnitude smaller and slightly higher beam energies would be preferred to minimize ^{84}Rb production. The CENPA tandem Van de Graaff can be stably operated

Table 5.2: Half-lives of rubidium istopes produced in ^{nat}Kr(p,xn) reactions. Values taken from reference [6]

Isotope	**Energy Level (MeV)**	**Jπ**	**Half-life (s)**
^{81}Rb	0.0	3/2-	4.572 h
	0.0863	9/2+	30.5 m
^{82}Rb	0.0	1+	1.2575 m
	0.069	5-	6.472 h
^{83}Rb	0.0	5/2-	86.2 d
^{84}Rb	0.0	2-	32.82 d
	0.4636	6-	20.26 m
^{85}Rb	0.0	5/2-	Stable
^{86}Rb	0.0	2-	18.642 d
	0.5561	6-	1.017 m

at 17.5 MeV with a beam current of 10 uA on target. While beam energies up to 18 MeV are possible for short time periods the beam current is significantly reduced and frequent sparking compromises beam stability. To ensure stable operation over the activation we selected 17.5 MeV as the beam energy.

The other rubidium isotopes decay to stable isotopes of krypton (or strontium) which can increase the base pressure in the apparatus but do not increase the radioactivity of the gas that leaves the source cell. We examined the Table of Radioactive Isotopes (TORI) data on rudibium isotopes created in these reactions and determined that only ^{83}Rb, ^{84}Rb and ^{86}Rb have appreciable half-lives. The isotope ^{85}Rb has a stable nucleus while the half-lives of the ^{81}Rb, ^{82}Rb, ^{82m}Rb, ^{83m}Rb and ^{84m}Rb isotopes are less than seven hours. The isotope ^{86}Rb has a half-life of 18.6 days but decays to a stable isotope of strontium which will remain bound to the cell walls. The isotope ^{84}Rb has a 32.8 day half-life and remains appreciable in the source over the lifetime

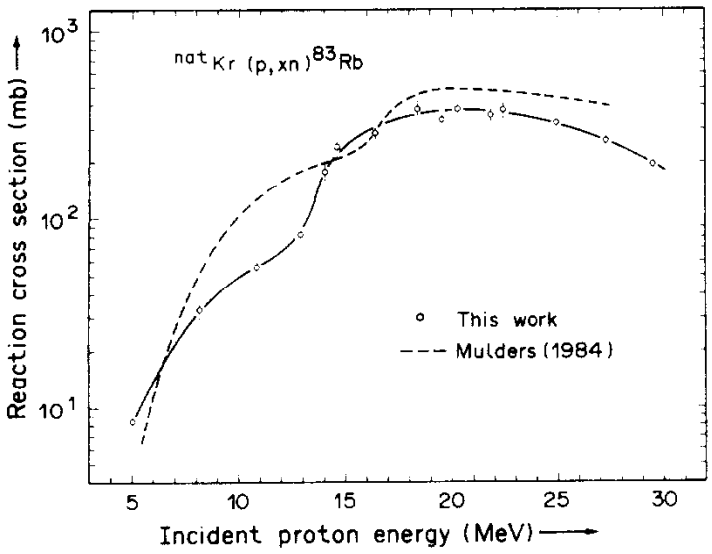

Figure 5.3: The ^{84}Rb production cross sections measured by Kovacs [7]

of the experiment. The ^{84}Rb decays to stable ^{84}Kr which will diffuse through the vacuum system. The decay also produces a high-intensity gamma ray at 886.2 keV, requiring additional lead shielding around the Rb/Kr source when high levels of ^{84}Rb are produced as well.

5.4.1 Activity calculation

The activation rate Y is given by the product of target density n, target cell length L, the cross section σ and proton fluence $N = I_{\text{beam}}$. The number of activated nuclei N_{nuc} is given by the integral of the activation rate as a function of time and is characterized in terms of the number of protons on target, N_{POT}. For nearly constant beam current this can be approximated as the product of activation rate and duration Δt of the activation.

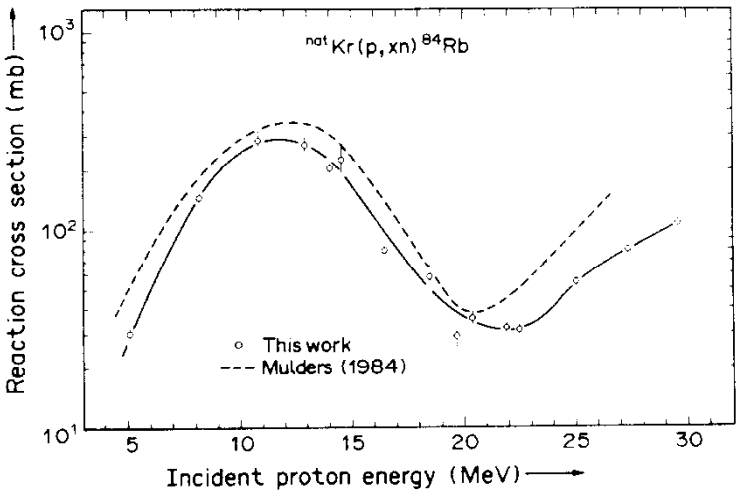

Figure 5.4: The ^{84}Rb production cross sections measured by Kovacs [7]

$$Y = nL\sigma N = nL\sigma \frac{I_{\text{beam}}}{e} \tag{5.1}$$

$$N_{\text{nuc}} = Y\Delta t = nL\sigma N_{\text{POT}} = nL\sigma \frac{I_{\text{beam}}}{e}\Delta t, \tag{5.2}$$

The activity of the source is given approximately by the quotient of the number of activated nuclei and the mean lifetime.

$$A \approx \frac{N_{\text{nuclei}}}{\tau} = \frac{Y\Delta t}{\tau} = \frac{nL\sigma \ln 2}{t_{\text{half}}} \frac{I_{\text{beam}}}{e}\Delta t \tag{5.3}$$

Solving for beam time as a function of activity yields

$$\Delta t = \frac{A}{nl\sigma} \frac{e}{I_{\text{beam}}} \frac{t_{\text{half}}}{\ln 2}. \tag{5.4}$$

We calculated the number density of one atmosphere of room temperature krypton ($2.68 \times 10^{29}\text{cm}^{-3}$) from the mass density and atomic weight.

The length of the chamber is that of the tee and entrance flange (14 cm). A longer chamber would increase activation for the same Δt but would be awkward to handle

and would require a larger lead housing after activation.

We extracted the ^{83}Rb production cross section of 370 millibarn from the Kovacs plot (See figure 5.3)[7]. We use the 86.2-day half-life for rubidium listed in the TORI [157]. We estimated approximately 15 hours of beam time was required to create a 1 mCi source with a typical beam current of 10 μA .

5.5 Cell design

The krypton gas cell operated with 0.33 psig of research-grade natural krypton gas providing a target. Protons entered the cell through a thin foil window installed on a double-faced flange. The main body of the cell consisted of a 2.75-inch/1.33-inch Conflat reducing tee. The cross arm connected to a valve used to pump/backfill the cell with natural krypton before activation and to extract the krypton after activation. The downbeam flange of the cell contained an aluminum beam-stop press fit into a blank Conflat flange. Upbeam of the cell a gate valve protected the foil after activation and sealed the vacuum system in case the foil breaks after activation. Figure 5.5 shows an Inventor model of the cell design. The parts of the source cell and their arrangement are described in greater detail below.

5.5.1 Entrance window

We developed a new procedure for making metal-sealed thin foil windows. We chose not to glue the foil in place because of our high-purity vacuum requirements and the desire for a seal that can be easily remade in case of damage to the foil. We chose aluminum wire because of concern over indium wire creep during activation. We punched 1.1-inch circular entrance window out of 0.0007-inch thick Reynolds 656 dead soft aluminum foil. A 1-in thick double-faced flange provided a base for the window. The 0.5-inch flange bore defined the acceptable beam trajectory and a machined 1.5-inch diameter, 0.4-inch deep step provided the sealing service. Eight 8-32x0.5-inch blind holes tapped into the step allow us to secure the foil with an

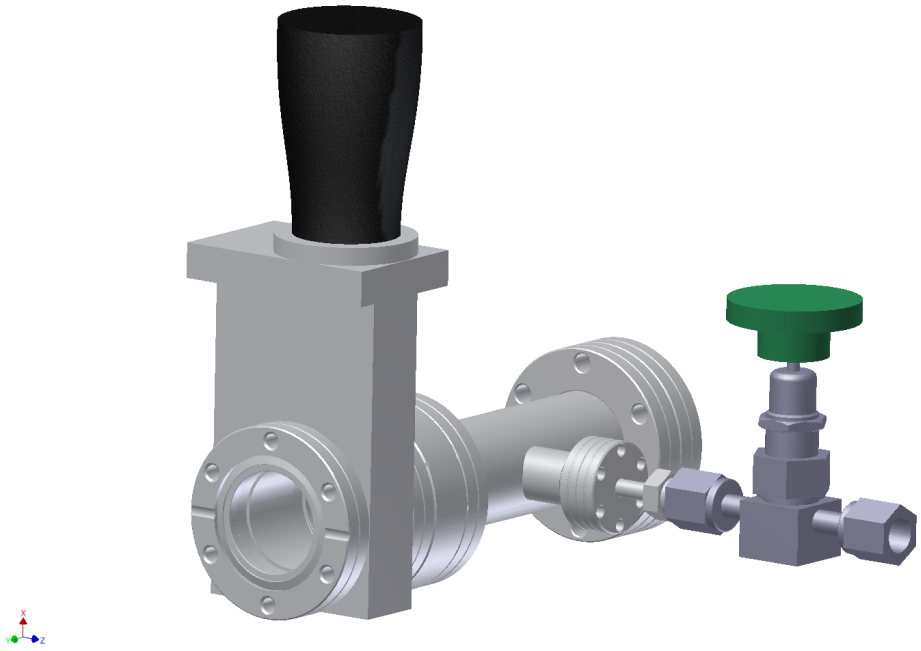

Figure 5.5: Inventor model of Krypton source cell

aluminum hold-down ring.

A gasket of 0.020-inch diameter deadsoft aluminum wire fusion welded to form a continuous ring sealed the spaces from each other. We made the gasket by carefully cutting the wire to the right circumference and applying aluminum brazing flux (Superior Flux & Mfg Co, No. 20) before quickly bringing the ends through the flame of a small acetylene torch. The flux prevented oxidation while the wire ends melted and joined. After removing them from the flame we tested the continuity and visually checked the pieces for any cracking. We cleaned the gasket in isopropyl alcohol to remove any excess flux.

The finished aluminum gasket was placed on the step in the flange with the foil set on top of the wire. The hold-down ring was set on top of the foil and the bolts were installed finger tight. As the bolts were tightened we measured the crush of the

gasket using a depth gauge at several points around the flange. A depth reading of 0.01-inches produced a leak-tight seal at the 1.0×10^{-12} mbar·L/s level.

Active cooling of the window was not necessary because calculations of the beam current heating of the foil showed very small temperature rises caused by energy loss in the foil. In the conservative limit where conductivity through the foil is the only cooling mechanism a 2-mm wide, 17.5-MeV, 15-μA beam raises the temperature in the center of the foil 124 K. The hold-down ring provides clamped connection with good thermal conductivity to the outside world. Thus the temperature differential from flange to center of foil is below 200 kelvin, well below the melting point of aluminum. Hence no external cooling is required for the window during activation.

5.5.2 Beam stop

We used an aluminum beam stop installed on the downbeam side of the cell. While the ideal beamstop for a gas cell is the target gas itself, the range of 17.8 MeV protons in one atmosphere of room-temperature krypton gas is 1.6 m [158]. A chamber of that length is difficult to handle and shield during use. Thus, the TRIMS source comprises a manageable 5-inch chamber with a high-purity (99.999

The range of 17.5-MeV protons in aluminum is 0.45 g/cm^2[158], or roughly 1/16 of an inch. The beam stop consists of a 0.125-in thick, 1.5-in OD aluminum disk press fit into a recess into the inside of 2.75-inch Conflat flange installed on the end of the gas cell. We use a tight press fit to ensure thermal contact between the flange and beamstop.

The previous CENPA activation used an additional aluminum liner in the body of the tee. This was added for the second Project 8 activation after an early attempt at activation failed to make krypton and activated the cell walls. Investigation revealed that this was the result of the beam impinging on the entrance flange rather than the window. For standard operation the scattering is nearly all forward and the sides do not see a large number of protons. Moreover the rubidium diffusion in aluminum

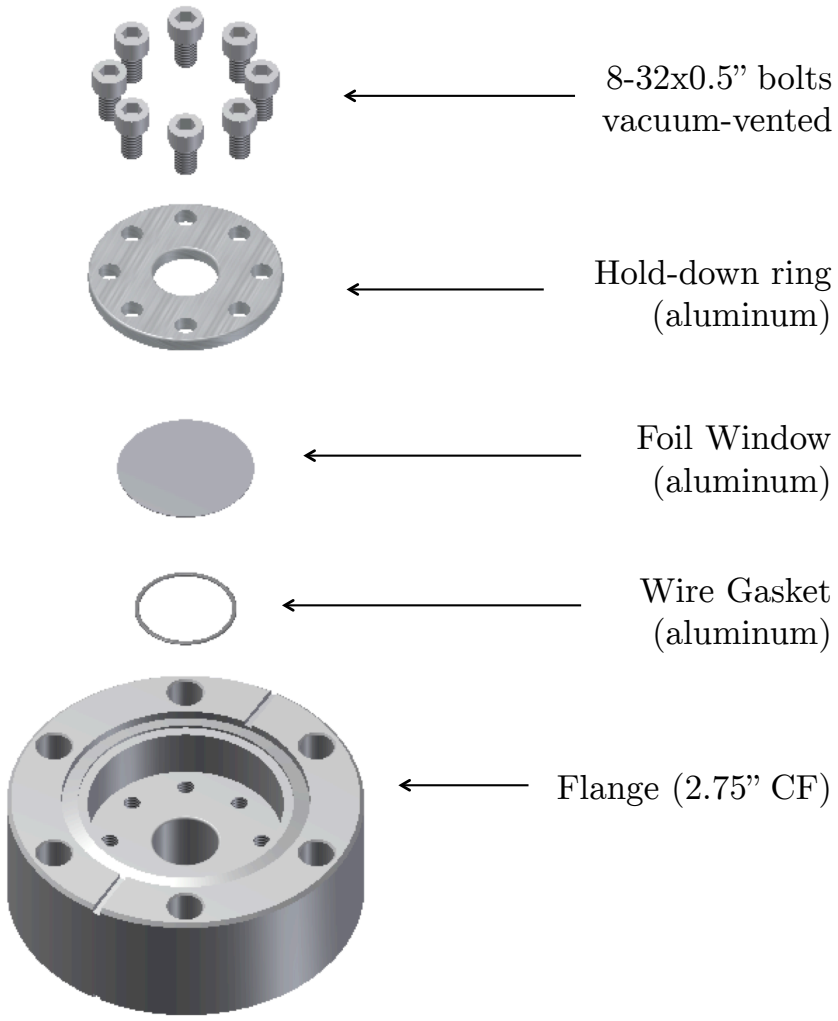

Figure 5.6: Cross-sectional view of entrance window assembly

is higher than that in stainless steel thus the use of aluminum should be minimized. The TRIMS version of the krypton cell does not contain an aluminum liner.

5.5.3 Cooling

The beamstop is actively cooled with water flowing through an oxygen-free high-conductivity (OFHC) copper cup bolted to the back flange of the cell. A printed circuit board placed between the cup and the flange electrically isolates the water line from the gas cell. While ideally the water would directly contact with the cell, electrical isolation is necessary to allow measurement of the beam current. A suitable electrically isolated water system does not exist, necessitating the thin circuit board which provides electrical isolation with sufficient thermal conductivity to cool the system. Other CENPA acclerator users employed this cooling device in previous setups with similar beam power.

5.5.4 Gate valve

A gate valve just upstream of the entrance flange ensures the system stayed sealed even if the foil were to break after activation. The gate valve is closed while under vacuum on the beamline, ensuring that the foil does not see the full 1-bar differential pressure when the remaining natural krypton is pumped from the system. This arrangment helps prevent foil failure and ensures the radioactive system remains sealed even if the foil breaks in the future.

The gate valve (Lesker SG0150MCVF) has a fluorocarbon bonnet/gate and is not compatible with the TRIMS vacuum standard which require all-metal seals. The previous version of an activation cell used by Project 8 had the gate valve downstream of the entrance flange. The logic for this arrangement is unclear as it causes some of the activated volume to be sealed off after activation. The gate valve has a fluorocarbon bonnet and gate and is not compatible with the TRIMS vacuum standard of all-metal seals. The valve sits upstream of the foil, making contamination an unlikely issue.

5.5.5 Beam & monitoring

The CENPA Direct Extraction Ion Source produces the proton beam and the CENPA tandem Van de Graaff accelerates the beam to 17.5 MeV. The target cell sits on the 30-degree right beam line, on the downbeam side of the 24-inch scattering chamber (in which no scatterer is installed during krypton runs).

A 0.25-inch defining collimator directly upbeam of the 24-inch chamber sets the angle of the beam cone. The ceramic housing electrically isolates the defining collimator from the beamline. A 0.25-inch cleanup collimator positioned just upstream of the cell prevents the beam from hitting the side of the window. The cleanup collimator consists of a blank copper gasket with a 0.25-inch bore. The gasket is in electrical contact with the surrounding section of beamline. The ceramic break attaches to the target cell electrically isolated the collimator from the target cell. A custom isolating flange made by PNNL upbeam electrically isolates the cleanup collimator from the rest of the beamline. We monitor the current on each collimator in realtime using the set of Keithley 485 picoammeters in the CENPA Control Room. Optimal run conditions have low beam current on the defining collimator, essentially zero current on the cleanup collimator and maximum current on the target cell.

We optically align the system using a mobile beamline telescope. Before installing the target cell we set the telescope on line with the collimators. For the activation run the endcap of the target cell was roughly 0.12 inches off line. We attribute the misalignment to the piston seal on the end of the 24-inch chamber. Given the beamline geometry the offsets up to 0.22 inches are acceptable because the cleanup collimator can effectively accommodate them without substantial beam loss.

We monitor the target cell current as a realtime accounting of the activity being produced and we integrate to estimate the total activity. A ceramic insulator in the beamline and a printed circuit board between the the water lines and the back flange electrically isolate the krypton cell from the beamline and environment. The electrical

isolation allows us to make an accurate current measurement using the Brookhaven Instruments 1000a current integrator in the CENPA Counting Room. A 25-MHz NPL scaler counts the output signals from the BIC to determine the total charge (number of protons) collected on target. From the number of protons on target we calculate the expected activity.

5.6 Activation Run

We scheduled one week of beam time June 9-13, 2014. The previous week we setup the beamline and finalized plans. We filled the target cell and aligned the beamline on Monday and Tuesday. We irradiated the target for 36 hours beginning Wednesday June 11 until the high-energy charging chain of the tandem broke, rendering the accelerator unuseable for some time. As we had collected over half of our planned activity we decided to end the run early and proceed with measuring the activity.

For the entire run the BIC scaler collected 15.8 million counts, corresponding to 1.98×10^{18} protons on target. For a cross section of 300 millibarn this corresponds to an activity of 0.56 mCi . For a cross section of 370 millibarn we calculated an activity of 0.69 mCi.

5.7 Source characterization

Immediately following activation we measured the activity of the source by γ-counting. This determines the ^{83}Rb activity of the source, presumably stuck to the surfaces of the chamberr, but does not determine whether the krypton will emanate from the walls following decay of the ^{83}Rb on the wall. In June 2015 we measured the electron spectrum of the gas emanating from the evacuated source. In this section we describe the source characterization measurements.

5.7.1 Measured γ Activity

We measured the activity of the source by taking gamma spectra with a high-purity germanium detector setup developed and maintained by Alejandro García. An Ortec GMX-55220, Ortec 257N preamplifier, Ortec 572 amplifier and Princeton Gamma Tech MCA8000 Multichannel Analyzer (MCA) comprise the heart of the setup. Princeton Gamma Tech QuantumMCA software records the output of the MCA on a PC and saves the histograms in ASCII format.

The detector operates at 2400 V bias. We set the MCA to a shaping time of 1 μs with a gain of 25 (knobs set to 5.0 and 50) to put the gamma rays of interest within the observation window.

We calibrate the detector using a 49-nCi (12/15/05) ^{60}Co source and a 105.1-μCi (6/1/91) ^{152}Eu source. Table 5.3 shows the lines for calibrating the energy spectrum. Equation 5.5 shows the results of the energy calibration used to identify the ^{83}Rb and ^{84}Rb peaks of interest.

$$E = 0.109518 * ADC - 9.45299 \tag{5.5}$$

Table 5.3: List of gamma peaks used to calibrated GMX-55220 detector.

Source	**Energy [keV]**	**ADC**
Co-60	1173	10806
Co-60	1333	12271
Eu-152	334	3161
Eu-152	779	7156
Eu-152	1408	12938

Given the high activity of the Rb/Kr source the Rb/Kr source was placed 253 cm (100 inches) away from the detector to prevent pileup. Figure 5.7 shows the layout of

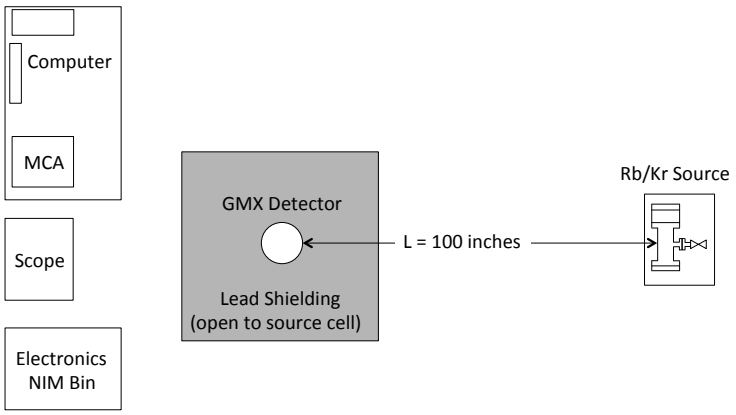

Figure 5.7: Top view of GMX gamma counting setup. (Not to scale.)

the laboratory during gamma counting. The geometry of the detector and surrounding lead shielding prevent us from placing the source in front of the detector. We place the cell to the side of the detector which results in significantly more entrance material. We use gamma calibrations to correct for the decreased efficiency from entering the side of the detector. We take spectra with the Co-60 source 13.5 cm from the front of the detector and repeated the measurement with the source 13.5 cm from the side of the detector. We fit the gamma peaks and extract the number of events in each peak. We take the ratio of events in the two peak (0.73) as the attenuation factor in our activity calculation.

We use the detector efficiency of 1.1×10^{-3} as published in the Ortec HPGe marketing brochure [8]. Figure 5.8 shows the Ortec published efficiency curve. As the Ortec definition of efficiency includes the solid angle at $L_o = 25$ cm, we correct the

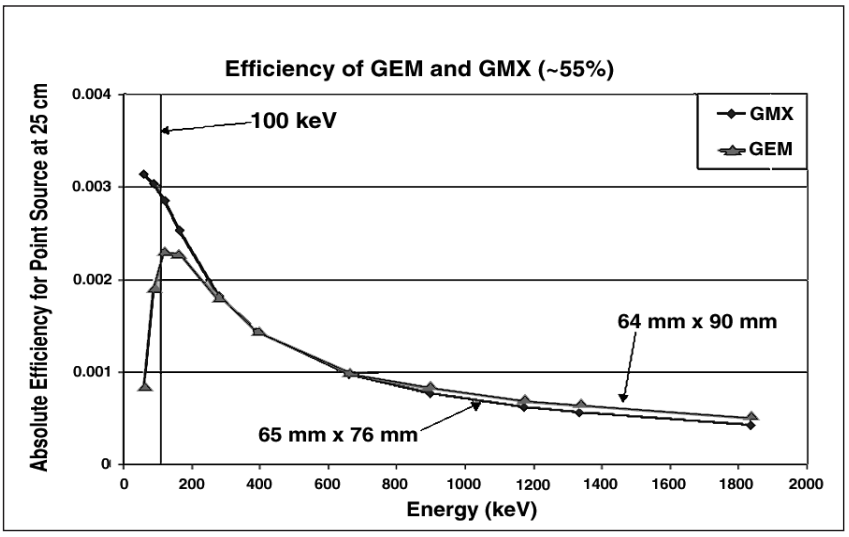

Figure 5.8: GMX-55 efficiency curve from Ortec HPGE Detector Brochure [8].

efficiency for the solid angle at the distance of the Rb/Kr source by employing the ratio of the squared distance to the source.

We account for the attenuation in the walls of the Rb/Kr source cell. Assuming the walls are pure iron we use information from NIST [159] to assign a total gamma attenuation factor of 0.91.

We collected the gamma spectrum for 100 seconds of realtime during which the detector was live for 98.24 seconds. Figure 5.7.1 shows the gamma spectrum taken with the Rb/Kr source. The ^{83}Rb gamma peaks at 520.4 keV, 529.6 keV and 552.5 keV sit just above the annihilation peak at 511 keV as shown in Figure 5.7.1. The ^{84}Rb decay produces a gamma peak at 882 keV (8500 bins) that is visible in the spectrum. We simultaneously fit the spectrum to five Gaussians (one annihilation peak, three ^{83}Rb peaks and one ^{84}Rb peak) and a linear background. Integrating the signal Gaussians we observed 14,982 gamma events in the ^{83}Rb peaks and 4079 events in the ^{84}Rb peak.

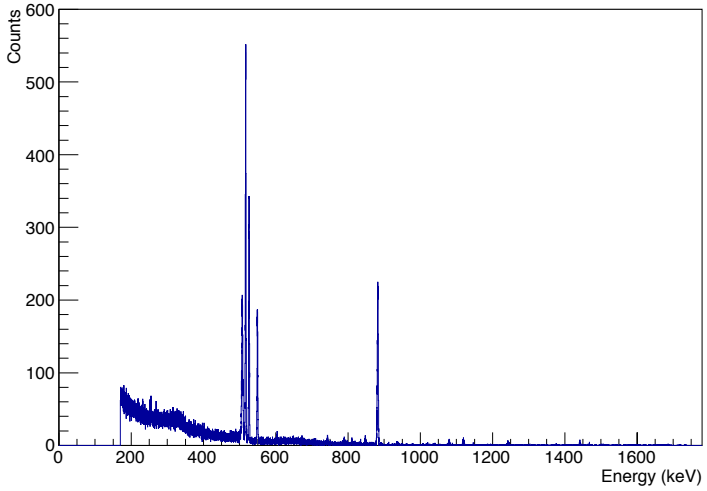

Figure 5.9: Rb/Kr source spectrum

We calculated the observed activity of the source according to

$$A_{observed} = \frac{N_{\text{counts}}}{\Delta t_{\text{sample}}} \cdot \frac{1}{f \cdot g_{\text{cell}} \cdot g_{Det}} \cdot \frac{L^2_{\text{source}}}{\epsilon \cdot L_o} \sim 0.64 \text{ mCi}, \tag{5.6}$$

where f is the summed fraction of decays leading to the gammas of interest, g_{cell} is the attenuation in the source cell walls, g_{Det} is the attenuation from using the side of the detector instead of the front, L_{source} is the distance from the detector to the source and ϵ is the efficiency of the detector at 25 cm (ORTEC's "absolute efficiency").

Correcting for decays in the 6 days between activation and observation we arrive at a total activity of 0.68 mCi. The measured activity agrees nicely with the predicted activity of 0.69 mCi. The errors on both estimates are large (of order 10%) because we extracted the detector efficiency and production cross sections from graphs with very limited resolution.

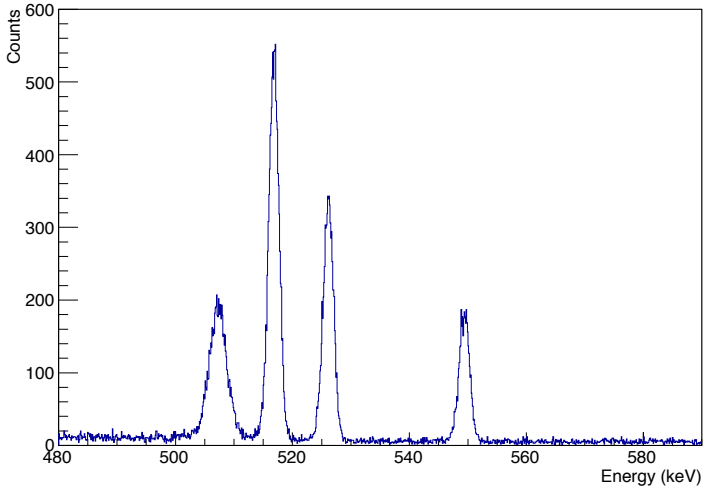

Figure 5.10: Close-up of Rb/Kr source spectrum near ^{83}Rb gamma lines

5.7.2 Electron spectrum

As we are interested in the ^{83m}Kr gas that comes off the walls after decay of the ^{83}Rb we set up a small silicon-detector electron counting station in the Hot Lab at CENPA to measure the emanation. The apparatus consists of a vacuum chamber with a dry pumping station that can be valved off, a long nipple containing the silicon detector, an ion gauge for vacuum measurement and a connection to the Rb/Kr source that can also be valved off. The setup is shown in Fig. 5.11.

To determine the krypton content we evacuated the vacuum system to the $1-^{-6}$ mbar level, valved off the pump, turned off the ion gauge (light from gauge is visible on the detector) and turned on the PIPS silicon detector. We used the TRIMS electronics chain described in section 3.5.2 consisting of the custom preamplifiers, CAEN 5720 desktop digitizer and a NIM-based trigger setup to reduce high frequency noise

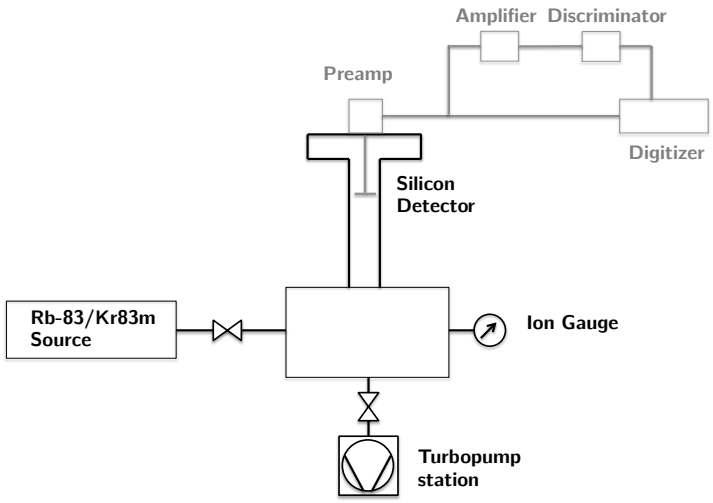

Figure 5.11: Schematic of the setup to measure the gaseous krypton emanating from the walls of the TRIMS ^{83}Rb/^{83m}Kr source. Vacuum parts are shown in black and parts of the detector signal chain are shown in grey.

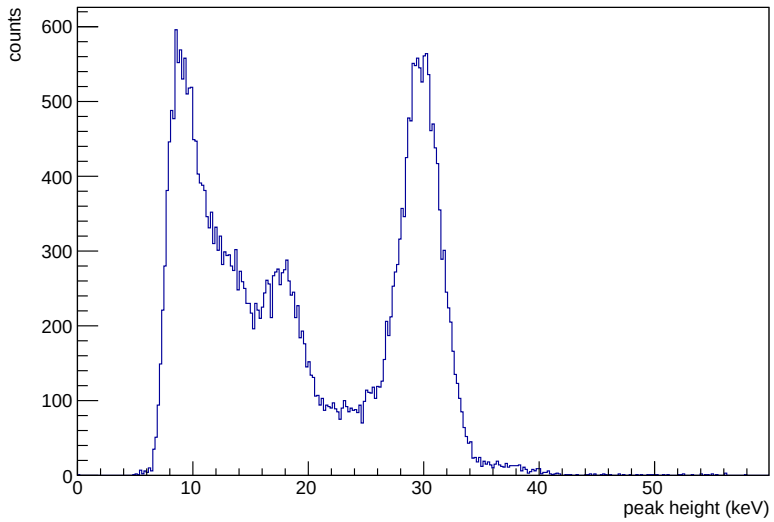

Figure 5.12: Krypton source spectrum with low threshold and filtered with a 4 μs trapezoidal filter. Exponential floor does not appear in calibration data.

triggers.

The krypton source spectrum shows a clear peak at 30 keV which corresponds to the expected dominant conversion electron from ^{83m}Kr. Runs with low threshold see a large spike at low energy that could correspond to the lower energy conversion electrons as shown in in 5.12. The apparent exponential floor does not appear in calibration runs with the same preamplifier setup. Thus, these are taken to be real signals arising from low energy particles hitting the silicon detector.

We estimate the emanation from the walls by comparing the observed count rate in the electron system to the expected count rate based on the known activity of the source in gamma rays. The event rate can be written as the combination of the decay rate R_{decay}, emanation factor $f_{\text{emanation}}$, the branching ratio to the peak of interest $\mathcal{B}$, the geometric efficiency $\epsilon_{\text{geometry}}$ and probability for the electron to backscatter out of the detector $P_{\text{backscatter}}$:

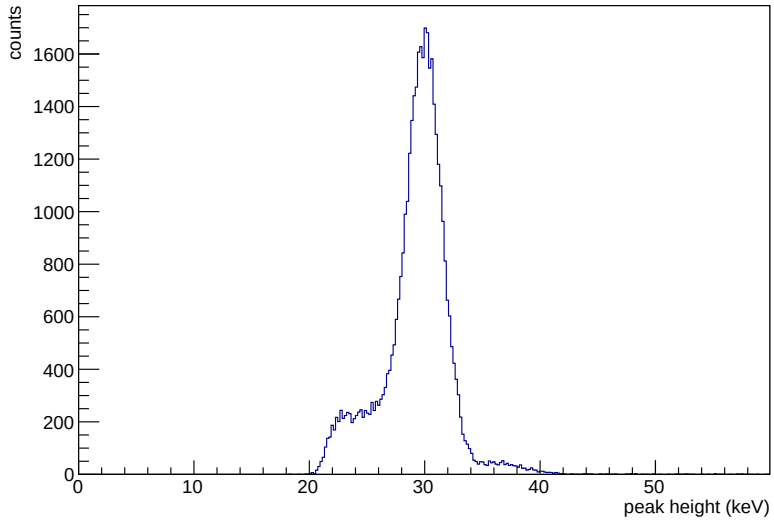

Figure 5.13: Spectrum of events observed in 10-min run of a test setup with the krypton source with threshold set above the 17.8-keV conversion electron peak. The single peak in the spectrum coresponds to the 30.2 keV internal conversion peak of ^{83m}Kr. The mean of the Gaussian fit to the peak corresponds to 30.0 keV.

$$R = R_{\text{decay}} \times f_{\text{emanation}} \times \mathcal{B} \times \epsilon_{\text{geometry}} \times (1 - P_{\text{backscatter}}). \tag{5.7}$$

Fig. 5.13 shows the observed spectrum from 10 minutes of running with the valve to the krypton cell open. The observed count rate was 70 Hz. The estimated activity of the source is the 32 μCi, down four half-lives from the 0.68 mCi measurement in June 2014. The branching ratio to the 30 keV electron is 0.63 [5]. Given the limited energy resolution of the detector we include the branching ratio to the nearby 31 and 32 keV electrons which add an additional 0.11 for a total branching ratio of 0.74. The collection efficiency is the ratio of the volume-integrated solid angle to the total volume of the vacuum system. We estimate the collection efficiency and backscattering probability with simple Monte Carlo techniques.

The efficiency Monte Carlo randomizes the location of the decay within the chamber using cylindrical coordinates (r,ϕ,z). We randomize the direction of the momentum kick received in the decay in angular coordinates (ψ,θ). In cylindrical coordinates we trace the momentum ray to the detector plane, using the radius to determine whether or not the ray is detected. For efficient calculation we only use the hemisphere with θ between 0 and $\pi/2$ because decays at larger angles always travel away from the detector. We correct for this by including a factor of 2 in the denominator of the efficiency calculation. An additional factor of 2 in the denominator comes from half the source volume being outside the field of view of the detector, i.e. within the krypton cell itself or behind the detector. The estimated geometric efficiency is ϵ =0.13% for a simulation using 1×10^7 rays. The Monte Carlo also uses the angle of incidence for detected electrons and previoius KATRIN work on electrons in silicon detectors [160] to determine the overall backscattering probability. The backscatter probability as a function of angle is taken from KATRIN simulation software [160]. For this test setup the average backscattering probability is 24%.

Using the calculated numbers in eqn. 5.7 we find the emanation factor is 8%. This is a factor of 6 lower than naively expected from half the decays being kicked into the wall and half being kicked away from the walls the error bars. The error bars on the emanation factor are difficult to estimate but should be dominated by the uncertainty on the decay rate, ∼30%. While the emanation factor is lower than expected the observed count rate should be adequate for TRIMS calibration purposes.

Half-life measurement

We measured the half-life of the source by looking at the build-up and decay of krypton gas in the chamber as we opened and closed the valves to the pump and cell. We evacuated the source cell, closed the valve to the pump, turned off the pressure sensor and turned on the silicon detector. We measured the counts in five minute intervals to determine the time constant for ^{83m}Kr build-up. After watching the buildup for

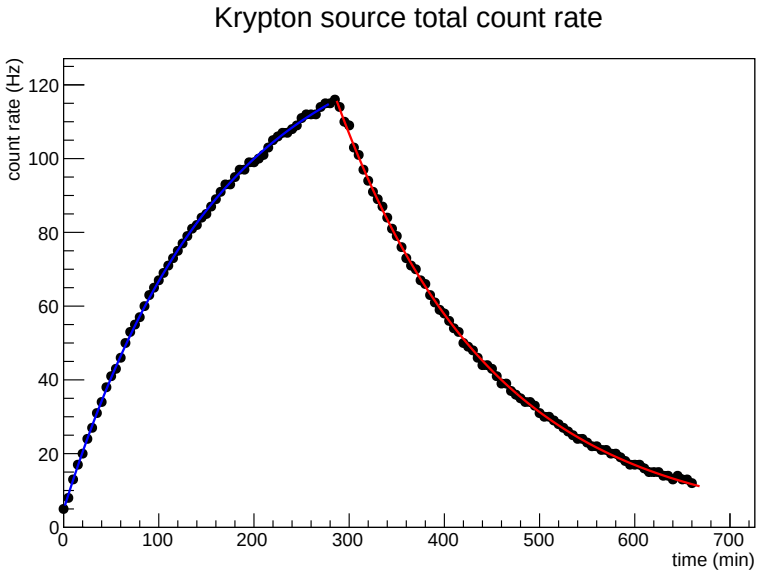

Figure 5.14: Count rate as a function of time for a single buildup and decay half-life measurement cycle for the TRIMS krypton source. The blue line is the exponential fit to the rise time. The red line is the exponential fit to the decay time.

several hours we closed the valve to the krypton source cell and measured the counts in five minutes intervals to determine the decay rate, a direct measurement of the half-life. Fig. 5.14 shows the count rate data taken over a full pump, build-up and decay cycle. The blue line is the fit to the build-up curve and the red line is the fit to the decay curve. The build-up curve fitted half-life is 1.84 hours and the decay curve fitted half-life is 1.89 hours. The NNDC reported ^{83m}Kr half-life is 1.8 hr [5].

5.8 TRIMS krypton spectra: First Light

We introduced krypton to the TRIMS apparatus on August 8, 2015. The first krypton spectrum consisted of a 10-minute run using the beta detector (serial number: 118088) and the ion detector (serial number: 98344) into channels 0 and 1 of the digitizer, respectively. The run triggered on the beta detector discriminator but read out both

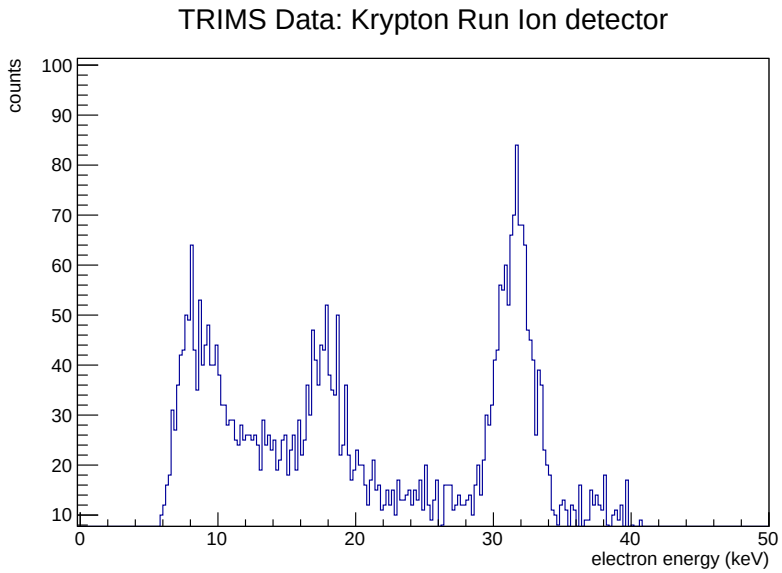

Figure 5.15: Krypton specrum taken in the TRIMS apparatus using the beta detector (serial number: 118088).

channels. The ion detector was positioned at 50.75 mm on the translation stage. Fig. 5.15 and 5.16 show the spectra obtained by filtering the waveforms with a 8 μs trapezoidal filter.

The relative timing of the signals in the beta and ion detector should correspond to the intermediate state half-life of 157 ns. Fig. 5.17 shows the timing of events with a beta detector signal of 9-18 keV and an ion detector signal of at least 2 keV. The ion detector energy is designed to cut the noise peak. Initial indications are that the hardware and software are capable of perfoming the planned measurements.

5.9 Outlook

We have been able to use the krypton calibration to evaluate the performance of the spectrometer with radioactive gas without worry of long-term contamination. The short half-life of ^{83m}Kr means the system quickly returns to safe levels after closing the

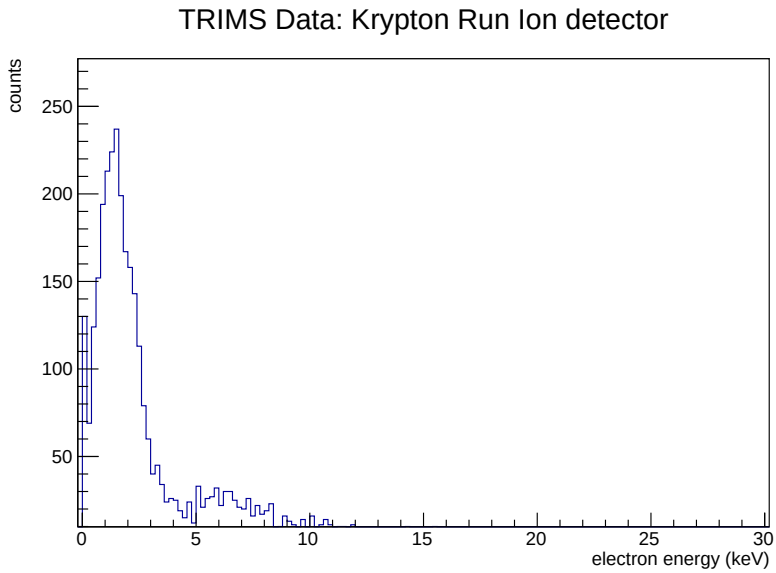

Figure 5.16: Krypton specrum taken in the TRIMS apparatus using the ion detector (serial number: 98344).

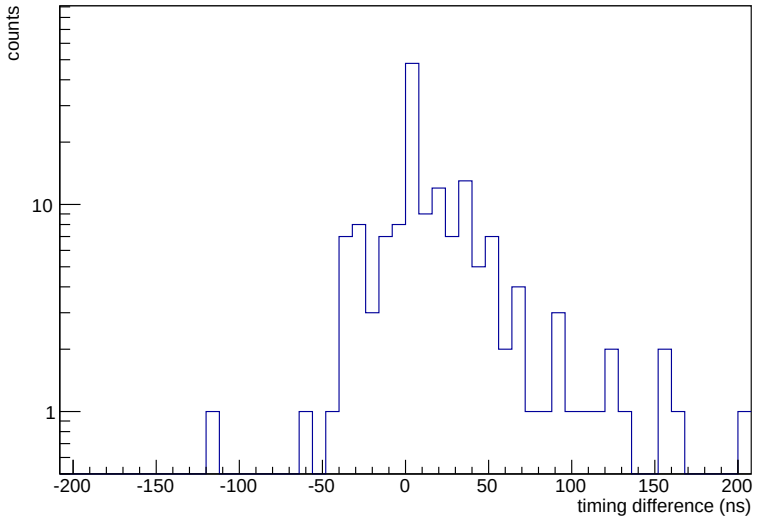

Figure 5.17: Relative timing of pulses in the krypton specra taken in the TRIMS apparatus.

source valve. The ongoing TRIMS calibration campaign shows promising early results as the activity and emanation from the CENPA-made krypton source are adequate to provide good statistics with reasonable calibration times. The krypton source has an effective activity of 1.8 μCi when used as a gaseous source. The remaining 34 μCi of ^{83m}Kr remains trapped in the walls of the source.

A complete krypton calibration of the full TRIMS experiment requires high voltage conditioning of the vacuum system which is expected in late 2015. We will use the krypton ion measurement to evaluate the performance of the spectrometer and assess the physics capability of the current design to measure dissociation in tritium beta decay. Following the initial calibration campaign we plan to implement any necessary changes to the apparatus before proceeding with the tritium measurement. Initial performance has been satisfactory with no indications that upgrades will be necessary for the dissociation measurement.

Chapter 6
DISCUSSION & CONCLUSIONS

An understanding of the molecular final state distribution is necessary for experiments using T_2 beta decay to measure the neutrino mass. The impact of molecular effects on KATRIN is not limited to the theoretical calculations of the final state distribution. The interplay of the experimental uncertainties on the parameters and the theoretical FSD associated with the specified set of parameters gives rise to a variety of systematic uncertainties, some of which have previously been ignored or miscalculated.

This chapter aggregates and, where possible, quantifies the various ways in which FSD uncertainties contribute when a gaseous tritium source is used to measure neutrino mass. These fall into 3 groups: theoretical uncertainties in the FSD itself, uncertainties in the degree of temperature equilibration for T_2, and uncertainties in the isotopic composition of the source gas. This chapter is based on our recent publication on molecular final state effects in neutrino mass experiments published in Physical Review C [4].

6.1 Theoretical uncertainty: toward validation of the calculations

Current calculations lack robust uncertainty estimates despite the fact that the theoretical uncertainty on the width of the final-state distribution must be kept at the 1% level in KATRIN. A significant amount of ongoing work is necessary to demonstrate uncertainty at the percent level. An over 50-year-old discrepancy between the data and theory will be revisited by the TRIMS experiment measurement of the branching ratio to the bound molecular ion.

The branching ratio can be predicted by the standard FSD calculation when considering the long term behavior of the states. Saenz and Roll have indicated that an initial investigation shows the excited states of the electronic ground state dissociate well before the 0.1-0.4 μs flight times applicable to TRIMS [103]. If those results hold the TRIMS branching ratio can be directly compared to the bound portion of the electronic ground state, i.e. no correction is necessary for in-flight de-excitation. The updated calculations should be done in the next year and will be of great interest to both the KATRIN and TRIMS collaborations.

The TRIMS project is making good experimental progress with a krypton calibration phase currently underway. The results of the krypton measurement will be used to determine the feasibility of moving forward on the tritium experiment and inform any design changes that are needed to improve performance.

6.2 Impact on KATRIN and other molecular-tritium-based neutrino mass experiments

The KATRIN experiment has sufficient statistical power that data-taking can be concentrated in the last 20 eV of the spectrum, which removes the theoretical uncertainties in electronic excitation of the molecule as a major concern. There is remaining uncertainty in the width of the ground-state manifold of rotational and vibrational excitations, but we have shown that the broadening has a very simple origin, mainly zero-point motion. Indeed, the semiclassically derived analytic expression yields a variance that agrees with the full theoretical calculation to 7%. Beyond this, a quantitative uncertainty estimate is lacking, and knowledge of the variance at the 1% level has been assumed in the design of experiments like KATRIN. We have reviewed a variety of tests of the theory, finding generally excellent agreement, with the one serious exception being the branching ratio to the bound mass-6 ground state manifold. A new experiment would provide substance for a re-evaluation of the theoretical uncertainties.

An accurate characterization of the composition of the source is necessary for KATRIN. The source gas is high-purity T_2. To determine the isotopic composition, the KATRIN collaboration has developed a laser Raman spectroscopy system called LARA. This system has achieved 0.1% precision [161] and better than 10% accuracy [71] in measurements of the isotopic composition. In principle, a laser Raman system can also provide information about the ortho-para ratio. However, due to the difficulty of *in situ* measurement, LARA is located at a higher-pressure stage prior to cooling and injection into the source. The KATRIN collaboration is studying an extension of the LARA system to measure the ortho-para ratio and is conducting ongoing simulation work on the evolution of the ortho-para ratio and other source parameters.

The KATRIN windowless, gaseous tritium source vessel will be maintained at a temperature of 30 K. In thermal equilibrium at this temperature the ortho-para ratio is approximately 1:1 and states with $J > 1$ are not appreciably populated. The time each molecule spends in the cooled source, however, is short compared to the spin relaxation time. The ortho-para ratio of the gas within the source is therefore expected to be close to the room temperature ratio of 3:1.

Disequilibrium in the source is not confined to the ortho-para ratio because depopulation of higher excited states in free space requires quadrupole transitions that are very slow. The de-excitation process is therefore predominantly collisional and apparatus-dependent. Incomplete thermalization of these excited states would be a source of uncertainty if undiagnosed.

These sources of uncertainty in the FSD translate directly to an uncertainty in the neutrino mass-squared. Robertson and Knapp [10] have shown that any neglected contribution to the variance of the FSD, $\Delta\sigma^2_{\mathrm{FSD}}$, modifies the extracted neutrino mass-squared by

$$\Delta m^2_\nu \simeq -2\Delta\sigma^2_{\mathrm{FSD}}. \tag{6.1}$$

Doss *et al.* [9] calculated the final state distributions arising from the lowest four rotational states of T_2 and the lowest two states of HT and DT, *i.e.* those populated in a 30-K thermal source. The FSDs were binned with 0.01-eV resolution compared to the 0.1-eV resolution used in reporting previous results [1]. We have estimated the variance of each binned distribution in two ways: using the central bin energy value and the reported mean energy value. We take the average of the two results as the best estimate of the variance and half the difference as the width (standard deviation) of the error distribution. The mean excitation energies and estimated variances of the FSDs are listed in Table 6.1. Unfortunately the distributions for higher rotational states of T_2 were not available, and distributions for HT are not available with the required binning resolution. Future calculations of the FSD, such as calculations using the configuration-interaction method, will be helpful in expanding and improving the estimates of the variances.

Figure 6.1 compares the semiclassical variances calculated for initial states $(0, J)$ in T_2 using Eq. 2.31 to the variances estimated from the calculations of Doss *et al.* [9]. From the figure we conclude that the semiclassical model is a good proxy for the FSD variance. The difference between the two is about 7% and independent of J. Of this difference, 1% is attributable to our more accurate result for $E^{\mathrm{kin}}_{\mathrm{rec,max}}$ because all contributions to the variance are proportional to $p^2/2m$. Given the limited set of full FSD calculations available, we use the semiclassical variances to estimate the systematic errors associated with various experimental parameters.

Because both the excitation energy and the recoil kinetic energy depend on the lepton momentum, the effective mean excitation energy of each of the FSDs corresponds to the same laboratory endpoint energy for each isotopolog. Thus the variance of the summed distribution can be taken as the sum of the variances for each isotopolog i and each rotational state J, weighted according to their populations f_i and $P_{J,i}$ for isotope and rotational state, respectively. An additional variance contribution arises from the translational Doppler broadening $\sigma^2_{\mathrm{trans}}$ at a given temperature T.

Table 6.1: Mean excitation energy and variances extracted from the FSD calculations of reference [3]. There is a small contribution to the variance (< 0.004 eV^2) from binning.

Source	J	Mean E_{exc} (eV)	σ_J^2 (eV^2)
T_2	0	1.752	0.194
	1	1.751	0.206
	2	1.750	0.215
	3	1.749	0.262
DT	0	1.752*	0.175
	1	1.752*	0.188

*Shifted to compensate for different recoil kinetic energy [3].

The overall variance σ^2_{tot} of the line broadening can be derived:

$$\sigma^2_{J,i} = \frac{p^2}{2m}\left[\frac{2\mu_i}{3m}E_{\mathrm{zp}(i)} + \frac{2\alpha^2 m_e^2 J(J+1)}{3R_0^2 m}\right] \tag{6.2}$$

$$\sigma^2_{\mathrm{FSD},i} = \sum_J P_{J,i}\sigma^2_{J,i} \tag{6.3}$$

$$\sigma^2_{\mathrm{trans},i} = \frac{p^2}{2m}\frac{2mk_BT}{m_{s,i}+m} \tag{6.4}$$

$$\sigma^2_{\mathrm{tot}} = \sum_i f_i\left(\sigma^2_{\mathrm{FSD},i} + \sigma^2_{\mathrm{trans},i}\right) \tag{6.5}$$

The $P_{J,i}$ weights are given by a Boltzmann distribution for the temperature T. (The translational and rotational temperatures need not be the same). The probability distribution is calculated independently for each isotopolog and summed according to the activity fraction f_i of each isotopolog in the source. The source activity may be expressed in terms of a parameter ϵ_{T} that is the equivalent fractional activity of the gas compared to pure T_2. Additionally the ratio of HT to DT in the source gas $\kappa = f_{\mathrm{HT}}/f_{\mathrm{DT}}$ is used to characterize the makeup of the active contaminants. Eq. 6.6

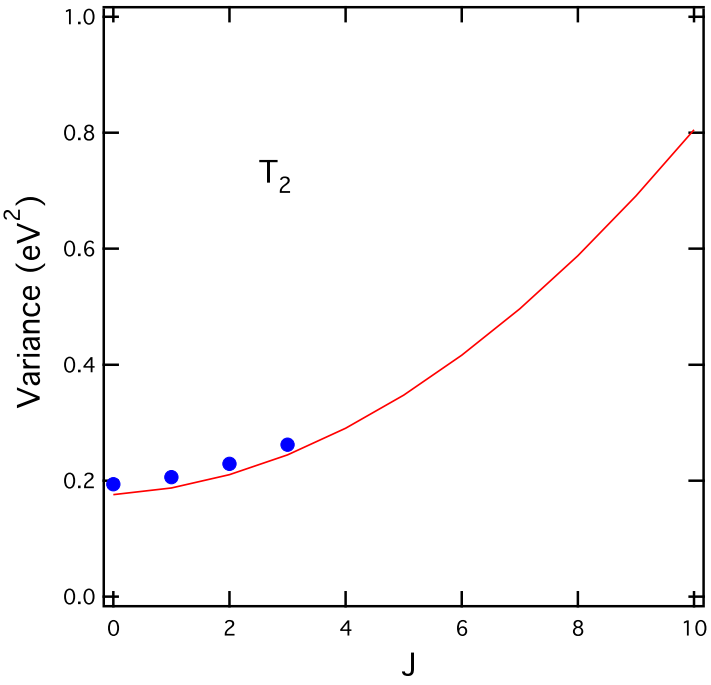

Figure 6.1: Comparison of the variance of the ground-state-manifold FSD produced in T_2 decay as calculated in the semiclassical model, Eq. 2.31 (solid curve, red online), with variances taken from calculations for states up to $J = 3$ described in Ref. [9] (blue dots). (Figure made by R. G. H. Robertson for reference [4].)

shows the functional form of the isotopic weights.

$$f_i = \begin{cases} 2\epsilon_T - 1 & , i = T_2 \\ 2(1-\epsilon_T)/(1+\kappa) & , i = DT \\ 2(1-\epsilon_T)\kappa/(1+\kappa) & , i = HT \end{cases} \tag{6.6}$$

Neglecting inert isotopologs H_2, HD, and D_2, ϵ_T is confined to the range $0.5 \leq \epsilon_T \leq 1$ and is assigned a reference value of 0.95 as in the KATRIN Design Report [11]. The reference value of κ is taken to be 0.1 because the fractional distillation process results in higher levels of deuterium than of protium.

Table 6.2 shows the rotational-state distributions for T_2 thermal 30 K, thermal

Table 6.2: Rotational-state distributions for T_2 at 30 K and 300 K. The energies are those used in Ref. [3] and variances are from the semiclassical width, Eq. 2.31. Probabilities P are calculated from the partition function (Eq. 2.17) using the energies listed in the table and the contributions to the total FSD variance are computed accordingly.

J	E_J	σ^2_{J,T_2}	30 K, Thermal		300 K, Thermal		30 K, $\lambda = 0.75$	
	(meV)	(eV^2)	P (%)	Var Contr	P (%)	Var Contr	P (%)	Var Contr
0	0.00	0.1762	43.70	0.0768	4.73	0.0083	24.6	0.0434
1	5.01	0.1875	55.70	0.1040	35.00	0.0656	75.0	0.1410
2	15.02	0.2103	0.62	0.0013	13.20	0.0277	0.35	0.0007
3	30.05	0.2445	0.01	0.0000	30.70	0.0752	0.01	0.0000
4	50.08	0.2900	0.00	0.0000	6.03	0.0175	0.00	0.0000
5	75.11	0.3469	0.00	0.0000	8.33	0.0289	0.00	0.0000
6	105.16	0.4152	0.00	0.0000	1.02	0.0042	0.00	0.0000
7	140.21	0.4949	0.00	0.0000	0.90	0.0045	0.00	0.0000
8	180.27	0.5859	0.00	0.0000	0.07	0.0004	0.00	0.0000
9	225.34	0.6883	0.00	0.0000	0.04	0.0003	0.00	0.0000
10	275.42	0.8022	0.00	0.0000	0.00	0.0000	0.00	0.0000
			FSD Variance	0.1830		0.2330		0.1850

Table 6.3: Rotational-state distributions for DT at 30 K and 300 K. The energies and variances are from the semiclassical model (see Eq. 2.31). Probabilities are calculated from the partition function (Eq. 2.17) using the energies listed in the table and the contributions to the total FSD variance are computed accordingly.

J	E_J	$\sigma^2_{J,\mathrm{DT}}$	30 K, Thermal		300 K, Thermal	
	(meV)	(eV^2)	P (%)	Var Contr	P (%)	Var Contr
0	0.00	0.1578	78.70	0.1242	11.61	0.0183
1	6.25	0.1692	21.02	0.0356	27.36	0.0463
2	18.76	0.1919	0.28	0.0005	28.11	0.0540
3	37.52	0.2261	0.00	0.0000	19.05	0.0431
4	62.53	0.2716	0.00	0.0000	9.31	0.0253
5	93.80	0.3285	0.00	0.0000	3.39	0.0111
6	131.32	0.3968	0.00	0.0000	0.94	0.0037
7	175.09	0.4765	0.00	0.0000	0.20	0.0010
8	225.12	0.5675	0.00	0.0000	0.03	0.0002
9	281.40	0.6700	0.00	0.0000	0.00	0.0000
10	343.93	0.7838	0.00	0.0000	0.00	0.0000
			FSD Variance	0.1603		0.2029

300 K, and nonthermal 30 K ($\lambda = 0.75$) sources along with the semiclassical FSD variances. Also shown is the contribution each state makes to the total FSD variance of the source in each configuration. The rotational-state distributions for DT and HT are shown in Tables 6.3 and 6.4, respectively. (The rotational-state energies differ slightly from those given by Doss [9], possibly because centrifugal stretching is not included here.) The rotational states up to $J = 7$ contribute significantly at room temperature and further work is necessary to provide an accurate assessment of the systematic error associated with the experimental uncertainty in the rotational-state

Table 6.4: Rotational-state distributions for HT at 30 K and 300 K. The energies and variances are from the semiclassical model (see Eq. 2.31). Probabilities are calculated from the partition function (Eq. 2.17) using the energies listed in the table and the contributions to the total FSD variance are computed accordingly.

J	E_J	$\sigma^2_{J,\mathrm{HT}}$	30 K, Thermal		300 K, Thermal	
	(meV)	(eV^2)	P (%)	Var Contr	P (%)	Var Contr
0	0.00	0.1251	94.09	0.1177	18.12	0.0227
1	10.00	0.1365	5.91	0.0081	36.93	0.0504
2	29.99	0.1592	0.00	0.0000	28.40	0.0452
3	59.98	0.1934	0.00	0.0000	12.46	0.0241
4	99.97	0.2389	0.00	0.0000	3.41	0.0082
5	149.95	0.2958	0.00	0.0000	0.60	0.0018
6	209.94	0.3641	0.00	0.0000	0.07	0.0003
7	279.91	0.4438	0.00	0.0000	0.01	0.0000
8	359.89	0.5348	0.00	0.0000	0.00	0.0000
9	449.86	0.6373	0.00	0.0000	0.00	0.0000
10	549.83	0.7511	0.00	0.0000	0.00	0.0000
		FSD Variance		0.1258		0.1526

distribution. Measurement of the rotational-state temperature and calculations of the higher rotational-state FSDs would significantly improve the error estimates.

To quantify the impact of using an incorrect FSD to analyze neutrino-mass data we examine the differences in variances that arise due to changes in temperature, isotopic purity and ortho-para conditions. For small deviations from the operating parameters the corresponding error in the extracted neutrino mass-squared can be derived from Eq. 6.1. Below, we derive the functional form for ortho-para ratio errors, temperature fluctuations and errors in the isotopic composition. The nominal source parameters

Table 6.5: Reference values of parameters used in estimating FSD and Doppler contributions to the projected uncertainty in the extracted m_ν^2 for KATRIN.

Parameter	Value
Source temperature	$T = 30$ K
Ortho fraction	$\lambda = 0.75$
Tritium fraction in WGTS	$\epsilon_{\mathrm{T}} = 0.95$
Ratio of DT to HT	$\kappa = 0.1$

are shown in Table 6.5.

6.2.1 Temperature: accuracy and fluctuations

The temperature of the source is a key parameter determining the width of the final state distribution. As previously stated, the rotational states of homonuclear T_2 do not equilibrate on short time scales [162] and the exact time required for thermalization in the KATRIN source depends not only on the gas density but also on the materials the gas contacts (*i.e.* walls, permeators, etc.) and the material history (*i.e.* surface treatment, saturation, etc.). The temperature changes the initial rotational-state distribution of the source as seen in the partition function. For small fractional changes in temperature the exponential factors can be expanded, and the resulting shift in variance can be expressed in terms of the fractional temperature change. For a cryogenic source only the $J = 0$ and $J = 1$ states contribute significantly and the shift in FSD variance for a given isotopolog simplifies to a single term, which may be written:

$$\delta\sigma^2_{\mathrm{FSD},i} = \sum_J \sigma^2_{J,i} P_{J,i} \sum_n P_{n,i} \frac{E_{J,i} - E_{n,i}}{kT} \frac{\delta T}{T} \tag{6.7}$$

$$\approx P_{0,i} P_{1,i} \frac{E_{1,i}}{kT^2} (\sigma^2_{1,i} - \sigma^2_{0,i}) \delta T. \tag{6.8}$$

Table 6.6: Variation with temperature of the translational Doppler contribution to the variance for a source near 30 K, calculated from Eq. 6.9.

Source	$\frac{\delta\sigma^2_{\text{trans}}}{\delta T}$ $(10^{-3}$ eV^2/K)
T_2	0.147
DT	0.176
HT	0.220

Table 6.6 shows the translational Doppler variance temperature-variation coefficients for T_2, DT and HT, computed from:

$$\delta\sigma^2_{\text{trans},i} = \frac{p^2}{2m}\frac{2mk_B}{m_{s,i}+m}\delta T. \tag{6.9}$$

The shifts in variance originating from the FSD and translational effects are additive, and each contributes to the overall shift in the extracted neutrino mass-squared according to Eq. 6.1. A temperature change of 0.15 K from the nominal 30 K results in a shift in extracted neutrino mass-squared of 0.11×10^{-3} eV^2.

In reality both thermal fluctuations and inaccuracy in the measurement of the temperature contribute to the uncertainty on neutrino mass. It is reasonable to assume these are uncorrelated errors and thus two independent thermal factors appear in the error budget. The expected temperature fluctuations and uncertainties are taken from the work of Grohmann *et al.* [163, 70].

6.2.2 Isotopic impurities

The isotopic purity of the source plays a major role in neutrino-mass experiments because the width of the FSD varies significantly between isotopologs. In addition to the dependence on the tritium activity fraction ϵ_{T}, there is a dependence on the relative population κ of contaminants HT and DT. Tables 6.2, 6.3 and 6.4 show the variance of the distribution for 30-K sources of tritium-containing isotopologs. The

T_2 results include the thermal source as well as the nonthermal source with $\lambda = 0.75$. The large differences in the FSD variances between HT, DT and T_2 demonstrate the importance of knowing the isotopic purity. The shift in the variance that occurs when the tritium purity of the source ϵ_T changes can be written

$$\delta\sigma^2 = \left[2\sigma^2_{T_2} - \frac{2}{1+\kappa}\sigma^2_{DT} - \frac{2\kappa}{1+\kappa}\sigma^2_{HT}\right]\delta\epsilon_T, \tag{6.10}$$

where σ_i^2 is the sum of the FSD (Eq. 6.3) and translational (6.4) terms. Similarly, the dependence on κ takes the form

$$\delta\sigma^2 = \frac{2(1-\epsilon_T)}{(1+\kappa)^2}\left[-\sigma^2_{DT} + \sigma^2_{HT}\right]\delta\kappa. \tag{6.11}$$

Starting from the nominal source parameters (Table 6.5) and introducing an uncertainty of 1% on the atomic purity of the source would lead to a uncertainty on the neutrino mass-squared of 0.96×10^{-3} eV^2. While conflicting previous results have led to confusion over the impact of errors in the measurement of isotopic purity [9, 71], our results indicate that it plays a major role.

6.2.3 Ortho-para ratio

The impact of the ortho-para condition of the source can also be derived from Eq. 6.5 by considering a slight reordering of rotational states. Due to the two-state nature of the homonuclear system, the state distribution for T_2 is often separated out in terms of the even (para) and odd (ortho) states. The sum of probabilites for all the odd states is the ortho fraction of the source:

$$\lambda = \sum_{J\ \text{odd}} P_J. \tag{6.12}$$

The variances of the ortho and para states can then be considered separately and even normalized independently to yield ortho and para state probabilities, labeled $P_{\text{ortho},J}$ and $P_{\text{para},J}$ respectively. The total variance is then a sum weighted according

to the λ factor.

$$\sigma^2_{\mathrm{FSD,T_2}} = \lambda \sum_{J\ \mathrm{odd}} P_{\mathrm{ortho},J}\sigma^2_{\mathrm{J}} + (1-\lambda) \sum_{J\ \mathrm{even}} P_{\mathrm{para},J}\sigma^2_{\mathrm{J}} \tag{6.13}$$

$$\equiv \lambda\sigma^2_{\mathrm{ortho}} + (1-\lambda)\sigma^2_{\mathrm{para}}. \tag{6.14}$$

If the probabilities within the ortho (para) state relative to the other states are not changing then the impact of the ortho-para transitions can be assessed in terms of the independent ortho and para state variances. Under this assumption, the dependence on $\delta\lambda$ is simply characterized by the difference in the FSD variances arising from the ortho and para distributions:

$$\delta\sigma^2_{\mathrm{FSD}} = (\sigma^2_{\mathrm{ortho}} - \sigma^2_{\mathrm{para}})\delta\lambda. \tag{6.15}$$

For cryogenic sources the equation of the shift in neutrino mass-squared further simplifies, only depending on the difference in the variances of the $J = 0$ and $J = 1$ states. For small changes in temperature which do not appreciably change the occupation of the higher states, the shift in variance is independent of temperature. The contributions from DT and HT remain unchanged as ortho-para considerations only apply to the homonuclear isotopolog. The effect of a change in ortho-para ratio on the extracted neutrino mass-squared is given by:

$$|\Delta m^2_\nu| \approx 2(2\epsilon_{\mathrm{T}} - 1)(\sigma^2_{J=1} - \sigma^2_{J=0})\delta\lambda. \tag{6.16}$$

Given the relatively short time that molecules will spend at cryogenic temperatures in the KATRIN source, the ortho fraction is expected to be close to 0.75, corresponding to the 700 K permeator through which the gas passes in atomic form. A lower bound of 0.57 is set by the beam-tube temperature of 30 K. If λ lies at an unknown value between these bounds the corresponding uncertainty on the extracted neutrino mass-squared would be 3.8×10^{-3} eV^2. Fortunately this is not expected to be the case and early simulations indicate that even in pessimistic scenarios only 3% of the ortho source molecules will transition from the ortho state to the para state [164]. These

KATRIN simulations show a shift in neutrino mass-squared of $0.48(7) \times 10^{-3}$ eV^2 caused by ortho-para transitions. Our calculation is 0.44×10^{-3} eV^2, in good agreement with the results of the simulation. Thus under standard scenarios the ortho-para ratio is not expected to contribute significantly to the uncertainty on the neutrino mass-squared.

While not considered a significant concern for KATRIN, from an experimental perspective the ortho-para ratio warrants more study as the λ factor and associated systematic error can potentially be measured. Current work by the LARA subgroup of KATRIN focuses on how to measure the ortho-para ratio using a modified version of the setup used to measure the isotopic ratio.

6.2.4 States with high rotational quantum number

As previously shown the rotational state distribution plays a significant role in the determination of the width of the FSD. Information about the rotational state distribution in the KATRIN source is limited. Many analyses look only at $J = 0$ and $J = 1$ states, implicitly assuming that quadrupolar transitions are fast enough to ensure thermalization of the ortho states and thermaliziation of the para states (although the states remain out of equilibrium with each other). This assumption has little basis as data on quadrupole transitions are not available in the pressure regime of KATRIN.

The effects of higher rotational states can be described in terms of a rotational state temperature $T_{\text{rotational}}$ uncertainty. The shift in the FSD variance caused by rotational temperature uncertainty is given by the same temperature equation given in Eq. 6.7. Assuming the rotational temperature nearly equilibrates at 30 K, an uncertainty of 10% on the rotational state temperature would cause a neutrino mass-squared uncertainty of 1×10^{-3} eV^2. Measurement of the rotational state temperature would be useful in demonstrating an understanding of the KATRIN source conditions. It is possible to measure the rotational state distribution using a laser Raman exper-

iment similar to the LARA setup but having lower resolution and higher bandwidth spectrometer. In principle a setup making use of two Raman systems with a cold tube in between could provide information on the evolution of the rotational state distribution within the KATRIN source.

6.2.5 Summary of KATRIN uncertainties

Table 6.7 summarizes the projected role of molecular effects on the KATRIN measurement for selected reference values of parameters, showing the sources of systematic error associated with molecular excitations, the projected accuracy on the parameters and the corresponding systematic error on the neutrino mass-squared.

6.3 Summary

The absoute mass scale for neutrinos is important for improving our understanding of nuclear physics, particle physics, astrophysics and cosmology. While the neutrino mass is limited to a small range between roughly 0.05 and 2 eV, physicists have yet to measure the mass scale in the laboratory. The most direct probe of neutrino mass is precise measurement of tritium beta spectrum near the endpoint but this approach relies on an understanding of the final-state distribution.

The KATRIN experiment is the next-generation, tritium-based, neutrino-mass experiment. The apparatus is currently under construction with the goal of achieving 0.2-eV sensitivity by 2022. The KATRIN experiment depends on a detailed understanding of the molecular effects inside the source and pushes the limits of the theoretical understanding of molecular effects in tritium beta decay.

In this thesis we have studied in detail the contribution of molecular effects on the systematic uncertainty of tritium-based neutrino-mass measurements. We developed a semiclassical model to show the majority of broadening due to the molecular effects arises from zero-point motion of the molecule, indicating that precise calculations should be possible. We demonstrated that the uncertainties on KATRIN source

Table 6.7: Summary of molecular-related sources of systematic shift in extracted neutrino mass-squared, the projected accuracy on the experimental parameters and the individual effect on m_ν^2 for the nominal KATRIN parameters shown in Table 6.5. The accuracy of theoretical calculations of the width is taken as 1% in accordance with the KATRIN Design Report [11] but further study is necessary to validate this number as discussed in the text. The achievable experimental uncertainty on the rotational-state temperature is being studied but is not known at this time.

Source of systematic shift	Target accuracy	$\sigma_{\text{syst}}(m_\nu^2)[10^{-3}\text{eV}^2]$
FSD theoretical calculations	$\lvert\Delta\sigma_{\text{FSD}}/\sigma_{\text{FSD}}\rvert \leq 1\%$	6
temperature calibration	$\lvert\Delta T/T\rvert \leq 0.005$	
- translational		0.05
- FSD		0.06
temperature fluctuations	$\lvert\Delta T/T\rvert \leq 0.001$	
- translational		0.009
- FSD		0.01
ortho-para ratio	$\lvert\Delta\lambda/\lambda\rvert \leq 0.03$	0.44
isotopic impurities		
- tritium purity	$\lvert\Delta\epsilon_{\text{T}}/\epsilon_{\text{T}}\rvert \leq 0.03$	2.9
- ratio of HT to DT	$\lvert\Delta\kappa/\kappa\rvert \leq 0.1$	0.03
higher rotational states	$\lvert\Delta T/T\rvert_{\text{rotational}} \leq 0.1$	1

parameters such as isotopic purity and rotational state temperature must be tightly controlled in order to prevent introducing previously unaccounted for errors in the measurement of m_ν^2 that can arise from the reliance on an absolute FSD. Our table of molecular systematics (table 6.7) has motivated further theoretical work as well as experimental studies needed to demonstrate an FSD understanding at the 1% level. The updated calculations will provide a more detailed uncertainty estimates and will be essential in interpreting the KATRIN data.

While the FSD calculations require verification few viable measurements have beeen identified. The calculations provide concrete estimates of the branching ratio to the bound molecular ion (or conversely the likelihood for the daughter molecular to dissociate). The TRIMS experiment is poised to make a measurement of the dissociation likelihood in tritium beta decay, thereby providing an independent assessment of the calculations used in molecular tritium beta decay experiments such as KATRIN. This independent measurement will be address the 50-year discrepancy between dissociation data and calculations.

The TRIMS apparatus makes use of silicon detectors and magnetic guiding to mitigate the systematics that plagued the interpretation of older dissociation data. The apparatus has been constructed and commissioned with a gaseous Kr-83m source. A full test of the system is expected in late 2015 with an eye toward tritium data in early 2016. The apparatus is in good working order and any modifications to the hardware are expected to be minor. The TRIMS dissociation measurement will be an important test of the theory and will be essential in demonstrating that the calculations meet the KATRIN uncertainty requirement of 1% on the FSD width.

BIBLIOGRAPHY

[1] Alejandro Saenz, Svante Jonsell, and Piotr Froelich. Improved molecular final-state distribution of HeT^+ for the β-decay process of T_2. *Phys. Rev. Lett.*, 84:242–245, 2000.

[2] O. Fackler, B. Jeziorski, W. Kołos, H. J. Monkhorst, and K. Szalewicz. Accurate theoretical β-decay energy spectrum of the tritium molecule and its neutrino mass dependence. *Phys. Rev. Lett.*, 55:1388, 1985.

[3] N. Doss. *Calculated final state probability distributions for T_2 β-decay measurements.* PhD thesis, University of London, 2007.

[4] L. I. Bodine, D. S. Parno, and R. G. H. Robertson. Assessment of molecular effects on neutrino mass measurements from tritium β decay. *Phys. Rev. C*, 91:035505, Mar 2015.

[5] E.A. McCutchan. Nuclear Data Sheets for A = 83. *Nuclear Data Sheets*, 125(0):201 – 394, 2015.

[6] S.-C. WU. Nuclear Data Sheets for A = 83. *Nuclear Data Sheets*, 92(4):893, 2001.

[7] Z. Kovács, F. Tárkányi, S. M. Qaim, and G. Stöcklin. Excitation functions for the formation of some radioisotopes of rubidium in proton induced nuclear reactions on ^{nat}Kr, ^{82}Kr and ^{83}Kr with special reference to the production of ^{81}Rb(^{81m}Kr) generator radionuclide. *International Journal of Radiation Applications and Instrumentation. Part A. Applied Radiation and Isotopes*, 42(4):329, 1991.

[8] ORTEC. The best choice of high purity germanium (HPGe) detector. URL http://www.ortec-online.com/download/Best-Choice-High-Purity-Germanium-HPGe-Detector.pdf, 2014. Accessed: 2014 June 16.

[9] Natascha Doss, Jonathon Tennyson, Alejandro Saenz, and Svante Jonsell. Molecular effects in investigations of tritium molecule β decay endpoint experiments. *Phys. Rev. C*, 73:025502, 2006.

[10] R. G. H. Robertson and D. A. Knapp. Direct measurements of neutrino mass. *Ann. Rev. Nucl. Part. Sci.*, 38:185, 1988.

[11] Katrin design report 2004. Technical report, 2005.

[12] Conseil de physique Instituts Solvay. Structure et proprits des noyaux atomiques : rapports et discussions du septime conseil de physique tenu a bruxelles du 22 du 29 octobre 1933. Paris, 1934. l'Institut international de physique Solvay. ID: 4052708.

[13] Y. Fukuda, T. Hayakawa, E. Ichihara, et al. Evidence for oscillation of atmospheric neutrinos. *Phys. Rev. Lett.*, 81:1562–1567, Aug 1998.

[14] B. Aharmim, S. N. Ahmed, A. E. Anthony, et al. Combined analysis of all three phases of solar neutrino data from the sudbury neutrino observatory. *Phys. Rev. C*, 88:025501, Aug 2013.

[15] S. Abe, T. Ebihara, S. Enomoto, et al. Precision measurement of neutrino oscillation parameters with kamland. *Phys. Rev. Lett.*, 100:221803, Jun 2008.

[16] F. P. An, J. Z. Bai, A. B. Balantekin, et al. Observation of electron-antineutrino disappearance at daya bay. *Phys. Rev. Lett.*, 108:171803, Apr 2012.

[17] Y. Abe, C. Aberle, T. Akiri, et al. Indication of reactor $\overline{\nu}_e$ disappearance in the double chooz experiment. *Phys. Rev. Lett.*, 108:131801, Mar 2012.

[18] J. K. Ahn, S. Chebotaryov, J. H. Choi, et al. Observation of reactor electron antineutrinos disappearance in the RENO experiment. *Phys. Rev. Lett.*, 108:191802, May 2012.

[19] M. H. Ahn, E. Aliu, S. Andringa, et al. Measurement of neutrino oscillation by the k2k experiment. *Phys. Rev. D*, 74:072003, Oct 2006.

[20] P. Adamson, I. Anghel, C. Backhouse, et al. Measurement of neutrino and antineutrino oscillations using beam and atmospheric data in minos. *Phys. Rev. Lett.*, 110:251801, Jun 2013.

[21] K. Abe, J. Adam, H. Aihara, et al. Measurement of neutrino oscillation parameters from muon neutrino disappearance with an off-axis beam. *Phys. Rev. Lett.*, 111:211803, Nov 2013.

[22] OPERA Collaboration, N. Agafonova, A. Aleksandrov, et al. Observation of tau neutrino appearance in the cngs beam with the opera experiment. 2014(10), 2014.

[23] K.A. Olive et al. Review of Particle Physics. *Chin.Phys.*, C38:090001, 2014.

[24] B. Kayser and R. N. Mohapatra. The nature of massive neutrinos. In David O. Caldwell, editor, *Neutrino Physics*. Springer, New York, 2001.

[25] Boris Kayser, Francoise Gibrat-Debu, and Frederic Perrier. *The physics of massive neutrinos*. World Scientific, 1989.

[26] Felix Boehm and Petr Vogel. *Physics of massive neutrinos*. Cambridge University Press, 1992.

[27] J. Schechter and J. W. F. Valle. Neutrinoless double-β decay in SU(2)×U(1) theories. *Phys. Rev. D*, 25:2951–2954, Jun 1982.

[28] The EXO-200 Collaboration. Search for majorana neutrinos with the first two years of exo-200 data. *Nature*, 510(7504):229–234, 06 2014.

[29] A. Gando, Y. Gando, H. Hanakago, et al. Limit on neutrinoless $\beta\beta$ decay of ^{136}Xe from the first phase of kamland-zen and comparison with the positive claim in ^{76}Ge. *Phys. Rev. Lett.*, 110:062502, Feb 2013.

[30] M. Agostini, M. Allardt, E. Andreotti, et al. Results on neutrinoless double-β decay of ^{76}Ge from phase i of the gerda experiment. *Phys. Rev. Lett.*, 111:122503, Sep 2013.

[31] R. G. H. ROBERTSON. Empirical survey of neutrinoless double beta decay matrix elements. *Modern Physics Letters A*, 28(08):1350021, 2013.

[32] Huaiyu Duan, George M. Fuller, J. Carlson, and Yong-Zhong Qian. Neutrino mass hierarchy and stepwise spectral swapping of supernova neutrino flavors. *Phys. Rev. Lett.*, 99:241802, Dec 2007.

[33] K. Hirata, T. Kajita, M. Koshiba, et al. Observation of a neutrino burst from the supernova sn1987a. *Phys. Rev. Lett.*, 58:1490–1493, Apr 1987.

[34] R. M. Bionta, G. Blewitt, C. B. Bratton, et al. Observation of a neutrino burst in coincidence with supernova 1987a in the large magellanic cloud. *Phys. Rev. Lett.*, 58:1494–1496, Apr 1987.

[35] E. N. Alekseev, L. N. Alekseeva, V. I. Volchenko, and I. V. Krivosheina. Possible detection of a neutrino signal on 23 February 1987 at the Baksan Underground Scintillation telescope of the Institute of Nuclear Research. *JETP Letters*, 45(10):589–592, May 25 1987.

[36] M. Aglietta, G. Badino, G. Bologna, et al. On the event observed in the mont blanc underground neutrino observatory during the occurrence of supernova 1987 a. *EPL (Europhysics Letters)*, 3(12):1315, 1987.

[37] Georg G. Raffelt. Supernova neutrino observations: What can we learn? *Nuclear Physics B - Proceedings Supplements*, 221(0):218 – 229, 2011. The Proceedings of the 22nd International Conference on Neutrino Physics and Astrophysics The Proceedings of the 22nd International Conference on Neutrino Physics and Astrophysics.

[38] J. N. Bahcall and S. L. Glashow. Upper limit on the mass of the electron neutrino. *Nature Letters*, (326):476–477, 1987.

[39] Steen Hannestad. Neutrinos in cosmology. *New Journal of Physics*, 6(1):108, 2004.

[40] K.N. Abazajian, E. Calabrese, A. Cooray, et al. Cosmological and astrophysical neutrino mass measurements. *Astroparticle Physics*, 35(4):177 – 184, 2011.

[41] Planck Collaboration, P. A. R. Ade, N. Aghanim, et al. Planck 2015 results. XIII. cosmological parameters. arXiv:1502.01589, 2015.

[42] E. W. Otten and C. Weinheimer. Neutrino mass limits from tritium β decay. *Rep. Prog. Phys.*, 71:086201, 2008.

[43] G. C. Hanna and B. Pontecorvo. The β-spectrum of H^3. *Phys. Rev.*, 75:983, 1949.

[44] S. C. Curran, J. Angus, and A. L. Cockroft. The beta-spectrum of tritium. *Phys. Rev.*, 76:853–854, 1949.

[45] K.-E. Bergkvist. A high-luminosity, high-resolution study of the end-point behaviour of the tritium β-spectrum (i). basic experimental procedure and analysis

with regard to neutrino mass and neutrino degeneracy. *Nucl. Phys. B*, 39:317–370, 1972.

[46] Karl-Erik Bergkvist. On some atomic effects in the tritium β-spectrum. *Phys. Scr.*, 4:23, 1971.

[47] J. F. Wilkerson et al. Limit on $\bar{\nu}_e$ mass from free-molecular-tritium beta decay. *Phys. Rev. Lett.*, 58:2023, 1987.

[48] R. G. H. Robertson et al. Limit on $\bar{\nu}_e$ mass from observation of the β decay of molecular tritium. *Phys. Rev. Lett.*, 67:957, 1991.

[49] V. A. Lyubimov et al. Estimation of the neutrino rest mass from measurements of the tritium β spectrum. *Sov. Phys. JETP*, 54(4):616, 1981.

[50] W. Stoeffl and D. J. Decman. Anomalous structure in the beta decay of gaseous molecular tritium. *Phys. Rev. Lett.*, 75:3237, 1995.

[51] H. C. Sun et al. (beijing neutrino-mass experiment). *Chin. J. Nucl. Phys.*, 15:261, 1993.

[52] H. Kawakami et al. New upper bound on the electron anti-neutrino mass. *Phys. Lett. B*, 256:105, 1991.

[53] E. Holzschuh, M. Fritschi, and W. Kündig. Measurement of the electron neutrino mass from tritium β-decay. *Phys. Lett. B*, 287:381, 1992.

[54] C. Kraus et al. Final results from phase II of the Mainz neutrino mass search in tritium β decay. *Eur. Phys. J. C*, 40:447, 2005.

[55] V. M. Lobashev. The search for the neutrino mass by direct method in the tritium beta-decay and perspectives of study it in the project katrin. *Nucl. Phys. A*, 719:C153, 2003.

[56] V. N. Aseev et al. Upper limit on the electron antineutrino mass from the Troitsk experiment. *Phys. Rev. D*, 84:112003, 2011.

[57] G. Beamson, H. Q. Porter, and D. W. Turner. The collimating and magnifying properties of a superconducting field photoelectron spectrometer. *J. Phys. E.: Sci. Instrum.*, 13:64, 1980.

[58] G. J. Feldman and R. D. Cousins. Unified approach to the classical statistical analysis of small signals. *Phys. Rev. D*, 57:3873, 1998.

[59] M. Galeazzi, F. Fontanelli, F. Gatti, and S. Vitale. End-point energy and half-life of the ^{187}Re β decay. *Phys. Rev. C*, 63:014302, 2000.

[60] A. Nucciotti. The MARE project. *J. Low Temp. Phys.*, 151(3-4):597, 2008.

[61] C. Arnaboldi. Measurement of the p to s wave branching ratio of ^{187}Re β decay from beta environmental fine structure. *Phys. Rev. Lett.*, 96:042503, 2006.

[62] C. W. Reich and B. Singh. Nuclear data sheets for A= 163*. *Nucl. Data Sheets*, 111:1211, 2010.

[63] M. Galeazzi et al. The electron capture decay of 163-Ho to measure the electron neutrino mass with sub-eV accuracy (and beyond). arXiv:1202.4763 [physics.ins-det], 2012.

[64] R. G. H. Robertson. Examination of the calorimetric spectrum to determine the neutrino mass in low-energy electron capture decay. *Phys. Rev. C*, 91:035504, Mar 2015.

[65] L. Gastaldo et al. The electron capture ^{163}Ho experiment ECHo. *J. Low Temp. Phys.*, 176(5-6):876–884, 2014.

[66] J. W. Engle et al. Evaluation of ^{163}Ho production options for neutrino mass measurements with microcalorimeter detectors. *Nucl. Instr. & Meth. in Phys. Res. B*, 311:131–138, 2013.

[67] Karlsruhe Institute of Technology. Katrin website. URL http://www.katrin.kit.edu. Accessed: 2015 August 4.

[68] M. Slezák et al. Electron line shape of the KATRIN monitor spectrometer. *J. Inst.*, 8:T12002, 2013.

[69] T. Thümmler, R. Marx, and C. Weinheimer. Precision high voltage divider for the KATRIN experiment. *New J. Phys.*, 11:103007, 2009.

[70] S. Grohmann et al. The thermal behavior of the tritium source in KATRIN. *Cryogenics*, 55-56:5–11, 2013.

[71] M. Schlösser et al. Accurate calibration of the laser Raman system for the Karlsruhe Tritium Neutrino Experiment. *J. Mol. Struct.*, 1044:61, 2013.

[72] P. J. Doe et al. Project 8: Determining neutrino mass from tritium beta decay using a frequency-based method. arXiv:1309.7093 [nucl-ex], 2013.

[73] B. Monreal and J. Formaggio. Relativistic cyclotron radiation detection of tritium decay electrons as a new technique for measuring the neutrino mass. *Phys. Rev. D*, 80:051301, 2009.

[74] D. M. Asner, R. F. Bradley, L. de Viveiros, P. J. Doe, J. L. Fernandes, et al. Single electron detection and spectroscopy via relativistic cyclotron radiation. *Phys. Rev. Lett.*, 2015. in press.

[75] M. Jerkins et al. Using cold atoms to measure neutrino mass. *New J. Phys.*, 12:043022, 2010.

[76] E. W. Otten. Comment on 'Using cold atoms to measure neutrino mass'. *New J. Phys.*, 13:078001, 2011.

[77] M. Jerkins et al. Reply to comment on 'Using cold atoms to measure neutrino mass'. *New J. Phys.*, 13:078002, 2011.

[78] John F. Wilkerson and R. G. H. Robertson. Direct measurements of neutrino mass. In David O. Caldwell, editor, *Neutrino Physics*. Springer, New York, 2001.

[79] D. H. Wilkinson. Small terms in the beta-decay spectrum of tritium. *Nucl. Phys. A*, 526:131–140, 1991.

[80] Susan Gardner, Veronique Bernard, and Ulf G. Meissner. Radiative tritium beta-decay and the neutrino mass. *Phys. Lett. B*, 598:188–196, 2004.

[81] Fedor Simkovic, Rastislav Dvornicky, and Amand Faessler. Exact relativistic tritium beta-decay endpoint spectrum in a hadron model. *Phys. Rev. C*, 77:055502, 2008.

[82] Chong-En Wu and Wayne W. Repko. One-half-plus to one-half-plus beta decay with neutrino mass effects in the elementary particle treatment of weak interactions. *Phys. Rev. C*, 27:1754–1760, Apr 1983.

[83] S.S. Masood, S. Nasri, J. Schechter, et al. Exact relativistic beta decay endpoint spectrum. *Phys. Rev. C*, 76:045501, 2007.

[84] Samina S. Masood, Salah Nasri, and Joseph Schechter. Fine structure of beta decay endpoint spectrum. *Int. J. Mod. Phys. A*, 21:517–532, 2006.

[85] G. Audi, A. H. Wapstra, and C. Thibault. The AME2003 atomic mass evaluation: (II). tables, graphs and references. *Nucl. Phys. A*, 729:337, 2003.

[86] Włodzimierz Kołos, Bogumił Jeziorski, Krzysztof Szalewicz, and Hendrik J. Monkhorst. Molecular effects in tritium β decay: Transitions to the discrete electronic states of the het+ molecule. *Phys. Rev. A*, 31:551–555, Feb 1985.

[87] A. E. Kramida. A critical compilation of experimental data on spectral lines and energy levels of hydrogen, deuterium, and tritium. *At. Data Nucl. Data Tables*, 96:586–644, 2010.

[88] D. C. Morton, Q. Wu, and G. W. F. Drake. Energy levels for the stable isotopes of atomic helium (^{4}He I and ^{3}He I). *Can. J. Phys.*, 84:83–105, 2006.

[89] Sz. Nagy, T. Fritioff, M. Björkhage, I. Bergström, and R. Schuch. On the q-value of the tritium beta decay. *Europhys. Lett.*, 74(3):404, 2006.

[90] Svante Jonsell, Alejandro Saenz, and Piotr Froelich. Neutrino-mass determination from tritium β decay: Corrections to and prospects of experimental verification of the final-state spectrum. *Phys. Rev. C*, 60:034601, 1999.

[91] M. Cantwell. Molecular excitation in beta decay. *Phys. Rev.*, 101:1747, 1956.

[92] W. Kołos and L. Wolniewicz. Accurate computation of vibronic energies and of some expectation values for H2, D2, and T2. *J. Chem. Phys.*, 41(12):3674–3678, 1964.

[93] L. Wolniewicz. Variational treatment of the heh+ ion and the decay in ht. *The Journal of Chemical Physics*, 43(4):1087–1091, 1965.

[94] J. A. Coxon and P. G. Hajigeorgiu. Experimental Born–Oppenheimer potential for the $X^1\Sigma^+$ ground state of HeH^+: Comparison with the ab initio potential. *J. Molec. Spectrosc.*, 193:306, 1999.

[95] David M. Bishop and Lap M. Cheung. Rigorous theoretical investigation of the ground state of h2. *Phys. Rev. A*, 18:1846–1852, Nov 1978.

[96] B. G. Anex. Ground state of the HeH^+ molecule ion. *J. Chem. Phys.*, 38:1651, 1963.

[97] J. D. Stuart and F. A. Matsen. One-center wavefunction for the ground state of the HeH^+ molecular ion. *J. Chem. Phys.*, 41:1646, 1964.

[98] H. H. Michels. Molecular orbital studies of the ground and low-lying excited states of the HeH^+ molecular ion. *J. Chem. Phys.*, 44:3834, 1966.

[99] O. Fackler, M. Mugge, H. Sticker, N. Winter, and R. Woerner. The calculation of molecular final states and their effect on a precision neutrino mass experiment. In J. Tran Thanh Van, editor, *Massive Neutrinos in Astrophysics and in Particle Physics, Proc. Fourth Moriond Workshop*, page 273. Editions Frontiéres, Paris, 1984.

[100] R. L. Martin and J. S. Cohen. Excitation and ionization accompanying the beta decay of T_2. *Phys. Lett. A*, 110:95, 1985.

[101] Y. V. Vanne and A. Saenz. Numerical treatment of diatomic two-electron molecules using a B-spline based CI method. *J. Phys. B.: At. Mol. Opt. Phys.*, 37:4101, 2004.

[102] A. Saenz. Photoabsorption and photoionization of HeH^+. *Phys. Rev. A*, 67:033409, 2003.

[103] A. Saenz. Private communication, 2014.

[104] J.A. Formaggio and J. Barrett. Resolving the reactor neutrino anomaly with the KATRIN neutrino experiment. *Phys. Lett. B*, 706:68 – 71, 2011.

[105] S. Mertens, T. Lasserre, S. Groh, et al. Sensitivity of next-generation tritium beta-decay experiments for keV-scale sterile neutrinos. *J. Cosmology Astropart. Phys.*, 2015(02):020, 2015.

[106] N. Doss and J. Tennyson. Excitations to the electronic continuum of $^3HeT^+$ in investigations of T_2 beta-decay experiments. *J. Phys. B: At. Mol. Opt. Phys.*, 41:125701, 2008.

[107] A. Saenz and P. Froelich. Effect of final-state interactions in allowed β decays. II. Reliability of the β-decay spectrum for T_2. *Phys. Rev. C*, 56:2162, 1997.

[108] P. Froelich, B. Jeziorski, W. Kołos, et al. Probability distribution of excitations to the electronic continuum of HeT^+ following the β decay of the T_2 molecule. *Phys. Rev. Lett.*, 71:2871–2874, 1993.

[109] L. Wolniewicz, I. Simbotin, and A. Dalgarno. Quadrupole transition probabilities for the excited rovibrational states of H_2. *Astrophys. J. Suppl. Ser.*, 115(2):293, 1998.

[110] J. D. Jackson, S. B. Treiman, and H. W. Wyld. Possible tests of time reversal invariance in beta decay. *Phys. Rev.*, 106:517, 1957.

[111] J. Byrne, P. G. Dawber, M. G. D. van der Grinten, et al. Determination of the electron anti-neutrino angular correlation coefficient a0 and the parameter $|\lambda| = |G(A)/G(V)|$ in free neutron beta decay from measurements of the integrated energy spectrum of recoil protons stored in an ion trap. *J.Phys.*, G28:1325–1349, 2002.

[112] G. H. Dieke. Molecular spectrum of hydrogen and its isotopes. *J. Molec. Spectrosc.*, 2:494–517, 1958.

[113] A. H. Snell, F. Pleasanton, and H. E. Leming. Molecular dissociation following radioactive decay: Tritium hydride. *J. Inorg. Nucl. Chem.*, 5:112–117, 1957.

[114] S. Wexler. Dissociation of TH and T_2 by β-decay. *J. Inorg. Nucl. Chem.*, 10:8–16, 1958.

[115] D. K. Veirs and G. M. Rosenblatt. Raman line positions in molecular hydrogen: H_2, HD, HT, D_2, DT, and T_2. *J. Molec. Spectrosc.*, 121:401, 1987.

[116] M.-C. Chuang and R. N. Zare. Rotation-vibration spectrum of HT: Line position measurements of the 1-0, 4-0, and 5-0 bands. *J. Molec. Spectrosc.*, 121:380, 1987.

[117] A. Carrington et al. Infrared bound to quasibound vibration-rotation spectrum of HeH+ and its isotopes. *Chem. Phys.*, 81:251, 1983.

[118] M. W. Crofton, R. S. Altman, N. H. Haese, and T. Oka. Infrared spectra of $^4HeH^+$, $^4HeD^+$, $^3HeH^+$, and $^3HeD^+$. *J. Chem. Phys.*, 91:5882, 1989.

[119] F. Matsushima, T. Oka, and K. Takagi. Observation of the rotational spectra of $^4HeH^+$, $^4HeD^+$, $^3HeH^+$, and $^3HeD^+$. *Phys. Rev. Lett.*, 78:1664, 1997.

[120] H. G. M. Edwards, D. A. Long, and H. R. Mansour. Pure rotational and vibration-rotational Raman spectra of tritium, $^3H_2$. *J. Chem. Soc., Faraday Trans. 2*, 74:1203, 1978.

[121] H. G. M. Edwards, D. A. Long, H. R. Mansour, and K. A. B. Najm. The pure rotational and vibration-rotational Raman spectra of $^1H^3H$ and $^2H^3H$. *J. Raman Spectrosc.*, 8:251, 1979.

[122] D. E. Tolliver, G. A. Kyrala, and W. H. Wing. Observation of the infrared spectrum of the helium-hydride molecular ion $^4HeH^+$. *Phys. Rev. Lett.*, 43:1719, 1979.

[123] A. Carrington, J. Buttenshaw, R. A. Kennedy, and T. P. Softley. Observation of bound to quasibound vibration-rotation transitions in the HeH^+ ion. *Mol. Phys.*, 44:1233, 1981.

[124] P. Bernath and T. Amano. Detection of the infrared fundamental band of HeH^+. *Phys. Rev. Lett.*, 48:20, 1982.

[125] Z. Liu and P. B. Davies. Infrared laser absorption spectroscopy of rotational and vibration rotational transitions of HeH^+ up to the dissociation threshold. *J. Chem. Phys.*, 107:337, 1997.

[126] Z. Liu and P. B. Davies. Measurement of the pure rotational quasibound spectrum of HeH^+ in a laboratory plasma by direct laser absorption. *Phys. Rev. Lett.*, 79:2779, 1997.

[127] J. Purder, S. Civiš, C. E. Blom, and M. C. van Hemert. Diode laser spectra and potential energy curve for the molecular ion HeH^+. *J. Molec. Spectrosc.*, 153:701, 1992.

[128] W. Y. Fan, N. T. Hunt, Z. Liu, and P. B. Davies. Infrared laser spectrum of high J pure rotational transitions of $^4HeD^+$. *Chem. Phys. Lett.*, 298:222, 1998.

[129] D.-J. Liu, W.-C. Ho, and T. Oka. Rotational spectroscopy of molecular ions using diode lasers. *J. Chem. Phys.*, 87:2442, 1987.

[130] C. E. Blom, K. Möller, and R. R. Filgueira. Gas discharge modulation using fast electronic switches: application to HeH^+. *Chem. Phys. Lett.*, 149:489, 1987.

[131] D. Bishop and L. M. Cheung. A theoretical investigation of HeH^+. *J. Molec. Spectrosc.*, 75:462, 1979.

[132] D. Basu and A. K. Barua. Photodissociation of HeH^+ molecular ion. *J. Phys. B.: At. Mol. Opt. Phys.*, 17:1537, 1984.

[133] J. Loreau, J. Lecointre, X. Urbain, and N. Vaeck. Rovibrational analysis of the XUV photodissociation of HeH^+ ions. *Phys. Rev. A*, 84:053412, Nov 2011.

[134] H. B. Pedersen et al. Crossed beam photodissociation imaging of HeH^+ with vacuum ultraviolet free-electron laser pulses. *Phys. Rev. Lett.*, 98:223202, 2007.

[135] H. B. Pedersen et al. Experimental investigation of dissociation pathways of cooled HeH^+ following valence electron excitation at 32 nm by intense free-electron-laser radiation. *Phys. Rev. A*, 82:023415, 2010.

[136] I. Dumitriu and A. Saenz. Photodissociation of the HeH^+ molecular ion. *J. Phys. B.: At. Mol. Opt. Phys.*, 42:165101, 2009.

[137] S. Wexler and F. T. Porter. Probability of formation of $[(^3He)^+]_{4s}$ following beta decay of tritium. *J. Chem. Phys.*, 50:5428, 1969.

[138] R. W. Schmieder. Optical emission spectrum of tritium gas. *J. Opt. Soc. Am.*, 72:593, 1982.

[139] R. Raitz Von Frentz et al. Observation of vibrational transitions in $(^3He^3H)^+$ after β-decay in the tritium molecule. *Phys. Lett. A*, 47:301, 1974.

[140] S. T. Staggs, R. G. Hamish Robertson, D. L. Wark, P. P. Nguyen, John F. Wilkerson, et al. Energy of the 32-keV transition of $^{83}Kr^m$ and the atomic mass difference between ^3H and ^3He. *Phys.Rev.*, C39:1503–1510, 1989.

[141] F. Pleasanton and A. H. Snell. Ionization following internal conversion in xenon. *Proc. R. Soc. London A*, 241:141–152, 1957.

[142] R. Brun and F. Rademakers. ROOT - an object oriented data analysis framework. *Nucl. Instr. & Meth. in Phys. Res. A*, 389:81–86, 1997.

[143] James F. Ziegler. SRIM-2003. *Nucl. Instr. Meth. B*, 219-220:1027–1036, 2004.

[144] B.L. Wall, J.F. Amsbaugh, A. Beglarian, et al. Dead layer on silicon p-i-n diode charged-particle detectors. *Nucl. Instr. & Meth. in Phys. Res. A*, 744:73–79, 2014.

[145] S. Agostinelli, J. Allison, K. Amako, et al. Geant4 –a simulation toolkit. *Nuclear Instruments and Methods in Physics Research Section A: Accelerators, Spectrometers, Detectors and Associated Equipment*, 506(3):250 – 303, 2003.

[146] J. Allison, K. Amako, J. Apostolakis, et al. Geant4 developments and applications. *Nuclear Science, IEEE Transactions on*, 53(1):270–278, Feb 2006.

[147] P. M. Stier and C. F. Barnett. Charge exchange cross sections of hydrogen ions in gases. *Phys. Rev.*, 103:896, 1956.

[148] Canberra Semiconductor. Passivated Implanted Planar Silicon (PIPS®) Detectors. URL http://www.canberra.com/products/detectors/pdf/passivated_pips_C39313a.pdf, 2012.

[149] H. P. Mumm et al. emiT: an apparatus to test time reversal invariance in polarized neutron decay. *Rev. Sci. Instrum.*, 75:5343, 2004.

[150] M. A. Howe et al. Sudbury Neutrino Observatory neutral current detector acquisition software overview. *IEEE*, 51(3):878 – 883, June 2004. See also http://orca.physics.unc.edu/.

[151] SAES Getters Group. St-101® non-evaporable getters. URL http://www.saesgetters.com/sites/default/files/St%20101%20Brochure_2.pdf, 2007.

[152] Kenji Ichimura, Naoya Inoue, Kuniaki Watanabe, and Toyosaburo Takeuchi. Absorption and desorption of hydrogen, deuterium, and tritium for ZrVFe getter. *Journal of Vacuum Science & Technology A*, 2(3):1341–1347, 1984.

[153] Mark Howe. OrcaRoot documentation @misc. URL http://orca.physics.unc.edu/~markhowe/Subsystems/ORCARoot.html. Accessed: 2015 April 9.

[154] V. T. Jordanov and G. F. Knoll. Digital synthesis of pulse shapes in real time for high resolution radiation spectroscopy. *Nucl. Inst. & Meth. A*, 345, 1994.

[155] M. Morelle. Private communication, 2012.

[156] Daniel J. Decman and Wolfgang Stoefflˆ. Atomic electron binding energies of multiply charged krypton ions by internal-conversion-electron spectroscopy. *Phys. Rev. Lett.*, 64:2767–2770, Jun 1990.

[157] S.Y.F. Chu, L.P. Ekstrm, and R.B. Firestone. WWW Table of Radioactive Isotopes, database version 2.1 [Retrieved 2014 May 4]. *LBNL Isotopes Project Nuclear Data Dissemination, Berkeley, CA*, 2004.

[158] M. J. Berger, J. S. Coursey, M. A. Zucker, and J. Chang. Estar, pstar, and astar: Computer programs for calculating stopping-power and range tables for electrons, protons, and helium ions (version 1.2.3) [online]. *National Institute of Standards and Technology, Gaithersburg, MD.*, 2005.

[159] National Institute of Standards and Technology. Tables of x-ray mass attenuation coefficients and mass energy-absorption coefficients from 1 keV to 20 MeV for elements Z =1 to 92 and 48 additional substances of dosimetric interest. NISTIR 5632: URL http://www.nist.gov/pml/data/xraycoef/, 1996. Accessed: 2014 June 22.

[160] P. Renschler. *KESS —A new Monte Carlo simulation coe for low-energy electron interactions in silicon detectors.* PhD thesis, Karlsruhe Institute of Technology, October 2011.

[161] S. Fischer et al. Monitoring of tritium purity during long-term circulation in the KATRIN test experiment LOOPINO using laser Raman spectroscopy. *Fusion Sci. Tech.*, 60:925–930, 2011.

[162] P. C. Souers. *Hydrogen Properties for Fusion Energy.* U. of California Press, Berkeley, 1986.

[163] S. Grohmann, T. Bode, H. Schoen, and M. Suesser. Precise temperature measurement at 30 K in the KATRIN source cryostat. *Cryogenics*, 51(8):438 – 445, 2011.

[164] M. Kleesiek. *A Data-Analysis and Sensitivity-Optimization Framework for the KATRIN Experiment.* PhD thesis, Karlsruhe Institute of Technology, July 2014.

Appendix A

TRIMS SOFTWARE

The TRIMS simulation comprises a set of classes and ROOT macros for generating and analyzing simulated data. The following lists the description of the classes and macros:

A.0.1 Simulation Software

- FSEvent: a class that creates a decay event at a random location in the detector, sets the inital beta energy based on the known spectrum, sets the ion energy based on the theoretical spectrum and randomizes the initial direction of travel of the ion. This class is called in FSSim.

- FSSim: a class for simulating TRIMS data. This class calls FSEvent to create decays according to the input parameters and number of decays defined at run time. This class takes a parameter file and number of decays desired as input.

- ParameterFiles: the parameter files list the parameters in the following order: Lchamber[m] Vchamber[V] Bfield[G] Pressure[mbar] BetaDetArea[mm^s] IonDetArea[mm^2] branchT branch3He branch3HeT bckgd3HeH bckgd3He bckgdH THcont[%] resolution[eV] jitter[s]

- plothistos.C: a macro designed to take FSSim output and create Energy vs Time of Flight spectra as well as cut on measured ion energy to fiducialize the volume. This macro will be updated to become the general TRIMS data analysis code.

- moreplots.C: a ROOT macro designed to plot the basic simulation output. This will not be used on real data as it relies on the MC truth values, plotting the ion energy at every physical step: decay, after acceleration to detector, deposition in detector, smearing by the data-acquisition system.

- GetBRmacro.C: a macro designed to compare two datasets with differing HT contents and return branching ratio for the T_2 final state.

A.0.2 Digitizer Software

The digitizer was not previously implemented in ORCA or OrcaRoot. M. Howe added the functionality to ORCA while L. Bodine wrote the OrcaRoot decoder and processor. Below we describe the waveform digitization software:

- ORCA: records waveforms from CAEN DT5720 digitizer during runs. The waveform trace length is selectable prior to the run and can vary between 4 μs and 1 ms.

- OrcaROOT: an object-oriented ROOT-based C++ toolkit written by Jason Detwiler and maintained by Mike Marino that converts ORCA files into ROOT trees. Each data-taker (e.g. digitizer) requires a separate decoder class to convert the 32-bit unsigned integers recorded by ORCA into the correct data format and processor class to save the data in the proper format.

- ORCaen5720Decoder: OrcaRoot decoder that parses the 32-bit words in the ORCA file into number of samples (trace length), active channel map, trigger time tag, and waveform data.

- ORCaen5720Processor: OrcaRoot Processor that calls the OrcaRoot decoder to decode DT5720 data found by the OrcaRoot executable. The processor stores the data in ROOT trees with one entry for each ORCA record (trigger).

- `orcaroot_TRIMS`: OrcaRoot executable that calls the ORCaen5720Processor to turn ORCA files into ROOT files.

- TRIMSWaveformFilter: A waveform filter class that takes ROOT trees generated by orcarootTRIMS and applies a trapezoidal filter with parameters defined a runtime. The trapezoidal filter parameters are the total length of the filter (roughly half of the integration time, the filter gap (optimized based on signal rise time) and the polarity tag. This class is based on a custom ROOT waveform filtering class written by Michelle Leber for testing the KATRIN DAQ system.

ROOT file format

Object-oriented Real-time Control and Acquisition (ORCA) (described in section 3.5.2) records the TRIMS waveform data in binary files with custom format. The ORCA files are converted to ROOT trees [142] using a custom data processor added to OrcaRoot [153].

The data tree contains one entry for each trigger of the CAEN DT5720 digitizer. Each entry contains the waveforms for all active channels, each stored in its own branch. The waveform peak height and relative timing are reconstructed during post-processing and the values are appended to the tree. The ROOT tree branches are listed in table A.1.

A.0.3 Analysis Software

The TRIMS analysis uses the digitizer software to produce energy and time of flight information for each event.

- TRIMSAnalysis: The main TRIMS analysis class. This class calls the WaveformFilter class to process waveforms and determine the energy and timing of each signal. The class produces energy-vs-time-of-flight spectra that are then

Table A.1: TRIMS ROOT tree format. Entries with $ exist for each channel.

Branch	**Description**
runNumber	ORCA run number, recorded by ORCA in header
subRunnumber	ORCA subrunnumber, recorded by ORCA in header
eventcount	event trigger number within given run
clock	the trigger time tag, i.e. clock tick related to trigger of digitizer
numSamples	number of samples in each waveform
channelmask	active channel map
waveform#	an array of length NumSamples that stores the waveform from channel $.
ADC$	peak height extracted from trapezoidal filtering of waveform$
time$	arrival time of waveform$ extracted from trapezoidal filtering
PILEUP	flag indicating the event is considered pileup
NOISE	flag indicating the event is considered noise

fit to extract the population in each mass group. The fit is implemented using Minuit and includes energy and timing uncertainty in addition to 4 mass groups (mass-1, mass-3, mass-4 and mass-6).

Appendix B

TRIMS BAKE-OUT

The TRIMS vacuum system is designed to reach 10^{-11} mbar before the addition of gaseous tritium. To reduce outgassing from the walls and achieve the low base pressure the system is baked at high temperature. The high temperature bake-out also reduces the hydrogen content of the system, preventing HT backgrounds from contaminating our sample excessively.

B.1 Bake-out Method

TRIMS uses a modular approach with surface heating tapes and blankets. The heating-tape method has the advantage of being able to vary the temperature across the apparatus but requires many channels of temperature readout and heater current control. T. D. Van Wechel and D. A. Peterson designed and built a multichannel temperature readout and control system.

Heating tapes come in a variety of lengths, widths and power ratings. From a given manufacturer heating tapes generally have constant power per unit length at a given voltage. Varying the temperature across the system can be achieved by using separate power supplies for each section of the vacuum system. The extensive temperature readout scheme incorporates an Omega temperature controller and custom relay box. The system, developed for TRIMS, was tested on the Project 8 system and performed according to specification.

Flexible silicone Omega heating tapes that reach 230°C have a power density 4.3 W/in^2. For uninsulated tapes in air, convective losses occur and power densities of 5 W/in^2 are required to reach 250°C. Heating tests indicate that power densities as

low as 2 W/in^2 are achievable with foil-insulated vacuum systems. The lower power density corresponds to 50% coverage with heater tapes. The vacuum system surface area is estimated at 2000 in^2, requiring 4 kW (33.3 A at 120 Vac) of power from 166 ft of half-inch heating tape.

B.1.1 Thermometry

Temperature sensors are placed on various vacuum parts including each VAT valve, each vacuum gauge, the UV window, the translational stage, and the main chamber. The thermocouples for heater control are placed between the heating tape and the part, resulting in a conservative temperature reading.

Secondary temperature sensors may be insulated from the tape or attached to unwrapped sections to more accurately measure the temperature of the components themselves. An RTD temperature readout array could be used for this purpose. We have a 10-channel array consisting of current sources for the RTDs and unity gain amplifiers. The amplifiers give ∼100-mV signals that can be connected to LabJack ADCs for read out. This setup is easy to monitor in ORCA and could provide valuable information about the uniformity of the temperature across the vacuum system.

B.1.2 Temperature Control

For temperature-control purposes the vacuum system is broken down into zones that can be heated to the same temperature. These zones are independently controlled, allowing maximum heating across the system.

The most basic method of temperature control is the use of Variacs to limit the power to each tape. Because the Variacs are manually adjusted the heating rate may be inadvisable to regulate. Our system has strong limits on the heating rate, making manual adjustment difficult.

Alternatively thermocouple-based temperature controllers can be used to slowly increase the temperature of the vacuum system at a set rate. The use of several

controllers with temperature readback at various points within each subsection would be ideal. This can be achieved with a multichannel controller and a supplementary temperature readout array consisting of current sources and unity gain amplifiers read by ADCs.

B.2 Component temperature ratings

The maximum tolerable temperature of each component has been considered as well as the overall heating strategy. Many components have lower than desirable maximum temperatures and some components have temperature differentials and rates that place considerable constraints on the heating method.

The maximum tolerable temperature of the major components are listed in table B.1. During the vacuum design phase careful attention was paid to the maximum temperature ratings of each component. The UV-window maximum temperature of 200°C sets the limit of the bake-out temperature limit for the main vacuum line. On the VCR manifold the vent gas purifier and tritium/hydrogen cells must remain at room temperature to prevent contamination from outgassing. The other main components of the vacuum system have higher maximum temperatures in excess of 250°C.

B.2.1 Non-bakeable Components

Some components are particularly heat-sensitive and cannot be brought significantly above room temperature. The N_2 purifier and the tritium/hydrogen cells are kept at room temperature. These items are insulated/cooled during bake-out.

During bake-out these components can be kept at room temperature by leaving a reasonable distance between the last heating tape and the sensitive component. If additional cooling is necessary a heat sink or cooling ring can be implemented. Close temperature monitoring is necessary, requiring dedicated temperature sensors at each sensitive component. While this method requires care and extra temperature sensors

Table B.1: Maximum bake-out and operating temperatures

Component	**Manufacturer**	**Maximum Temperature (°C)**	
		Bake-out	**Operating**
Main chamber	Larson	450	–
PIPS detectors	Canberra	200	–
Translation stage	Lesker	200	–
Right-angle valves	VAT	300	60
Gate valves	VAT	150	65
Bellows-sealed Valves	Nupro/Swagelok	315	315
Pirani gauges	MKS	250	50
RGA	SRS	300	70
Nude ion gauge	Leybold-Heraeus	400	400
UV window	Lesker	200	200
Ion pump	Varian	400	250
Getter pumps	SAES	750	250
Sorption pump	Huntington	250	-196
Turbo pump	Varian	120	35
N_2 purifier	SAES	40	25
BNC feedthrough	Lesker	400	165
Microdot feedthrough	Lesker	450	165

it provides the cleanest solution since no venting is required following bake-out.

Additionally, the turbomolecular pumping cart is kept at room temperature by virtue of the long bellows between the right-angle valve and the gate valves. This pump is used during bake-out to handle the high gas load.

The high-voltage divider chain must also be removed during bake-out. A layer of

clean foil between the glass chamber and the heating blanket will protect the glass from contamination.

B.2.2 Heating Rates

The lowest specified heating rate is for the VAT right-angle valves. The maximum heating rate for the valves is 60°C/hr=1°C/min. This rate should be reasonable for the other parts as well and is designated as our nominal heating rate.

The UV window is rated for 2-3°C/min. The window should not be directly heated and should be shielded with many layers of aluminum foil to avoid thermal gradients.

The feedthroughs can be ramped at 25°C/min to a maximum temperature of 400°C for the BNC and 450°C for the Microdot.

The detectors may also be sensitive to the heating rate but Canberra does not specify a maximum rate. The maximum bake-out temperature of 200°C is for the bakeable version specified at order. The detectors are heated through their detector mounts, which for the ion detector includes a glass insulator. Additional detector heating through the signal and grounding cables necessitates consideration of the tolerable thermal gradients.

B.3 Pumping during bake-out

The turbocart evacuates the vacuum system prior to bake-out. After roughing out the system, the ion pump is used to bring the chamber pressure as low as possible. The contents of the vacuum system is measured with the RGA prior to bake-out. During bake-out the gas load is quite high, necessitating constant use of the turbopump. Additionally the sorption pump is baked out with the gas load pumped directly by the turbocart.

At the end of the bake-out process the nonevaporable getters pumps are activated. The getter activation power is provided by a DC power supply. The activation temperature of the in-vacuum pump body is 750°C. During activation the pump housing

can reach up to 250°C, consistent with the bake-out temperature for the rest of the system.

At the end of bake-out the system temperature is lowered slowly. As the system cools, the ion pump is started along with one getter pump. As the temperature drops to 25°C the pressure should approach the 10^{-11} mbar level.

B.4 Vacuum Monitoring during bake-out

The nude ion gauge can be run at high temperature and monitors the vacuum level during the evacuation and bake-out process as well as during normal operation. This signal provides a continuous benchmark for understanding the vacuum level before, during and after bake-out. Use during bake-out requires a special cable constructed of high-temperature compatible materials to replace the plastic housing and standard LEMO connector.

The RGA cannot be run at high temperature but is used before and after bake-out to determine the cleanliness of the vacuum system. The total pressure measurement is compared to the nude ion gauge for reliability. Additional gas correction factors may be necessary depending on the level of detail required.

Appendix C
TRIMS SLOW CONTROLS AND DATABASE

In this appendix we describe the TRIMS slow controls and database systems.

C.1 Slow Controls

A slow controls system monitors system changes that do not require fast processing. Table C.1 lists all items to be recorded by slow controls.

With the exception of RGA data slow-controls data is acquired with ORCA. The majority of systems are monitored via LabJack U12 ADCs. The ADCs have eight single-ended ±10-V inputs or four differential inputs with programmable gains of 1, 2, 4, 5, 8, 10, 16, or 20. Inputs to the LabJack ADCs pass through a buffer circuit in order to prevent signal sagging due to impedance mismatch. A USB interface provides easy connection to the DAQ computer. The components read out via ADCs are listed in table C.2 along with their output voltage ranges.

The RGA data is recorded via a standalone LabVIEW-based application provided by Stanford Research Systems. This application is Windows-based and runs on a separate slow controls PC.

C.2 Database

The TRIMS database runs on PostgreSQL on `marie.npl.washington.edu`. The primary means of data entry is OrcaRoot DAQ entry (e.g. run number, trigger rate), Slow-Controls entry (e.g. high voltage, pressure readings) and manual entry (e.g. ion detector position, HT contamination setting).

Since these entry methods are not synchronized, separating the data-tables accord-

ing to entry method reduces the number of null entries and simplifies data extraction. The OrcaRoot routine updates all DAQ-related values at once for each run, as well as supplying data (mean and standard deviation) about the distributions of certain critical slow-controls variables for each run.

The Slow-Controls-entry values are read by ORCA from the LabJack ADCs and shipped every ten seconds to a text file on the DAQ computer. Once a minute, a `launchd` task scheduler launches a bash script, `bash_fill_orca.sh`, that in turn runs the python script `filltable_ORCA.py`. This python code reformats the new data entries in the text file and uploads them to the TRIMS database via an SSH connection. The code for these operations was written by Ting Lin.

The manual-entry variables will typically be updated at different times. The web-based manual-update client propagates the most recent values for the columns that are not being updated when adding a record to the `manual_data` table. At the same time, it adds a record to the `manual_update_history` table indicating which columns were updated at that time. Both these records carry the same automatically-generated timestamp.

The result is four data tables:

1. `daq_data` (DAQ-related data): Table C.3

2. `sc_data` (slow-controls data): Table C.4

3. `manual_data` (manual-entry data): Table C.5

4. `manual_update_history` (timestamps changes to each manual-entry variable): Table C.6

Each variable is assigned a PostgreSQL data type. The TIMESTAMP type stores the date and time in the format `yyyy-mm-ddhh:mm:ss`; database entries, unlike events

in an ORCA file, do not require subsecond precision. The REAL type stores floating-point numbers with (on most platforms) at least six decimal digits of precision, in a range from `1E-37` to `1E+37`. The maximum INTEGER is in excess of 2 billion and thus provides ample headroom for run numbers and HT mixing states.

Table C.1: TRIMS Slow Controls items

Subsystem	**Item**	**Units**	**Readout Mode**
High Voltage	Current	A	ADC + SC
	Voltage	V	ADC + SC
Vacuum System	Pirani Gauge Pressure	mbar	ADC + SC
	Nude Ion Gauge Pressure	mbar	2 ADCs + SC
	RGA Pressure	mbar	Standalone
	Spinning Rotor Gauge	mbar	ADC +SC
Magnets	PS Current, outer pair	A	ADC + SC
	PS Current, inner pair	A	ADC + SC
	PS Voltage, outer pair	V	ADC + SC
	PS Voltage, inner pair	V	ADC + SC
Detector	Ion Detector Bias	V	Manually recorded
	Beta Detector Bias	V	Manually recorded
	Detector Position	mm	Manually recorded
DAQ	DAQ Status	–	ORCA
	HT Mixing status	–	Manually recorded
	Data Rate	Hz	ORCA
	Trigger Level	mV	ORCA
	Pedestal	mV	ORCA
	Coincidence window	μs	Manually recorded

Table C.2: TRIMS LabJack ADC Readouts. Items marked with † are planned but not yet implemented.

Subsystem	**Item**	**Units**	**Range (V)**
High Voltage	Current	A	0–10
	Voltage	V	0–10
Vacuum System	Pirani Gauge Pressure	mbar	0.33–5.5
	Nude Ion Gauge Coefficient	–	0–10
	Nude Ion Gauge Exponent	–	4–9
	Ion Pump Pressure	Torr	0–0.1
	Spinning Rotor Gauge	mbar	0–10
Magnets	Hall probe reading†	G	0–2
	PS Current, outer pair†	A	0–10
	PS Current, inner pair†	A	0–10
	PS Voltage, outer pair†	V	0–10
	PS Voltage, inner pair†	V	0–10

Table C.3: `daq_data` DB table

Column	Description	Data Type	Size (B)
`time`	Date/time	TIMESTAMP	8
`run_num`	Run number	INTEGER	4
`data_rate`	Data rate (Hz)	REAL	4
`pedestal`	ADC pedestal (mV)	REAL	4
`HV_mean`	HV average (kV)	REAL	4
`HV_sigma`	HV sigma (kV)	REAL	4
`B_mean`	B-field average (kG)	REAL	4
`B_sigma`	B-field sigma (kG)	REAL	4
`P_ig_mean`	Ion gauge average (mbar)	REAL	4
`P_ig_sigma`	Ion gauge sigma (mbar)	REAL	4
	All 10 columns		44

Table C.4: `sc_data` DB table

Column	Description	Data Type	Size (B)
`time`	Date/time	TIMESTAMP	8
`hv_voltage`	High voltage (V)	REAL	4
`hv_current`	High-voltage current (A)	REAL	4
`pressure_ion`	Ion-gauge pressure (mbar)	REAL	4
`coefficient_ion`	Ion-gauge pressure coeff	REAL	4
`exponent_ion`	Ion-gauge pressure exp	INTEGER	4
`pressure_cep`	CEP pressure (mbar)	REAL	4
`mag_field`	Magnetic field reading (G)	REAL	4
`mag_current_outer`	Magnet-outer-pair current (A)	REAL	4
`mag_current_inner`	Magnet-inner-pair current (A)	REAL	4
`mag_voltage_outer`	Magnet-outer-pair voltage (A)	REAL	4
`mag_voltage_inner`	Magnet-inner-pair voltage (A)	REAL	4
	All 12 columns		52

Table C.5: `manual_data` DB table.

Column	Description	Data Type	Size (B)
`time`	Date/time	TIMESTAMP	8
`ion_det_pos`	Position of ion detector (in)	REAL	4
`th_mixing_state`	HT mixing status	INTEGER	4
`trigger_level`	Trigger level (mV)	REAL	4
`nim_coin_window`	NIM-logic coincidence window (µs)	REAL	4
`cep_main_connected`	Status of main-chamber CEP	BOOLEAN	1
`cep_h2_connected`	Status of protium-line CEP	BOOLEAN	1
`cep_t2_connected`	Status of tritium-line CEP	BOOLEAN	1
	All 8 columns		27

Table C.6: `manual_update_history` DB table.

Column	Description	Data Type	Size (B)
`time`	Date/time	TIMESTAMP	8
`ion_det_pos_updated`	Status of manual-entry variable	BOOLEAN	1
`th_mixing_state_updated`	Status of manual-entry variable	BOOLEAN	1
`nim_coin_window_updated`	Status of manual-entry variable	BOOLEAN	1
`trigger_level_updated`	Status of manual-entry variable)	BOOLEAN	1
`cep_connection_updated`	Status of manual-entry variables	BOOLEAN	1
	All 6 columns		13

Appendix D

TRIMS POWER REQUIREMENTS

This section outlines the TRIMS experiment power requirements according to each subsystem. Table D.1 shows the power requirements of 115-Vac components that will be continually used. Table D.2 shows the power requirements of 115-Vac components that will be intermittently used. Table D.3 shows the power requirements of 208-Vac components that will be used. Gray-scale values are those that have been calculated from other quantities or inferred from rules of thumb regarding power consumption.

Table D.1: TRIMS 115 Vac Constant Power requirements

Component	**Voltage [V]**	**Current [A]**	**Max Power [W]**
Ion pump	110 or 120	10	1200
Spinning Rotor Gauge	115	1.25	150
Digitizer	115	1	115
DAQ Computers	120	8.4	1000
NIM crate + Modules	120	10	1200
HV PS	120–125	3	345
F/O board	110–120	1.5	180
TOTAL		35.2	4190

Table D.2: TRIMS 115 VAC Intermittent Power requirements

Component	**Voltage [V]**	**Current [A]**	**Max Power [W]**
Turbostation	110	2	230
Ion Gauge Controller	110 or 130	1.9	220
Pirani Gauge Controller	90–120	0.075	9
SRG Controller	90–120	1.25	150
RGA	120	0.5	60
UV Lamp	120	∼0.1	∼12
Pulser	100–240	0.45	50 (VA)
Battery Charger	115	0.6	72
Temp controller	120	10	1200
Heating tapes	120	∼43	5000
Sorption heating jacket	120	3	350
Getter heater	30(DC)	3.5	105
TOTAL		∼65	∼7500

Magnets

The magnets are powered from two Danfysik 823 regulated magnet power supplies. These supplies require 208-Vac, 3-phase power. The amperage is not listed in the manual but the max power draw is listed at 17.9 kVA, corresponding to 50 A. These power supplies will be run at significantly lower output power than rated: 150 A at 40 V instead of 250 A at 50 V. They should not draw more than 40 A, as observed in a similar setup for the accelerator.

Table D.3: TRIMS 208-VAC Power requirements. Gray values are estimates.

Component	**Voltage [V]**	**Current [A]**	**Max Power [W]**
Mag Power Supply 1	208 (3ϕ)	40	17900
Mag Power Supply 2	208 (3ϕ)	40	17900

Vacuum System

The vacuum system requires only 120-VAC power but the total current draw will vary as we pump, bake-out and operate the experiment. During standard operation the nude ion gauge, RGA and the ion pump will be powered. During the pump down the Pirani gauge, turbomolecular pump station will also be powered. During bake-out and getter activation larger current loads will be experienced from the heating tapes.

During standard operation the vacuum pumps draw 1.2 kW, 10 A and the vacuum gauges draw 430 W, 3.7 A. During roughing the pumps draw 2.6 kW, 22 A and the vacuum gauges draw 289 W, 2.5 A During bake-out the pumps draw 1.5 kW, 12.5 A and the gauges draw 220 W, 1.7 A.

For getter activation a DC power supply provides 105 W, 3.5 A at 30 V.

Bake-out

During bake-out the entire TRIMS system will draw a total of $\sim$75 A.

The heating tapes will draw an estimated 4 kW of power, or 33.3 A. The sorption pump heating jacket draws 350 W, corresponding to 3 A. The standard equipment will also be in use, drawing another 37 A.

High Voltage

The Glassman LG-80P supply requires 360 W, 3-amp at the full output. We will run at slightly lower power but 360 W is a reasonable upper limit.

Calibration

The UV pencil lamp requires 12 W, 100 mA. The pulser requires 50 VA for 100-240 VAC.

Front-end Electronics

The preamp and fiber-optic senders are battery powered. The Li-ion battery charger requires 72 W, 0.6 A.

The digitizer is powered by 120 VAC and will run continuously. The current draw is 1A at 115 Vac, for a power consumption of 115 W. The in-rush current is stated as 65A at 230 Vac.

We also need power for a rack that houses a NIM crate with a few relatively low-power modules.

Computers

Two computers will be running at all times. The DAQ is an Apple MacPro4 which draws a maximum of 263 W. The Slow Controls PC is a Compaq CQ5500F which draws 250 W. The Apple Cinema Display draws <300 W. A standard PC monitor would require ∼1.5 A, or 180 W.

Two computers with their own monitors have a total power draw of 1 kW, 8.4 A. If a third computer is necessary this will increase by 50%.

Hot Lab Available Power

There are currently six 120 Vac, 20 A circuits in the room. Five of these circuits are isolated to the Hot Lab and one shares a single outlet with the curved hallway to the tandem. All the 120-Vac power comes from the LB panel in room 176. Three of the circuits come directly from the panel while three are wired through the QO-load center subpanel NS which is installed on the south wall of the lab and wired from breaker 68 of panel LB.

Two 208 Vac, 3-phase, 40-A circuits were installed, drawing power from the ATHENA panel in the neighboring server room.

VITA

Laura Bodine was born in Grand Forks, ND in 1983. She and her three siblings grew up in Yakima, WA where she attended West Valley High School. During high school she participated in the Running Start Program at Yakima Valley Community College. In 2002 she matriculated at the University of Washington where she majored in Physics and Mathematics. During her undergraduate studies she was the recipient of the Physics Department Higgs-Osborn prize for outstanding laboratory coursework and the Miller Award for excellence of scholarship and character. She worked with Professor Gordon Watts, studying single top quark production at the D0 detector at Fermilab. In 2005 she graduate with a Bachelor of Science degree in Physics and Mathematics, with Distinction in Physics.

Following college she spent a year studying physics at the University of Wiconsin - Madison before returning to Seattle for graduate studies at the University of Washington. She spent two years working on the ATLAS experiment with Professor Henry Lubatti before joining the Center for Expermental Nuclear Physics and Astrophysics (CENPA). At CENPA she worked on the Karlsruhe Tritium Neutrino Experiment with Professor R. G. Hamish Robertson. During her time at CENPA she also worked on a variety of neutrino mass related and technical projects, working closely with the team of CENPA engineers. During this time she developed a strong interest in the interplay between physics experiments and engineering, learning how modern physics experiments can push the limits of current technology to improve measurements.